The Hippo signaling transducers Yap1/Wwtr1 in zebrafish development

vom Fachbereich Biowissenschaften (FB15) der Johann
Wolfgang Goethe - Universität als Dissertation angenommen.

Dekan: Prof. Dr. Meike Piepenbring

Gutachter: Prof. Dr. Didier Y. R. Stainier
                Prof. Dr. Virginie Lecaudey

Datum der Disputation :

REVIEWERS

Prof. Dr. Didier Y. R. Stainier, Ph.D.

Department of Developmental Genetics

Max Planck Institute for Heart and Lung Research

61231 Bad Nauheim, Germany

and

Prof. Dr. Virginie Lecaudey, Ph.D.

Department of Developmental Biology of Vertebrates

Institute of Cell Biology and Neuroscience

Johann Wolfgang Goethe University

60438 Frankfurt am Main, Germany

ERKLÄRUNG

Ich erkläre hiermit, dass ich mich bisher keiner Doktorprüfung im Mathematisch-Naturwissenschaftlichen Bereich unterzogen habe.

Frankfurt am Main, den ....

(Unterschrift)

Versicherung

Ich erkläre hiermit, dass ich die vorgelegte Dissertation über

The Hippo signaling transducers Yap1/Wwtr1 in zebrafish development

selbständig angefertigt und mich anderer Hilfsmittel als der in ihr angegebenen nicht bedient habe, insbesondere, dass alle Entlehnungen aus anderen Schriften mit Angabe der betreffenden Schrift gekennzeichnet sind.

Ich versichere, die Grundsätze der guten wissenschaftlichen Praxis beachtet, und nicht die Hilfe einer kommerziellen Promotionsvermittlung in Anspruch genommen zu haben.

Frankfurt am Main, den ....

(Unterschrift)

To my parents: Lai Tek Chai and Ong Ching Goh.

Keranamu, perjalanan ini direalisasikan, dan berjaya. Terima kasih atas kasih sayang dan sokonganmu.

因为你们，博士读成功了。感谢你们的爱，关心 和支持。

"*Fiat Lux*" - Genesis 1:3, the Bible.

"Science: Discover things that have always been true, but you just didn't know it.
Scientism: Things are true if and only if science discovers them." - Comment by Paul Rowe on Facebook.

TABLE OF CONTENTS

ABBREVIATIONS

Abbreviation	Description
RNA	Ribonucleic acid
DNA	Deoxyribonucleic acid
mRNA	Messenger RNA
gRNA	Guide RNA
PCR	Polymerase chain reaction
HRMA	High resolution melt analysis
WT	Wild type
ss	Somite stage
EVL	Enveloping layer
WISH	Whole mount *in situ* hybridization
qPCR	Quantitative real-time PCR
sih	*silent heart* gene
flh	*floating head* gene
cas	*casanova* gene
DA	Dorsal aorta
PCV	Posterior cardinal vein
DLAV	Dorsal longitudinal anastomotic vessel
ISV	Intersegmental vessel
aISV	Arterial ISV
vISV	Venous ISV
PL	Parachordal lymphangioblast
MEF	Mouse embryonic fibroblast
AVC	Atrioventricular canal
At	Atrium
V	Ventricle
L	Lumen
OFT	Outflow tract
Zfish	Zebrafish
KO	Knock-out
CKO	Conditional knock-out
CAYAP	Constitutively active YAP
CAWwtr1	Constitutively active Wwtr1
LLP	Lateral line primordium

RPE	Retinal pigmented epithelium
LPM	Lateral plate mesoderm
ALPM	Anterior lateral plate mesoderm
hpf	Hours post-fertilization
dpf	Days post-fertilization
LEC	Lymphatic endothelial cell
DLLV	Dorsal longitudinal lymphatic vessel
CPC	Cardiac progenitor cell
EST	Expressed sequence tag

1. INTRODUCTION

1.1. The Hippo signaling pathway

The idea of size limit is intuitive, but how this limit is intrinsic to each individual/species is still an incompletely understood phenomenon. Why is our body proportioned in a fixed ratio, such that we are able to approximate our height by the length of our arm span, the length of our feet by the length of our forearm, and the size of our heart by the size of our fists? Metazoan organisms are made up of a collection of multiple specialized cells and have not lost their ancestral roots in unicellular organisms (Vincent, 2010). Indeed, unicellular organisms grow and thrive in nutrient rich environments; a common trick in cell culture technique is serum withdrawal to inhibit cell proliferation (Ryan, 1979). There is little reason for cells to stop proliferating under nutrient rich environments, unless inhibited. In this section, I will introduce the Hippo signaling pathway, a key inhibitor of cell proliferation and survival, which regulates tissue growth and prevents detrimental pathological consequences of overgrowth.

1.1.1. Origins and functions of the Hippo signaling pathway and its nuclear effectors YAP1/WWTR1

The Hippo kinase (Hpo; named after the large stature of the hippopotamus) was first isolated from a forward genetic screen performed in *Drosophila melanogaster* to find genes that limit cellular proliferation (Wu et al., 2003). The underlying idea for such a screen was founded on the notion that tumorigenesis can arise from uncontrolled cell proliferation (Hanahan and Weinberg, 2011). Interestingly, the human ortholog of *hpo*, *STK3/4*, was able to fully rescue the overgrowth phenotype of the *hpo Drosophila* mutant (Wu et al., 2003), suggesting that its function is conserved, and is likely to be part of a conserved pathway (see Table 1 for core proteins in the Hippo signaling pathway and their respective orthologs in flies and humans). Indeed, subsequent experiments in vertebrates showed that STK3/4, and other components of the kinase cassette, regulate tissue growth and their deregulation is commonly associated with tumor growth (Benhamouche et al., 2010; Cai et al., 2010; Lee et al., 2010; Lu et al., 2010; Zhang et al., 2010; Zhou et al., 2009). Subsequent screens identified *Yorkie* (*Yki*; named after the small stature of the Yorkshire Terrier), encoding a transcriptional co-activator that promotes cellular proliferation and survival (Huang et al., 2005). Yki is negatively regulated by the Hippo kinase cassette through select phosphorylation sites that promote its nuclear exclusion and/or proteolytic degradation (Zhao et al., 2010) (Figure 1).

Human proteins	D. melanogaster protein
Core components	
MST1, MST2	Hpo
SAV1 (also known as WW45)	Sav
LATS1, LATS2	Wts
MOB1A, MOB1B	Mats
YAP, TAZ	Yki
TEAD1–TEAD4	Sd
Pathway modulators	
CRB1–CRB3	Crb
PATJ, MUPP1	Patj
MPP5 (also known as PALS1)	Sdt
AMOT, AMOTL1, AMOTL2	-
NF2	Mer
KIBRA	Kibra
FRMD6 (also known as EX1)	Ex
TAO1–TAO3	Tao
MARK1–MARK4	Par-1
E-cadherin	E-cadherin
α-catenin	α-catenin
Ajuba, LIMD1, WTIP	Jub
ZYX, LPP, TRIP6	Zyx
RASSF1-RASSF6	Rassf
PP2A	STRIPAK-PP2A complex (dSTRIPAK)
SCRIB	Scrib
LGL1, LGL2	Lgl
DLG1–DLG4	Dlg
PTPN14	Pez
CSNK1	Dco
β-TRCP	Slimb
HIPK	Hipk
MASK1, MASK2	Mask
WBP2	Wbp2
VGL4	Tgi

Table 1. Core human proteins of the Hippo signaling pathway and their *Drosophila* orthologs. Table adapted from Johnson & Halder 2014 with permission from NPG.
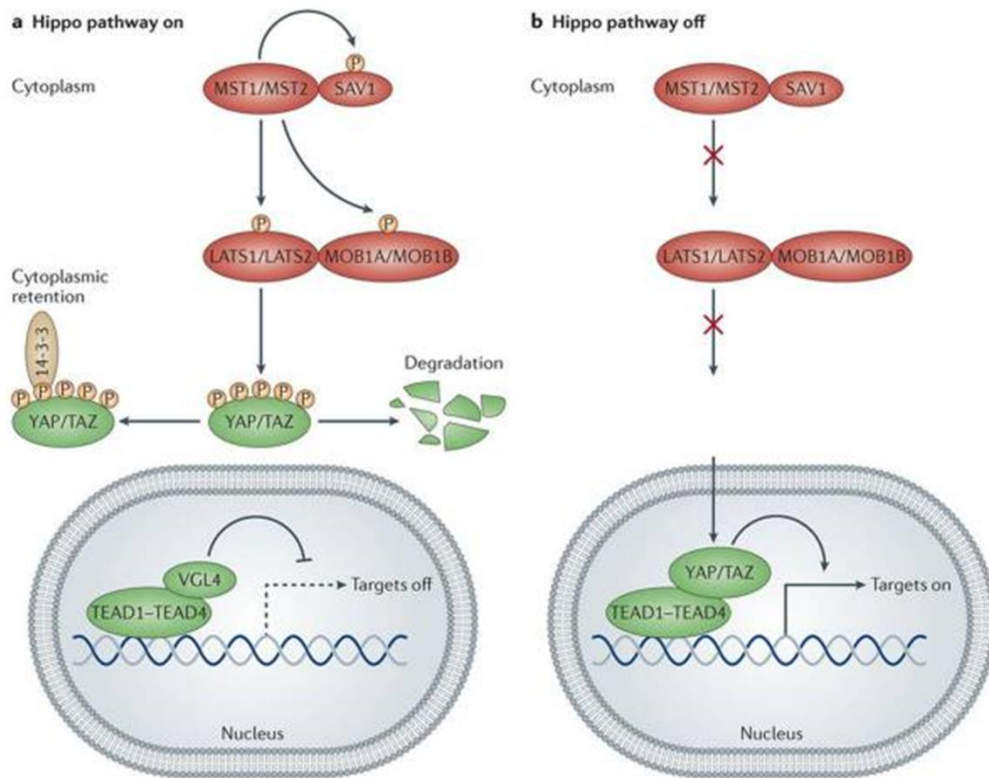
Figure 1. Regulation of YAP1/WWTR1 through the Hippo signaling pathway.
YAP1/WWTR1 (YAP/TAZ) drives transcription of target genes together with TEADs. It is negatively regulated when the core Hippo signaling components are turned on in a kinase cascade as shown in (a). When this core pathway is inhibited or switched off (b), YAP1/WWTR1 can associate with TEADs, translocated into the nucleus to drive genes that promote cell proliferation and survival. Figure taken from Johnson & Halder 2014 with permission from Nature Publishing Group (NPG).

Although the signaling pathway is, for the most part, conserved throughout evolution, it has been proposed that some components of the pathway have diverged (Bossuyt et al., 2014), while others have duplicated. For example, *Yki* (*YAP1*) was duplicated in vertebrate ancestors to give rise to *WWTR1* (Hilman and Gat, 2011). The domains and structures of YAP1 and WWTR1 are largely similar, and some studies indicated a considerable overlap in their function (Zanconato et al., 2015). YAP1 and WWTR1 bind to TEADs via their TEAD-binding domain (Vassilev et al., 2001; Zhao et al., 2008) to regulate the expression of several target genes that promotes growth and survival, such as *CTGF*, *CYR61*, *AURK*, *CCND1*, etc (Johnson and Halder, 2014).

1.1.2. Protein domains of YAP1/WWTR1

YAP1 and WWTR1 are composed of four principal domains, namely the TEAD-binding domain (TBD), WW domain, transcriptional activation domain, and the PDZ-binding motif. The fifth and less characterized domain is the SRC-homology domain. The TBD, as mentioned earlier, is responsible for YAP1/WWTR1 interaction with TEADs. The crystal structure of this complex has been solved for both YAP1 (Chen et al., 2010) and WWTR1 (Kaan et al., 2017). However, the latter observation noted a nuanced difference in binding dynamics. The interaction with TEADs is essential, as TEADs have a DNA binding domain but lack transcriptional activation domains, and, conversely, YAP1/WWTR1 lack DNA binding domains but possess a C-terminal transcriptional activation domain (Cao et al., 2008). The WW domain contains a conserved binding pocket which recognizes proline-rich motifs, namely PPXY (Chen et al., 1997; Linn et al., 1997). The WW domain can be regarded as a modular domain (Sudol and Harvey, 2010), as it allows YAP1/WWTR1 to associate with a host of protein partners to drive specific functions. Specific substitutions in this domain have been shown to abolish binding of the WW domain to the PPXY motif of binding partners (Chen et al., 1997; Ermekova et al., 1997; Komuro et al., 2003; Manderfield et al., 2015). Functionally, inactivation of the WW domain was shown to dampen the activation of YAP1 by Neuregulin-ERBB4 signaling (Komuro et al., 2003), as well as abrogate the interaction with the Notch intracellular domain (NICD) (Manderfield et al., 2015). In another protein, WW domain-containing protein, PQBP1, a missense mutation in the WW domain is the underlying cause of the Golabi-Ito-Hall syndrome (Lubs et al., 2006). The transcriptional activation domain, enables the YAP1/WWTR1-TEADs complex to drive transcription of target genes. Finally, the PDZ-binding motif is a ~5-residue motif that can be recognized by the PDZ domain, provided that the motif is exclusively in the C-terminal tail or in a structural

mimic of a terminus (Harris and Lim, 2001). Proteins with PDZ domains recognize this motif and can assemble large complexes or stabilize localization of a protein (Haggie et al., 2006), as observed in the cystic fibrosis gene, CFTR. In YAP1/WWTR1, it has been documented that perturbation to the PDZ-binding motif can interfere with nuclear localization and function (Cao et al., 2008; Kanai, 2000; Oka and Sudol, 2009; Oka et al., 2010). Although the function of the YAP1/WWTR1-TEADs complex is a topic of intense research, the diverse repertoire of YAP1/WWTR1 binding partners suggest that novel functions of YAP1/WWTR1 remain to be discovered.

1.1.3. The mechanisms regulating YAP1/WWTR1

In addition to a diverse set of protein domains, YAP1 and WWTR1 possess a number of serine and tyrosine phosphorylation sites, whose phosphorylation can modulate the spatiotemporal distribution and function of these proteins. For the purpose of this introduction, only the phosphorylation sites of YAP1 will be covered to minimize repetition, as these sites are conserved in WWTR1. Of the five (four in WWTR1) serine phosphorylation sites on YAP1, phosphorylation of the S127 residue (of the human protein), leads to binding of YAP1 to the nuclear export factor, 14-3-3 (Zhao et al., 2010). Another key serine phosphorylation site is S381, which signals for the degradation of YAP1 through the $SCF^{\beta-TRCP}$ proteasome degradation pathway (Zhao et al., 2010). Both serine residues are part of the HXRXXS peptide motif that is recognized by LATS1/2 (Zhao et al., 2007), which is the human ortholog of *Drosophila* Wts and a component of the Hippo kinase cassette. Apart from the negative regulation of YAP1/WWTR1 through the phosphorylation of these serine residues, YAP1/WWTR1 also contain a tyrosine (Y357) residue that is phosphorylated by a Src family kinase, YES (Taniguchi et al., 2015). Phosphorylation of this tyrosine residue promotes the nuclear import of YAP1. Therefore, YAP1/WWTR1 contain specific phosphorylation sites that instruct their spatiotemporal distribution in the cell to help achieve exquisite tissue growth control.

YAP1 and WWTR1 are primarily regulated by the Hippo kinase cassette as mentioned earlier. The Hippo kinase cassette is, in turn, regulated by a number of upstream cues such as G-protein coupled receptors (GPCRs) (Yu et al., 2012), cell polarity complexes (apico-basal and planar cell polarity) (Genevet and Tapon, 2011), and cell-cell junction complexes (Schlegelmilch et al., 2011; Varelas et al., 2010; Yu and Guan, 2013). Nevertheless, YAP1 and WWTR1 can be regulated independently of the Hippo kinase cassette, such as

mechanotransduction (Dupont et al., 2011; Nakajima et al., 2017). For example, mechanical force from the contraction of chick skeletal muscles can promote Yap1 nuclear localization and affect muscle differentiation through Notch signaling (Esteves de Lima et al., 2016). Intriguingly, most of the upstream regulators of YAP1/WWTR1 are reliant on external cues, thus placing YAP1 and WWTR1 in a position to modulate cellular behaviors in relation to signals from neighbouring cells.

1.1.4.   The roles of YAP1/WWTR1 in vertebrate development

The function of YAP1/WWTR1 has been studied in various model systems, including mouse and fish. In mouse, YAP1/WWTR1 has been implicated in the regulation of tissue growth of organs such as liver (Lu et al., 2010) and heart (Heallen et al., 2011; von Gise et al., 2012; Xin et al., 2011). Similarly, the size regulation of the lateral line primordium (LLP) (Agarwala et al., 2015) and liver (Cox et al., 2016) in zebrafish is regulated by Yap1. However, the function of YAP1/WWTR1 is not restricted to regulation of tissue growth. In mouse embryos, YAP1/WWTR1, in cooperation with TEADs, are important for trophectoderm specification (Nishioka et al., 2009). In medaka fish embryos, Yap1 plays an essential role in maintaining tissue tension for 3D body morphogenesis (Porazinski et al., 2015). Furthermore, YAP1 is important for retinal pigmented epithelium (RPE) specification, proper closure of the optic fissure (Miesfeld et al., 2015; Williamson et al., 2014), as well as kidney morphogenesis (Hossain et al., 2007; Reginensi et al., 2015; Reginensi et al., 2016). As mentioned earlier, YAP1 and WWTR1 can respond to mechanical cues and have recently been implicated in vascular development by a number of research groups (Kim et al., 2017; Nakajima et al., 2017; Wang et al., 2017). Finally, YAP1 participates in cardiac regeneration of adult mammalian hearts following myocardial infarction, by promoting cardiomyocytes to reenter the cell cycle and other cellular functions (Bassat et al., 2017; Heallen et al., 2013; Morikawa et al., 2015; Morikawa et al., 2017; Xin et al., 2013). Altogether, while YAP1/WWTR1 is widely associated with tissue growth control and tumorigenesis, recent research efforts have revealed a role for YAP1/WWTR1 in specific tissue morphogenetic processes during development.

1.2.   Vascular development

Blood vessels are an important part of the cardiovascular system as they carry blood from the heart into every parts of the animal. The blood carries nutrient, oxygen, signaling molecules etc., to nourish tissues as well as to serve as a communication network between tissues.

Additionally, our immune cells are carried through the bloodstream to survey and to defend against foreign invaders. This highly sophisticated and important circulatory system, nevertheless has its simple origins during embryonic development, and is conserved among vertebrates.

1.2.1. Vasculogenesis

Vasculogenesis is a process of *de novo* vascular morphogenesis. It involves the migration of angioblasts, at ~ 14 hours post-fertilization (hpf), from the lateral plate mesoderm (LPM) to the midline that coalesce to form the axial vessel just ventral to the notochord (Ellertsdóttir et al., 2010; Jin et al., 2005) (Figure 2A). The midline (notochord, floor plate, and hypochord) secretes a signaling ligand called Apelin, which guides angioblasts in the lateral side of the developing embryo to migrate medially (Helker et al., 2015). The midline is exquisitely required for the migration of the angioblasts, as the *floating head* (*flh*) mutants which lacks the midline, do not show coalescence of the angioblasts in the midline in order to form the axial vasculature (Fouquet et al., 1997; Sumoy et al., 1997). Angioblasts migrate to the midline in two waves: the first initial wave forms the dorsal aorta (DA), and shortly after, a second wave of migration forms the posterior cardinal vein (PCV) (Kohli et al., 2013). Once the DA and PCV are formed, new vessels emerge from them through endothelial sprouting in a process called angiogenesis.

1.2.2. Angiogenesis

Endothelial sprouting first occur from the DA at ~20 hpf (Isogai et al., 2003). The leading cell, or tip cell, emanates long protrusions and move dorsally as though attracted to the source (Isogai et al., 2003; Lawson and Weinstein, 2002). The principal signaling pathway governing this process is Vegf signaling, as *vegfaa* mutants/morphants have completely abrogate the initial angiogenic sprouting (Nasevicius et al., 2000; Rossi et al., 2016). Endothelial cells in individual sprouts move in a collective manner, led by a tip cell followed by stalk cells (Jakobsson et al., 2010; Siekmann and Lawson, 2007). Once the sprout reaches the dorsal part of the neural tube, the arterial intersegmental vessel (aISV) is formed, and connects with neighboring aISVs to form the dorsal longitudinal anastomotic vessel (DLAV) (Isogai et al., 2003) (Figure 2B).
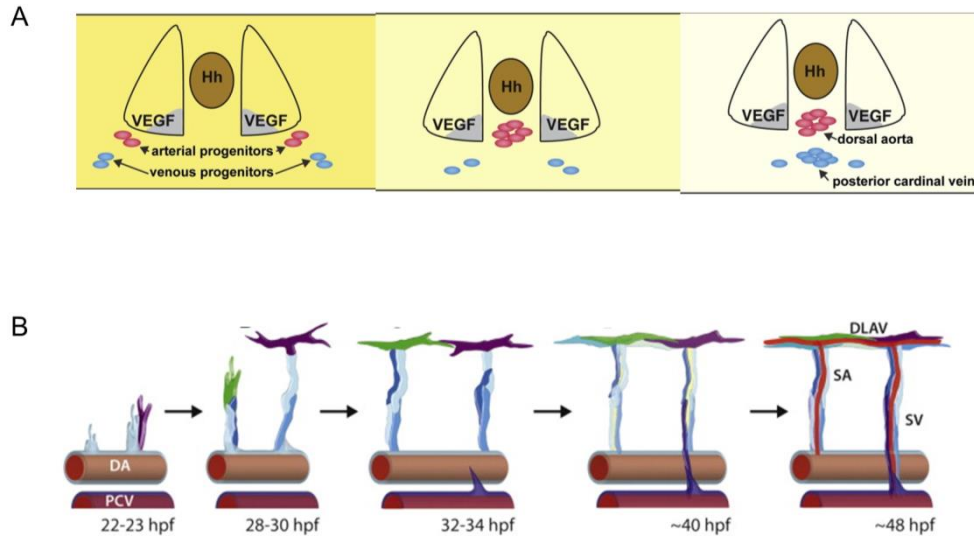
Figure 2. Overview of vascular development in zebrafish. (A) Angioblasts in the lateral sides of the embryo migrate to the midline as they are attracted to signaling molecules expressed by the midline. They coalesce in two distinctive waves to form the dorsal aorta (DA) and posterior cardinal vein (PCV). (B) Primary angiogenic sprouting arise from endothelial cells in the DA. Endothelial cells migrate dorsally in a collective manner and connect to neighboring segmental vessels to form the dorsal longitudinal anastomotic vessels (DLAV). A second wave of angiogenic sprouting arise from the PCV, some giving rise to the venous vascular network, otherwise the lymphatic vascular network. SA - segmental arteries (or aISVs); SV - segmental veins (or vISVs). (A) was adapted from Kohli et al., 2013 and (B) was taken from Ellertsdóttir et al., 2010 with permission from Elsevier.

Following the formation of the primary vascular network, a second wave of angiogenic sprouting begins from the PCV at ~ 30 hpf (Figure 2B). The principal signaling pathway is again Vegf, but this time through the Vegfc ligand which is processed by Ccbe1 (Hogan et al., 2009a; Hogan et al., 2009b; Le Guen et al., 2014), and binds to Vegfr3 which is expressed in the PCV to initiate secondary sprouting angiogenesis to form the venous and lymphatic vascular network (Le Guen et al., 2014; Nicenboim et al., 2015; Yaniv et al., 2006). A subset of these secondary sprouts will form a connection to the adjacent aISV to form the venous intersegmental vessels (vISVs), which also redirects blood flow from the DLAV into the PCV and then back into the heart (Isogai et al., 2003). The remaining secondary sprouts, which are lymphatic endothelial cells (LECs) or parachordal lymphangioblasts (PLs), migrate to the horizontal myoseptum and move anterior-posteriorly to form the parachordal chain (PAC) (Bussmann et al., 2010). This is followed by its migration along the aISVs, dorsally to the DLAV network to form the dorsal longitudinal lymphatic vessel (DLLV), and ventrally into the space between the DA and PCV to form the thoracic duct (Bussmann et al., 2010; Yaniv et al., 2006). The migration cues of the LECs are distinct from vISVs, as mutations affecting the Cxcl12-Cxcr4 chemokine signaling stalls LEC migration without perturbing vISV development (Cha et al., 2012).

Additionally, the endothelium, which is the innermost layer of the vasculature is responsive to blood flow (Lee et al., 2006; Nicoli et al., 2010), and can be important for processes such as endothelial cell migration and pruning (Franco et al., 2015; Franco et al., 2016; Kwon et al., 2016). Furthermore, it was shown recently with a Tead reporter line, that the zebrafish endothelium exhibit Yap1/Wwtr1 activity which is responsive to blood flow. Notably, Yap1 and Wwtr1 were shown to be crucial for angiogenic sprouting, vascular barrier maturation and vascular stability (Kim et al., 2017; Nakajima et al., 2017; Wang et al., 2017). Blood flow is dispensable for primary angiogenic sprouting as the *silent heart* (*sih*) mutants do not exhibit gross perturbation to the primary vascular network patterning (Isogai et al., 2003). However, the role of blood flow on secondary angiogenic sprouting was briefly described as below:

"Secondary intersegmental vessel sprouts appear at the proper time in mutant animals, and, as in wild-type animals, many sprouts contribute to the parachordal system. The connection of secondary sprouts to primary segments cannot be definitively assayed in the absence of blood flow, but it is not obviously evident in *sih* mutants." (Isogai et al. 2003).

It is therefore worth noting that the function of mechanosensing in endothelial cells has not been thoroughly explored, and it will be of interest to investigate the role of blood flow on angiogenesis through the modulation of Yap1/Wwtr1 activity.

1.3.   Heart development

The heart is an organ that functions to pump blood into the vascular network. This organ is not unique to vertebrates, however, as non-vertebrates such as flies have pump-like organs that function to distribute the hemolymph, albeit in an "open" circulatory system (Rosenthal and Harvey, 2010). For the purpose of this thesis, I will describe the development of the vertebrate heart, which has three principal layers, namely the epicardium, myocardium and the endocardium (Bakkers, 2011; Staudt and Stainier, 2012). The cellular mechanism and signaling networks that specifies and coordinate the formation of the heart is thought to be largely conserved throughout (Rosenthal and Harvey, 2010), although 'higher' and 'lower' vertebrates can be distinguished by the existence of additional heart chambers, i.e. a two-chambered fish heart compared to a four-chambered mammalian heart. The emergence of additional chambers in 'higher' vertebrates is to primarily separate the systemic circulation from the pulmonary circulation, which is necessary for terrestrial animals to perform gaseous exchange through the lung.

1.3.1.   Development and growth of the heart

1.3.1.1.   Orchestration of cardiomyocytes in the formation of a heart

Similar to angioblasts in the previous chapter, cardiac progenitor cells (CPCs) are specified during gastrulation and arise from the mesoderm (Bakkers, 2011; Staudt and Stainier, 2012). During segmentation stages, CPCs in the anterior lateral plate mesoderm migrate to the midline and coalesce, first posteriorly, then anteriorly, to form the cardiac disc (Figure 3a, b). By this stage, the arterial and ventricular cardiomyocytes are already specified (Keegan et al., 2004; Staudt and Stainier, 2012), as evident by their respective markers. Unlike angioblasts, the midline migration of the CPCs is dependent on the endoderm, as the *casanova* (*cas*) mutants invariably exhibit bifid hearts (Alexander et al., 1999), in which two distinct myocardial tissues in lateral positions are found beating rhythmically, and independently. Through forward genetic screening, many genes have been implicated in the midline migration of CPCs such as *spns2*, *s1pr2* (*miles apart; mil*), *fn1a* (*natter; nat*), *mixl1* (*bonnie*

and clyde; bon), *sox17*, *tdgf1* (*one-eyed pinhead; oep*), and *gata5* (*faust; fau*) (Chen et al., 1996; Stainier et al., 1996; Staudt and Stainier, 2012). Although there had been a study that implicated Yap1 in the migration of CPCs (Fukui et al., 2014), the conclusion was largely mired in morpholino toxicity as the *yap1* zebrafish mutants did not recapitulate the cardia bifida phenotype of the *yap1* morphants (Agarwala et al., 2015; Miesfeld et al., 2015; Nakajima et al., 2017).

Once the cardiac disc is formed, cardiomyocytes undergo a series of complex morphogenetic movements to form the heart tube (Stainier, 2001) (Figure 3c), and by this time rhythmic pulses of contractility has begun. The heart tube then intrinsically loops dextrally (Noël et al., 2013), guided by signaling cues that establish left-right asymmetry (Staudt and Stainier, 2012). This looping is followed by ballooning of the atrial and ventricular chambers (Figure 3d). Both chambers are separated by the atrioventricular canal (AVC), where the heart valves will form from the endocardial layer to prevent retrograde flow from the ventricle into the atrium (Pestel et al., 2016; Staudt and Stainier, 2012). By 60 hpf, the ventricular wall begins to mature via trabeculation (Figure 3e), which is thought to facilitate myocardial growth in the absence of coronary vascular network (see below). The heart, continues to grow in size by addition of new cardiomyocytes through differentiation and proliferation (Chen et al., 2004; Choi et al., 2013; Staudt and Stainier, 2012).
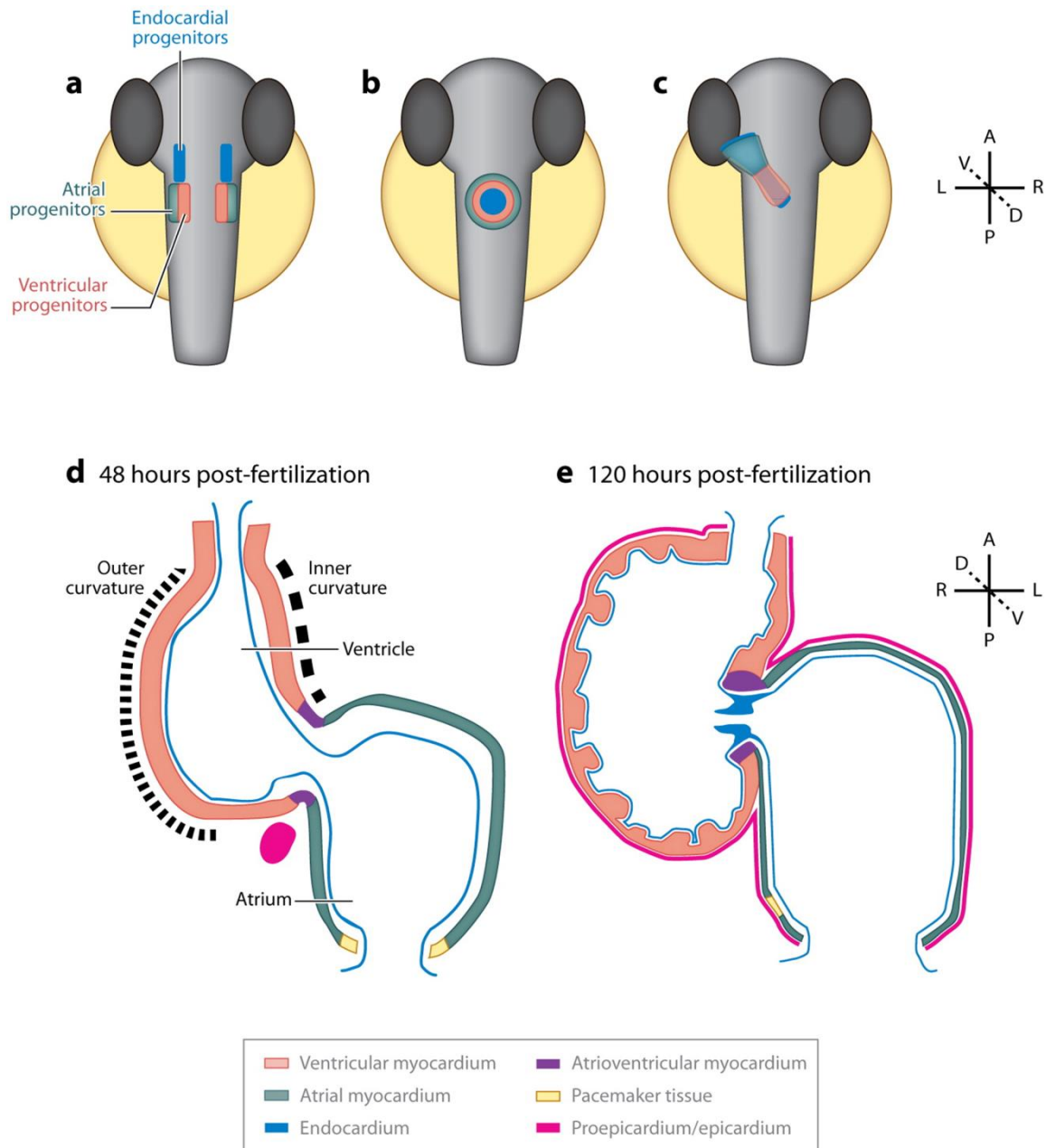
Figure 3. Overview of heart development in zebrafish. (a-c) Midline migration of cardiac progenitor cells (CPCs) to form the cardiac disc and then the heart tube. (d) After looping of the heart tube, atrial and ventricular chambers are formed. (e) The cardiomyocytes in the ventricular chamber undergo a series of complex morphogenetic movements leading to trabecular morphogenesis. Figure taken from Staudt & Stainier 2012.

1.3.1.2. Cardiomyocyte proliferation and heart regeneration

In mammals, as the heart continues to develop, the myocardium becomes increasingly quiescent (Naqvi et al., 2014; Soonpaa et al., 1996), and is thought to largely lack any proliferative capacity in adults. This observation is one of many underlying reasons why the adult mammalian hearts are unable to regenerate after myocardial insults. In contrast to mammalian hearts, the zebrafish and amphibian hearts robustly regenerate after different forms of injuries (Porrello and Olson, 2014; Poss et al., 2002; Vivien et al., 2016). A key difference between fish/amphibian and mammalian cardiomyocytes is the number of nuclei per cardiomyocyte. The percentage of multinucleated mammalian cardiomyocytes, after birth, increases, but not indefinitely, over time (Botting et al., 2012; Soonpaa et al., 1996). Furthermore, it has been recorded that multinucleation of mouse cardiomyocytes is through cytokinesis failure (Clubb and Bishop, 1984), and possibly in combination with endomitosis, as each nucleus can have variable ploidy number in some mammalian cardiomyocytes (Botting et al., 2012). While aneuploid cells (such as cancer cells), or tetraploid cells (such as hepatocytes) are not quiescent, multinucleated cells such as myotubes are indefinitely quiescent. Similarly, multinucleated cardiomyocytes are thought to be incapable of reentering the cell cycle (Soonpaa et al., 1996). Zebrafish and amphibian cardiomyocytes, on the other hand, do not face this limitation, as their cardiomyocytes are largely mononucleated (Matz et al., 1998; Oberpriller et al., 1988; Wills et al., 2008) and can reenter the cell cycle. Nevertheless, this comparative correlation cannot entirely explain the different heart regenerative capacity of different animals. For example, the percentage of mononucleated cardiomyocytes in medaka is similar to zebrafish (my unpublished observations), but medaka hearts are not regenerative. Furthermore, over 70% of cardiomyocytes in human hearts are mononucleated (Botting et al., 2012), but are quiescent and unable to repair a myocardial wound. Moreover, minute cardiomyocyte turnover in adult human hearts has been reported (Bergmann et al., 2009).

Recent efforts in searching for factors that promote cardiomyocytes to reenter the cell cycle has revealed key pathways that limit myocardial growth. For example, supplying the myocardium with Neuregulin1 can stimulate cardiomyocyte proliferation and partial regeneration of the injury area (Bersell et al., 2009; Polizzotti et al., 2015). However, overstimulation with NRG1 can be detrimental to heart function (Gemberling et al., 2015). The myocardial-specific conditional knock-out (CKO) of components belonging to the Hippo kinase cassette results in higher cardiomyocyte proliferation rates, higher percentage of

mononucleated cardiomyocytes, cardiomegaly, and robust cardiac regeneration in adulthood (Heallen et al., 2011; Heallen et al., 2013). Whether loss of the Hippo signaling pathway promotes multinucleated cardiomyocytes to become mononucleated, as observed in knock down experiments leading to the inactivation of the Hippo signaling pathway (Ganem et al., 2014), remains to be tested. The Hippo signaling pathway limits cardiomyocyte proliferation through YAP1, as *Yap1* CKO myocardial wall is thinner (von Gise et al., 2012; Xin et al., 2011). Moreover, the regenerative property of neonatal mouse hearts are compromised when *Yap1* is conditionally deleted (Xin et al., 2013). Conversely, expression of a constitutively active YAP1 (CAYAP), which can partially override the negative regulation of the Hippo kinase cassette, promoted cardiomyocyte proliferation (von Gise et al., 2012), but not complete cardiac regeneration as observed in the *Salv* CKO injured hearts (Xin et al., 2013). The Hippo signaling pathway therefore limits myocardial growth through regulation of YAP1.

1.3.2. Cardiac trabeculation

1.3.2.1. The structure and function of trabeculae

Cardiac trabeculae are muscular ridges that appear to extend from the atrio-ventricular canal (AVC) and continuously line the entire outer-curvature of the ventricular chamber. The emerging ridges are aligned orthogonally to the direction of blood flow (Reischauer et al., 2014). Morphologically, trabecular cardiomyocytes are distinct from compact wall cardiomyocytes (Reischauer et al., 2014; Wenink et al., 1996), the former have mature myofibrils lining the cortex and spans across the long axis of the cell, whilst the latter have striated cortical actin network. Without the highly specialized trabecular cardiomyocytes, the ventricular chamber can still contract and pump blood, albeit weaker (García-Rivello et al., 2005; Liu et al., 2010; Ozcelik et al., 2002), leading to dilated cardiomyopathy. These data indicate that trabeculae are the primary drivers of ventricular chamber contractility. Another characteristic of trabecular morphology is that it increases the surface area of the ventricular chambers to allow sufficient nourishment of cardiac muscles in the absence of a coronary circulatory system (Sedmera et al., 2000). Altogether, cardiac trabeculae are essential for cardiac performance, and perturbation to trabecular development can lead to congenital heart diseases (Fahed et al., 2013; Zemrak et al., 2014). Thus, it is important to understand the underlying mechanism that modulates trabeculation.

1.3.2.2.   The molecular mechanisms governing trabecular development

The key signaling pathway that governs cardiac trabeculation is the Neuregulin signaling pathway, as mutants affecting the ligand (mouse: NRG1; zebrafish: Nrg2a) or its receptor (mouse: ERBB2/4; zebrafish: Erbb2) completely abrogates any emergence of cardiac trabeculae (Gassmann et al., 1995; Lee et al., 1995; Liu et al., 2010; Meyer and Birchmeier, 1995; Rasouli and Stainier, 2017). Molecular analyses indicate that the Neuregulin ligand is expressed in the endocardial layer (Grego-Bessa et al., 2007; Meyer and Birchmeier, 1995; Rasouli and Stainier, 2017), while the receptor(s) are expressed in the myocardial layer (Gassmann et al., 1995; Han et al., 2016; Lee et al., 1995). Following stimulation of ERBB2/4 receptors in cardiomyocytes, a subset of cardiomyocytes in the compact wall send out protrusions luminally and migrate (delaminate) to occupy the trabecular layer (Staudt et al., 2014). Whether this morphogenetic movement is an epithelial-mesenchymal transition (EMT) phenomenon remains to be thoroughly established, but current data provide support for this hypothesis (Jiménez-Amilburu et al., 2016).

In addition to the Neuregulin signaling pathway, Notch signaling activity has been documented at various steps of heart development and implicated in trabecular development (D'Amato et al., 2016; Grego-Bessa et al., 2007; Han et al., 2016; Jiménez-Amilburu et al., 2016). Notch activity is first observed in the endocardial layer after formation of the heart tube (Han et al., 2016; Samsa et al., 2015). In mouse, Notch signaling in the endocardium modulates the expression of *EphB2*, which in turn regulates the expression of *Nrg1 (Grego-Bessa et al., 2007)*. Consistent with this model, early inactivation of Notch activity recapitulates the *neuregulin/erbb* mutant heart phenotype (Han et al., 2016). Interestingly, Notch activity, as assessed by the *tp1* Notch reporter, was detected in a subset of cardiomyocytes after the initiation of trabeculation, and this signal is largely absent in trabeculae null mutant models (Han et al., 2016; Jiménez-Amilburu et al., 2016). Furthermore, lineage tracing experiments with the *tp1* promoter showed that cardiomyocytes which expressed this promoter eventually remained in the compact layer (Jiménez-Amilburu et al., 2016).

As mentioned earlier, the Hippo signaling pathway has been shown to intersect with the Notch and Neuregulin signaling pathways. Although mice mutants affecting the Hippo signaling pathway primarily exhibit a myocardial growth phenotype (Heallen et al., 2011; von Gise et al., 2012; Xin et al., 2011), the role for WWTR1, the vertebrate paralog of YAP1, in

25

heart development has not been explored. To this end, I have generated *yap1* and *wwtr1* zebrafish mutants to study their roles in zebrafish development, but with greater emphasis on the cardiovascular system.

2. AIMS OF THE PROJECT

Yap1 and Wwtr1 have been implicated in the regulation of growth and specific developmental processes, but their role in cardiovascular development remains unclear. My goal is to generate zebrafish *yap1* and *wwtr1* mutants to deepen our understanding of the function of Yap1/Wwtr1 in zebrafish development, with an emphasis on the cardiovascular system. I have chosen to work with the zebrafish model as it is an excellent animal model to study the cardiovascular development down to the cellular and molecular level. The developing embryos are transparent and the cardiovascular network is easily accessible to advanced confocal microscopy platforms for live imaging as well as 3D reconstructions. Additionally, the zebrafish genome is tractable with the advent of TALENs and CRISPR/CAS9.

AIM 1: Generation of zebrafish *yap1* and *wwtr1* mutants
I will generate zebrafish *yap1* and *wwtr1* mutants using the CRISPR/CAS9 technology and evaluate their roles in zebrafish embryonic development. As both genes are in separate chromosomes, and are evolutionary related, I will take the opportunity to study the compound mutants. I will utilize light microscopy to characterize developmental abnormalities arising from the combinatorial loss of these genes.

AIM 2: Elucidate the functions for Yap1/Wwtr1 in vascular development
As Yap1/Wwtr1 are known to respond to external mechanical shear stress in endothelial cells, I will investigate the consequences of the loss-of-function of Yap1/Wwtr1 in zebrafish vascular development. Specifically, I will examine the roles for blood flow in vascular development and whether blood flow executes its function through Yap1/Wwtr1.

AIM 3: Uncovering the roles of Yap1/Wwtr1 in heart development
The Hippo signaling pathway has been primarily implicated in the growth and repair of the myocardium (Heallen et al., 2011; von Gise et al., 2012; Xin et al., 2011). Furthermore, the cross-talk between the Neuregulin and Hippo signaling pathways were documented before (Haskins et al., 2014; Komuro et al., 2003). However, the role for WWTR1, a vertebrate paralog of YAP1, in cardiac development is poorly studied. Here, I report undiscovered roles for the Hippo signaling pathway, especially Wwtr1, in myocardial wall maturation.

3.   MATERIALS AND METHODS

3.1.   Materials

3.1.1.   Machines

Machines	Supplier	Machines	Supplier
Centrifuge 5418	Eppendorf	Bacterial shaker	Infors HAT
Centrifuge 5417R	Eppendorf	Bacterial incubator	Heraeus
Centrifuge 5810R	Eppendorf	Heating block	VWR
mastercycler pro	Eppendorf	Microwave oven	Bosch
PTC-100 thermalcycler	MJ Research	Zebrafish breeding tanks	Tecniplast
GeneTouch thermalcycler	Bulldog Bio	Zebrafish aquaculture system	Tecniplast
NanoDrop 2000c	Thermo Scientific	Zebrafish incubator	Panasonic
Injection micromanipulator	World precision instruments	Stereomicroscope Stemi 2000	Zeiss
Picospritzer III	Parker	Stereomicroscope SMZ18	Nikon
CFX connect real time PCR	BioRad	Stereomicroscope SMZ25	Nikon
Gel Doc EZ	BioRad	LSM700 confocal microscope	Zeiss
Electrophoresis power supply	BioRad	LSM800 confocal microscope (inverted)	Zeiss
Microscale	Novex	LSM880 confocal microscope	Zeiss
Weighing balance	Sartorius	Spinning disk confocal microscope	Zeiss
Micropipette puller P-1000	Sutter Instrument	CM1950 Cryostat	Leica

3.1.2.   Laboratory Supplies

Laboratory supplies	Supplier	Laboratory supplies	Supplier
Bacterial culture tube	Sarstedt	Petri dish	Greiner bio-one
Latex gloves	Roth	Forceps	Dumont
Nitrile gloves	VWR	Glass bottles	Duran
Beakers	VWR	Laboratory film	Parafilm
Eppendorf tubes	Sarstedt	Pipetboy	Integra

Falcon tubes	Greiner bio-one	Pipette tips	Greiner bio-one
Glass bottom dish	MatTek	Filtered pipette tips	Greiner bio-one
Microloader pipette tips	Eppendorf	Conical flasks	VWR
PCR tubes	Sarstedt	Serum pipette	Greiner bio-one
Scalpel	Braun	Spring scissors	Dumont
Pipettes	Gilson		

3.1.3. Antibiotics

Antibiotics	Working concentration (µg/ml)
Ampicillin	100

3.1.4. Antibodies

Antibody	Supplier	Catalog #	Dilution
Anti-DIG-AP	Roche	11093274910	1:10,000
Anti-DIG-POD	Roche	11207733910	1:1000
Anti-WWTR1	Cell Signaling	D24E4	1:200
Anti-EGFP	Aves Lab	gfp-1020	1:200
Anti-MYH1	DSHB	MF20	1:200

3.1.5. Bacteria

Strain	Purpose
DH5α	Competent cells

3.1.6. Chemicals

Chemical	Supplier	catalog #	Chemical	Supplier	catalog #
Mineral oil	Sigma	M8410	Agarose	Peqlab	35-1020
SOC media	Thermo Scientific	15544034	LB medium	Roth	X968
LB agar	Roth	X969	Nuclease-free water	Ambion	AM9938
DIG RNA labeling mix	Roche	11277073910	Trizol	Ambion	15596018
Bovine serum albumin (BSA)	Sigma	A2153	Acidic phenol	Ambion	AM9720
Chloroform	Merck	102445	Glycerol	Millipore	356350
Citric acid	Sigma	27487	Pronase	Roche	10165921001

DNA ladder (100bp)	Thermo Scientific	SM0241	SYBR safe	Invitrogen	S33102
DNA ladder (1kbp)	Thermo Scientific	SM0311	1-Phenyl-2-thiourea (PTU)	Sigma	P7629
Ethanol (molecular grade)	Roth	5054.4	NaCl	Sigma	S3014
Ethanol (denatured)	Roth	K928.3	KCl	Sigma	P9541
Methanol	Roth	4627.5	$MgSO_4$	Sigma	M2643
Paraformaldehyde (PFA)	Sigma	P6148	H_2O_2	Sigma	31642
Gel loading dye	Thermo Scientific	R0611	KOH	Sigma	P1767
Heparin	Sigma	H5515	Proteinase K	Roche	1092766
Isopropanol	Roth	6752.4	Formamide (deionized)	Ambion	AM9342
20X SSC	Ambion	AM9763	Sucrose	Sigma	S0389
Methylene blue	Sigma	M9140	Phenol red	Sigma	P0290
NBT/BCIP stock solution	Roche	11681451001	$MgCl_2$	Sigma	63068
Tricaine	Pharmaq	NA	HCl	Sigma	H1758
Phosphate-buffered saline (PBS) tablets	Sigma	P4417	HEPES	Sigma	H3375
Dimethylsulfoxide (DMSO)	Sigma	D4540	$NaHCO_3$	Roth	965.1
Sheep serum	Sigma	S3772	$MgSO_4.7H_2O$	VWR	437044K
Tris	Roth	5429.2	Dextran sulfate sodium salt	Sigma	42867
Tween-20	Sigma	P1379	4-Iodophenol	sigma	I10201
Triton X-100	Sigma	RES3103T-A101X	sodium tetraborate	Sigma	221732
tRNA	Sigma	R7876	Boric acid	Sigma	B6768
CutSmart buffer	NEB	B7204S	Blocking Reagent	Roche	11921673001
Agarose, low gelling temperature	Sigma	A9414	Alexa Fluor 568 Tyramide reagent	Thermo Scientific	B40956

Alexa Fluor 568 Phalloidin	Thermo Scientific	A12380	DAPI	Thermo Scientific	D1306
OCT	Sakura	4583			

3.1.7. Buffer/Solutions

Buffer/Solutions	Composition
Egg water	3 g Instant Ocean 0.75 g Calcium sulfate 10 L final volume (distilled water)
Hybridization Mix (HM)	50% deionized formamide 5X SSC 0.1% Tween-20 50 ug/mL heparin 500 ug/mL tRNA Adjust to pH6 with 1M citric acid
HM - wash	50% deionized formamide 5X SSC 0.1% Tween-20 Adjust to pH6 with 1M citric acid
10X TBE	121 g Tris 62 g Boric Acid 7.4 g EDTA 1 L final volume (distilled water)
Blocking buffer (WISH)	2 mg/mL BSA 2% Sheep serum Dissolved in 1X PBST
Alkaline tris buffer	100 mM Tris HCl pH9.5 100mM NaCl 50 mM MgCl$_2$ 0.1% Tween-20 Dissolved in distilled water
10X PBS	10 PBS tablet (Sigma) 200 mL distilled water
1X PBST	0.1% Tween-20 Dissolved in 1X PBS
1X PBSTT	0.1% Tween-20 0.1% Triton X-100 Dissolved in 1X PBS
1X PBSTTD	1% DMSO Dissolved in 1X PBSTT
4% PFA	40 g PFA Dissolved in 1 L 1X PBS

	Adjust to pH7 by HCl/NaOH
Blocking buffer (immunostaining)	2 mg/mL BSA 5% Sheep serum dissolved in 1X PBSTTD
200 mM Borate pH8.5	200 mM boric acid 150 mM NaCl 50 mM sodium tetraborate
TSA buffer	100 mM Borate pH8.5 0.1% Tween-20 2% Dextran sulfate 0.003% H_2O_2 (450 ug/ml 4-iodophenol)
10X Modified Barth's Saline (MBS) pH7.8	880 mM NaCl 10 mM KCl 10 mM $MgSO_4.7H_2O$ 50 mM HEPES 25 mM $NaHCO_3$
1X MBS	20 ml 5X MBS 7 mL 0.1 M $CaCl_2$ H2O to 100 mL

3.1.8. Restriction Enzymes

Restriction Enzymes	Supplier
EcoRI-HF	NEB
ClaI	NEB
AgeI	NEB
XhoI	NEB
NotI	NEB
NheI	NEB
BamHI-HF	NEB
BsmBI	NEB
XbaI	NEB

3.1.9. Kits

Kits	Supplier	Catalog #
Phusion taq DNA polymerase	NEB	M0530
KAPA 2G master mix	KAPA biosystems	KM5101
SYBR Green PCR master mix	Thermo Scientific	F-416
mMessage mMachine SP6 transcription kit	Ambion	AM1340
mMessage mMachine T7 transcription kit	Ambion	AM1344
mMessage mMachine T3 transcription kit	Ambion	AM1348

MEGAshortscript T7 transcription kit	Ambion	AM1354
High-Capacity RNA-to-cDNA kit	Applied Biosystems	4387406
Maxima First Strand cDNA Synthesis Kit for RT-qPCR, with dsDNase	Thermo Scientific	K1671
Rapid DNA ligation kit	Thermo Scientific	K1422
pGEM-T Easy Vector cloning kit	Promega	A1360
Q5 site-directed mutagenesis kit	NEB	E0554
GeneJET PCR purification kit	Thermo Scientific	K0701
GeneJET gel extraction kit	Thermo Scientific	K0691
GeneJET plasmid miniprep kit	Thermo Scientific	K0502
Direct-zol RNA MicroPrep kit	Zymo Research	R2061
miRNeasy Micro Kit	Qiagen	217084

3.1.10. Plasmids

Plasmid	Resistance	Source
pCS2+	Ampicillin	Addgene
pTol2 myl7	Ampicillin	Javad Rasouli
pT3TS-nlsCas9nls	Ampicillin	Addgene
pT7-gRNA	Ampicillin	Addgene
pCS2+ CAYAP	Ampicillin	Kimberly Evason
Plasmid with mKate	Ampicillin	Hyouk-Bum Kwon
Plasmid with EGFP	Ampicillin	Hyouk-Bum Kwon
pCS2+ transposase	Ampicillin	Andrea Rossi

3.1.11. Zebrafish food

Food	Developmental stage
SDS100	5 dpf - 12 dpf
Brine Shrimp	> 1 months
SDS200	1 - 2 months
SDS300	2 - 3 months
SDS400	> 3 months

3.1.12. Zebrafish transgenic lines

Line Name	Abbreviation	Publication
Tg(myl7:mKate-CAAX)^{sd11Tg}	*Tg(myl7:mKate-CAAX)*	Lin et al., 2012
Tg(myl7:EGFP-Hsa.HRAS)^{s883Tg}	*Tg(myl7:EGFP-Hsa.HRAS)*	D'Amico et al., 2007
Tg(-5.1myl7:DsRed2-NLS)^{f2Tg}	*Tg(-5.1myl7:DsRed2-NLS)*	Rottbauer et al., 2002

Tg(EPV.Tp1-Mmu.Hbb:Venus-Mmu.Odc1)^{s940Tg}	*Tg(tp1:Venus-PEST)*	Ninov et al., 2012
Tg(myl7:BFP-CAAX)^{bns193Tg}	*Tg(myl7:BFP-CAAX)*	This study
Tg(myl7:LIFEACT-GFP)^{s974Tg}	*Tg(myl7:LA-GFP)*	Reischauer et al., 2014
TgBAC(cdh2:cdh2-EGFP,crybb1:ECFP)^{zf517Tg}	*TgBac(cdh2:cdh2-EGFP)*	Revenu et al., 2014
Tg(-0.2myl7:EGFP-podocalyxin)^{bns103Tg}	*Tg(-0.2myl7:EGFP-podxl)*	Jiménez-Amilburu et al., 2016
Tg(-0.2myl7:Mark3a-tagRFP)^{bns240Tg}	*Tg(-0.2myl7:Mark3a-tagRFP)*	Jiménez-Amilburu et al., 2016
Tg(fli1:EGFP)^{y1Tg}	*Tg(fli1:EGFP)*	Lawson & Weinstein, 2002
TgBAC(etv2:EGFP)^{ci1Tg}	*TgBAC(etv2:EGFP)*	Proulx et al., 2010
Tg(-5.2lyve1b:DsRed)^{nz101Tg}	*Tg(-5.2lyve1b:DsRed)*	Okuda et al., 2012
Tg(Hsa.CTGF:nlsmCherry)^{ia49Tg}	*Tg(Hsa.CTGF:nlsmCherry)*	Astone et al., in preparation
Tg(myl7:EGFP-Wwtr1)^{bns239Tg}	*Tg(myl7:EGFP-Wwtr1)*	This study

3.1.13. Zebrafish mutants

Allele	**Gene**	**Publication**
yap1^{bns19}	*yap1*	This Study
wwtr1^{bns35}	*wwtr1*	This Study
vegfc^{hu6410}	*vegfc*	Le Guen et al., 2014

3.1.14. Morpholinos

Gene	**Sequence (5'->3')**	**Publication**	**Other names**
tnnt2a	CATGTTTGCTCTGATCTGACACGCA	Sehnert et. al., 2002	*silent heart;sih*
Standard control	CCTCTTACCTCAGTTACAATTTATA	NA	

3.1.15. Primers

Sequence (5'->3')	**Name**	**Purpose**	**PMID**
TGGGATCCGCTAGCCCACCATGGTGTCTAAGGGCGAAG	Fmkate	Cloning mKate	
GAGCGGCCGCATCGATGCGGGTTTCTTGGATCT	Rmkate_NS	Cloning mKate	

G			
GCTCTGGGTGTCCATGT AGG	136. cmfiemF1	Sequencing	
CTGCATTCTAGTTGTGG TTTGTCC	137. emfigfpR2	Sequencing	
AATTCGGCAGTGGAGA GGGCAGAGGAAGTCTG CTAACATGCGGTGACG TCGAGGAGAATCCTGG CCCAAT	5'-EcoRI-2Ap-ClaI-3'	2A linker	
CGATTGGGCCAGGATT CTCCTCGACGTCACCG CATGTTAGCAGACTTC CTCTGCCCTCTCCACTG CCG	5'-ClaI-2Ap-EcoRI-3'	2A linker	
TAGGACCTCATCGGCA CGGAAGGG	cF_yap1_TBD1	CRISPR gRNA (yap1)	
AAACCCCTTCCGTGCC GATGAGGT	cR_yap1_TBD1	CRISPR gRNA (yap1)	
CTGTTTGTGGTTTCTGA GGGG	Fyap1_TBD1n2	bns19 genotyping	
CGCTGTGATGAACCCG AAAA	Ryap1_TBD1n2	bns19 genotyping	
CTCGAGCGGCCGCAAA TTAATTAAC	Rmkate-NotI-XhoI	Cloning mKate	
GTGACACTGCAGGCTG AAAG	F_yapTBD_founderSc reen	CRISPR yap1 founder sequencing primer	
GCGCGTTTCCACATTTA TTT	R_yapTBD_founderSc reen	CRISPR yap1 founder sequencing primer	
GCTAGTTATTGCTCAGC GG	T7 terminalPrimer		
TAGGTCACCACATGGC	cF_wwtr1_WW	CRISPR	

ACGACCCC		gRNA (wwtr1)	
AAACGGGGTCGTGCCATGTGGTGA	cR_wwtr1_WW	CRISPR gRNA (wwtr1)	
TTTGTTGTGCAGTCACATTGAG	Fwwtr1_WW	bns35 genotyping	
GAGGGCGTCATGCTCTTC	Rwwtr1_WW	bns35 genotyping	
CTGGAAGGGTGTCCACTGAT	F_wwtr1_WW_founderScreen	CRISPR wwtr1 founder sequencing primer	
CTGAGAGAGGGCCATGGAG	R2_wwtr1_WW_founderScreen	CRISPR wwtr1 founder sequencing primer	
TGAGTGGAAACAACCCCATC	F_yap1_qPCRa	qPCR yap1	
GAAAGGGTCAGAGCTGTTGG	R_yap1_qPCRa	qPCR yap1	
TCCAGAGGAGACAGGAGGAG	F_wwtr1_qPCRb	qPCR wwtr1	
AGTGGTCGGGATGCTGTAAC	R_wwtr1_qPCRb	qPCR wwtr1	
GTGTTCACCTGGTGTAAGCCTAGTTC	F_ctgfa_qPCRa	qPCR ctgfa	
ACCGTCCAGACACGTGCACTGGTAT	R_ctgfa_qPCRa	qPCR ctgfa	
TAAGGACGGAGTGAACAACCA	F_rpl13_qPCR	qPCR rpl13	
CTTACGTCTGCGGATCTTTCTG	R_rpl13_qPCR	qPCR rpl13	
ACGCGAAGATGTTTGCTTGG	F_cyr61_qPCRa	qPCR cyr61	
CCGGCCCTCTGATTTAG	R_cyr61_qPCRa	qPCR	

CTC		cyr61	
GGTGGTATCGATATGA GCGGTAATCCTCTCC	F_cDNA_ClaI-wwtr1	cloning wwtr1	
GGTGGTCTCGAGCTAC TACTAGAGCCAGGTGA GGAAG	R_cDNA_wwtr1-XhoI	cloning wwtr1	
GGTGGTGCTAGCATGA TGGTGAGCAAGGG	F_NheI-GFP-linker	cloning EGFP	
GGTGGTACCGGTTGTA GCGACGGGAGGGTCGC CGAGCTTGTACAGCTC GTCC	R_AgeI-GFP-linker	cloning EGFP	
GGTGGTACCGGTATGA GCGGTAATCCTC	F_AgeI-wwtr1_cDNA	cloning wwtr1	
GGTGGTCTCGAGCTAC TAGAGCCAGGTGAGG	R_wwtr1-XhoI_cDNA	cloning wwtr1	
GAGCCCGCCGGCAGCT GTAGGGACGCCGGAGA AGCGCGCGAGCGAAAG	R_wwtr1_S79A	CAWwtr1 SDM	
ACAGCTGCCGGCGGGC TCCGTG	F_wwtr1_S79A-NaeI	CAWwtr1 SDM	
gacgctAGGAAGAGCATG ACGCCC	F_wwtr1_mutWW_S DM	Wwtr1 SDM	
gtgagcTGTGGTGATCTTC TCAATGTGATTG	R_wwtr1_mutWW_S DM	Wwtr1 SDM	
TATGCCGCAGgctTTCTT CCAGG	F_wwtr1_S48A_TBD _SDM	Wwtr1 SDM	
TCCTTGTTCCTCCAGGA GC	R_wwtr1_S48A_TBD _SDM	Wwtr1 SDM	
TCCGGTTCTCTCCCGCC G	F_wwtr1_delTBD_SD M	Wwtr1 SDM	
CATATCCTTGTTCCTCC AGGAGCTC	R_wwtr1_delTBD_SD M	Wwtr1 SDM	
GGCCTCAACAGAGCTT CAAC	F_vegfc_qPCR_a	qPCR vegfc	20625388
TCTCTTGGGGTCCACGT TAC	R_vegfc_qPCR_a	qPCR vegfc	20625388

TGCACCAGTATGCCAC ATTT	F_vegfr3_qPCR_b	qPCR vegfr3	24069224
TGCTTCCATTGCTTTGA CTG	R_vegfr3_qPCR_b	qPCR vegfr3	24069224
AATCGCAACGACGAAG TACC	F_ccbe1_qPCR_a	qPCR ccbe1	24069224
CCGGCACACACATCAT AATC	R_ccbe1_qPCR_b	qPCR ccbe1	24069224
CGCCATTCATGCACCG ATTT	F_cxcl12a_qPCR_b	qPCR cxcl12a	
TGACTTGGAAGGGGCA GTTG	R_cxcl12a_qPCR_b	qPCR cxcl12a	
TTTCTCCCAACGGTGTA CGG	F_cxcr4a_qPCR_a	qPCR cxcr4a	
TACCAGTCTTTGGCCAC GTC	R_cxcr4a_qPCR_a	qPCR cxcr4a	
CATTAACCCTCACTAA AGGGAAGATATCCAGG GGTTCCGAAA	F_mrc1a_PCRish	WISH mrc1a	
TAATACGACTCACTAT AGGGGGCATGTTCATT CTGTTCGA	R_mrc1a_PCRish	WISH mrc1a	
CATTAACCCTCACTAA AGGGAAATGCCGGCAA AACCAGC	F_mybphb_PCRish	WISH mybphb	
TAATACGACTCACTAT AGGGGATCTTCACGGA GGCAG	R_mybphb_PCRish	WISH mybphb	
CATTAACCCTCACTAA AGGGAAGCAAACCTTG CTTTCGAGTC	F_vegfc_PCRish	WISH vegfc	
TAATACGACTCACTAT AGGGAGGACGGCTGTG CTTTACAC	R_vegfc_PCRish	WISH vegfc	
CATTAACCCTCACTAA AGGGAAGGGGAAGAT AAGGGAGATGG	F_efnb2a_PCRish	WISH efnb2a	
TAATACGACTCACTAT	R_efnb2a_PCRish	WISH	

AGGGGCGTGTCCATTT TCACACCT		efnb2a	
GGTGGTATCGATATGC CGGCAAAACCAGCACC	F_ClaI-mybphb	clone mybphb	
GGTGGTCTCGAGTTATT ATTTCTTATCAGCATCA GC	R_mybphb-XhoI	clone mybphb	
CTTTCATCAATCTTGAA CTTTT	1_vegfc_WT	hu6410 genotyping	
AAACTCTTTCCCCACAT CTA	2_vegfc_WT	hu6410 genotyping	
GATGAACTCATGAGGA TAGTTT	1_vegfc_hu6410	hu6410 genotyping	
TAAATTAATAGTCACT CACTTTACT	2_vegfc_hu6410	hu6410 genotyping	

3.1.16. Softwares

Name	Purpose
R	Data analysis
Fiji	Image processing
Imaris (Bitplane)	Image processing
Zen Blue (Zeiss)	Image processing

3.2. Methods

3.2.1. Ethics Statement

Animal experiments with zebrafish embryos and larvae adhere to German animal protection laws and approved by local governmental animal protection committee. Zebrafish were raised and maintained following standard zebrafish husbandry practices (zfin.org). Protocols involving live animals were approved by the veterinary department of the Regional Board of Darmstadt.

3.2.2. Zebrafish husbandry

Zebrafish adults were reared in an aqua culture system (Techniplast) as recommended in "The Zebrafish Book. A guide for the laboratory use of zebrafish (*Danio rerio*), 4th edition, 2000,

Westerfield M.". Water tank temperature was set at 28°C and room temperature was set at 29°C. The fish were grown in a light-dark cycle of 14 hours of light and 10 hours of dark. The fish tanks are connected to a water recycling system equipped with biological filters and UV-sterilization.

A zebrafish couple is placed in a breeding tank in the evening with a separator. The next morning, the divider is removed at a planned time no later than 12pm. Females were allowed to spawn for at least 10 minutes and at most 1 hour. Eggs were collected and cleaned before they are used for injections or for growing. 6 hours after the eggs were collected, unfertilized or poor eggs were discarded and the remaining embryos were staged and placed into fresh Petri dishes.

3.2.3.   Embryo care

A maximum of 50 zebrafish embryos were grown in egg water in a 90 mm Petri dish. Incubator for embryos were set at 28.5°C. At 24 hpf, PTU was added to the egg water to prevent pigmentation for subsequent imaging experiments. Chorion was removed either manually by a pair of sharp forceps or by incubating in pronase.

3.2.4.   Preparation of injection plates and needles

1% agarose is dissolved in egg water with the aid of a microwave oven. The homogenous solution is poured into a Petri dish and a custom made mold is placed on the agarose solution. The agarose is left in room temperature to cool. Once solidified, the mold is carefully removed. The injection plates can be stored in a 4°C fridge.

Glass capillaries were pulled by a micropipette puller to obtain fine-tipped needles. The injection cocktail was loaded into the needle and the tip of the needles are broken by a forcep. A drop of mineral oil is placed on a microruler to measure the size of the injection droplet.

3.2.5.   RNA Isolation (cDNA stock)

50 zebrafish embryos or 3 zebrafish adult hearts were pooled in Trizol solution and mechanically dissociated with a pestle. The samples were frozen in -80°C overnight. Phase separation was performed according to manufacturer's instructions. The RNA pellet was resuspended with 20-50 μL of nuclease free water and stored at -80°C.

3.2.6. cDNA synthesis (cDNA stock)

1 µg of RNA was used for the reverse-transcriptase reaction using the High-Capacity RNA-to-cDNA kit according to manufacturer's instructions. The cDNA was stored in -80°C for long term storage. The obtained cDNA was used to clone genes into an expression vector or to make the anti-sense *in situ* probes.

3.2.7. CRISPR mutants

3.2.7.1. gRNA assembly

guideRNA (gRNA) oligos targeting zebrafish *yap1* and *wwtr1* were designed with a tool developed by the Zhang Lab (crispr.mit.edu). The oligos (*yap1*: cF_yap1_TBD1 and cR_yap1_TBD; *wwtr1*: cF_wwtr1_WW and cR_wwtr1_WW) were assembled and cloned into the pT7-gRNA plasmid linearized with BsmBI restriction enzyme. Ligation reaction was performed with Rapid DNA ligation kit according to manufacturer's instructions, followed by transformation of competent cells. Clones of transformed bacteria were picked and cultured in suspension media overnight. Plasmids were then isolated with a miniprep kit and sent for sequencing with the M13Fwd standard sequencing primer to confirm the insertion of the gRNA oligos.

3.2.7.2. gRNA synthesis

pT7-gRNA plasmids containing the gRNA oligos were linearized with the BamHI-HF restriction enzyme. The reaction was cleaned up with the GeneJET PCR purification kit. This linearized plasmid will serve as a template for RNA synthesis using the MEGAshortscript T7 transcription kit according to manufacturer's instructions. The gRNA was then isolated by phenol-chloroform extraction with acidic phenol. RNA pellet was resuspended in nuclease free water to a final concentration of 500 ng/µL and stored in -80°C in 1 µL aliquots.

3.2.7.3. CAS9 mRNA synthesis

Plasmid containing *CAS9* gene (pT3TS-nlsCas9nls) was linearized by XbaI restriction enzyme. The reaction was cleaned up with the GeneJET PCR purification kit. This linearized plasmid will serve as a template for RNA synthesis using the mMessage mMachine T3 transcription kit according to manufacturer's instructions. The synthesized *CAS9* mRNA was then isolated by phenol-chloroform extraction with acidic phenol. RNA pellet was

resuspended in nuclease free water to a final concentration of 750 ng/µL and stored in -80°C in 1 µL aliquots.

3.2.7.4. Injection and efficiency test

The injection cocktail contained 100 ng of gRNA, 150 ng of *CAS9* mRNA, 1 µL of phenol red and nuclease free water to a final volume of 5 µL. 1 nL of the injection cocktail was injected into the yolk of one-cell stage embryos. Uninjected embryos were kept as negative controls. 8 individual 1 dpf embryos were digested in a PCR strip tube with Proteinase K for at least an hour at 55°C. Proteinase K was inactivated at 95°C for 10 minutes. A high-resolution melt analysis (HRMA) was performed with the respective primers (*yap1*: Fyap1_TBD1n2 and Ryap1_TBD1n2; *wwtr1*: Fwwtr1_WW and Rwwtr1_WW). The HRMA reaction consists of:

Reagent	Volume (µL)
SYBR Green PCR master mix	5
DNA template	1
Premixed primer pairs (5 mM)	0.8
Water	3.2
Total	10

The amplification program of the HRMA was:

Step	Temperature (°C)	Time	Description
1	95	10 minutes	Polymerase activation
2	95	10 seconds	PCR amplification, 35-40 cycles
	60	15 seconds	
3	55	15 seconds	HRM analysis
	95	15 seconds	

If mutation was detected in some of the injected embryos, the remaining injected embryos were raised.

3.2.7.5. Founder screening

F0 adult fish were outcrossed to WT adult fish. 8 embryos were sampled at 1 dpf to obtain DNA for HRMA as described above. DNA samples that show heterozygosity from the HRMA were then used as a template to amplify a larger fragment around the gRNA target site for TA cloning and sequencing. The primers used for this purpose were: *yap1* - F_yapTBD_founderScreen and R_yapTBD_founderScreen; *wwtr1* - F_wwtr1_WW_founderScreen and R2_wwtr1_WW_founderScreen. PCR reaction was performed with KAPA 2G mastermix according to manufacturer's instructions. The amplicon was isolated and purified with the GeneJET gel extraction kit followed by TA cloning. The plasmid was sent for sequencing with the standard T7 primer. The sequencing results were aligned to the expected WT sequence to identify the lesion.

3.2.7.6. Maintenance

The founder carrying the desired lesion was outcrossed to relevant transgenic lines. The F1 progenies were grown until adulthood. DNA was isolated from a small piece of F1 adult fins to perform the HRMA as described earlier. DNA samples with the same HRMA profile as the desired lesion were used for TA cloning to confirm the lesion of interest. The identified F1 adult fish (*yap1^{bns19}* and *wwtr1^{bns35}*) were again outcrossed to obtain the stable mutant lines.

3.2.7.7. Genotyping of *yap1^{bns19}* and *wwtr1^{bns35}*

Genotyping of the stable mutant lines were done by regular PCR with the following primers - *yap1*: Fyap1_TBD1n2 and Ryap1_TBD1n2; *wwtr1*: Fwwtr1_WW and Rwwtr1_WW. When exogenous *wwtr1* was introduced into the animal (i.e. plasmid injections or transgenics), the *wwtr1^{bns35}* allele can be genotyped with these primers instead: F_wwtr1_WW_founderScreen and Rwwtr1_WW. The PCR reaction was as follows:

Reagent	Volume (μL)
KAPA 2G master mix	5
DNA template	1
Premixed primer pairs (5 mM)	0.8
Water	3.2
Total	10

The cycling conditions were:

Step	Temperature (°C)	Time	Description
1	95	5 minutes	Template denaturation
2	95	10 seconds	PCR amplification, 35-40 cycles
	60	15 seconds	

The PCR products were separated on a 2% agarose gel to identify the genotypes.

3.2.8.   Plasmid constructs

3.2.8.1.   pTol2 *myl7:mKate*

The pTol2 *myl7:mKate* plasmid was generated by cloning the NheI-CCACC-mKate-XhoI fragment (underlined are restriction sites for cloning) into a multiple cloning site of a Tol2 enabled vector that is downstream of a *myl7* promoter. CCACC is the Kozak sequence. The mKate fragment was amplified with the following primers: Fmkate and Rmkate-NotI-XhoI.

3.2.8.2.   pTol2 *myl7:mKate-2A-wwtr1*

The pTol2 *myl7:mKate-2A-wwtr1* plasmid was generated by ligating the NheI-CCACC-mKate-EcoRI, EcoRI-2A-ClaI and ClaI-wwtr1-XhoI fragments and then cloned into the Tol2 enabled vector. The fragments were amplified with the following primers - mKate: Fmkate and Rmkate_NS; wwtr1: F_cDNA_ClaI-wwtr1 and R_cDNA_wwtr1-XhoI. The 2A peptide sequence is GSGEGRGSLLTCGDVEENPGP (Kim et al., 2011).

3.2.8.3.   Site-directed mutagenesis to obtain Wwtr1 variants

To obtain the WW*, TBD* and ΔTBD mutant constructs, site-directed mutagenesis (SDM) was performed using Q5 Site-Directed Mutagenesis Kit on the pTol2 *myl7:mKate-2A-wwtr1* plasmid. The following primers were used for SDM, WW*: F_wwtr1_mutWW_SDM and R_wwtr1_mutWW_SDM; TBD*: F_wwtr1_S48A_TBD_SDM and R_wwtr1_S48A_TBD_SDM; ΔTBD: F_wwtr1_delTBD_SDM and R_wwtr1_delTBD_SDM. All reactions were done following manufacturer's recommendation. The mutated *wwtr1* constructs were confirmed by Sanger Sequencing and were re-cloned using the ClaI and XhoI cloning sites into the parent plasmid to avoid any off-target mutations.

3.2.8.4.   pTol2 *myl7:mKate-2A-CAWwtr1*

The CAWwtr1 construct was obtained by SDM via PCR with the following primers: F_wwtr1_S79A-NaeI and R_wwtr1_S79A. The amplicon was digested with NaeI and cloned into the NaeI cloning site. The digested pTol2 *myl7:mKate-2A-wwtr1* plasmid was treated with Antarctic Phosphatase to prevent self-ligation of plasmid. After successful insert of the amplicon, the correct orientation of the insert was determined by Sanger Sequencing.

3.2.8.5.   pTol2 *myl7:mKate-2A-mybphb*

The pTol2 *myl7:mKate-2A-mybphb* construct was obtained by first amplifying the *mybphb* fragment with the following primers: F_ClaI-mybphb and R_mybphb-XhoI. The amplicon was digested and cloned into the ClaI/XhoI cloning site of the pTol2 *myl7:mKate-2A-wwtr1* plasmid. Insert sequence was validated by Sanger Sequencing.

3.2.8.6.   pTol2 *myl7:EGFP-Wwtr1*

The pTol2 *myl7:EGFP-Wwtr1* plasmid was generated by ligating the NheI-CCACC-EGFP-linker-AgeI and AgeI-wwtr1-XhoI fragments and cloned into the same Tol2 enabled vector containing the *myl7* promoter. The EGFP and wwtr1 fragments were amplified with the following primers - EGFP: F_NheI-GFP-linker and R_AgeI-GFP-linker; wwtr1: F_AgeI-wwtr1_cDNA and R_wwtr1-XhoI_cDNA. The linker sequence, LGDPPVAT, was kindly provided by Dr. Alessandro Mongera.

3.2.9.   TA-Cloning

Amplicons with A-overhangs were cloned into the pGEM-T easy vector system following manufacturer's instructions. The cloned vector was used to transform competent cells on LB agar plates supplemented with Ampicillin and X-Gal. The next day, white colonies were selected for further verification of the insert of interest.

3.2.10.   Bacterial glycerol stock storage

Bacterial clones from a suspension culture was mixed in 50:50 glycerol:LB media and stored at -80°C.

3.2.11.   Generating zebrafish transgenic lines

3.2.11.1.   transposase mRNA synthesis

Plasmid containing *transposase* gene (pCS2+ transposase) was linearized by NotI restriction enzyme. The reaction was cleaned up with the GeneJET PCR purification kit. This linearized plasmid will serve as a template for RNA synthesis using the mMessage mMachine SP6 transcription kit according to manufacturer's instructions. The *transposase* mRNA was then isolated and purified by phenol-chloroform extraction with acidic phenol. RNA pellet was resuspended in nuclease free water to a final concentration of 150 ng/µL and stored in -80°C in 1 µL aliquots.

3.2.11.2.   Microinjection and screening

The injection cocktail consisted of 15 ng/µL of *transposase* and 8-12 ng/µL of plasmid. 1 nL of the cocktail was injected into the cell of one-cell stage embryos. At 3 dpf, injected larvae hearts were screened for successful integration of the plasmid by the expression of the fluorescent marker encoded in the plasmid.

3.2.11.3.   Founder screening

F0 injected fish were outcrossed to WT fish. A total of 100 3 dpf larvae hearts were screened for successful transmission of the injected plasmid. Larvae hearts expressing the fluorescent marker encoded by the plasmid were then imaged under the confocal microscope to assess quality of the integrated transgene. F1 larvae with good transgenic insertion were grown to adulthood and outcrossed for experiments.

3.2.12.   Fixing zebrafish embryos/larvae

Embryos or larvae were fixed with 4% PFA. For experiments involving confocal imaging of hearts, the embryos/larvae were first anesthetized with 0.2% tricaine for at most 5 minutes before fixation with 4% PFA. Samples were fixed for at least 2 hours at room temperature or overnight at 4°C. For immunostaining of hearts, fixed samples were decapitated, leaving the hearts attached to the head, and clearing out any residual yolk. The remaining body was used for genotyping, if applicable. Images for Figures 30A and B were obtained from fixed hearts as the working distance of the 60X lens is too narrow.

3.2.13. Whole mount *in situ* hybridization (WISH)

Standard WISH protocol was carried out (Thisse and Thisse, 2008). cDNA from zebrafish embryos or adult zebrafish hearts were used as template for the PCR reaction to obtain the template for the *in vitro* transcription of the anti-sense probe. Purified amplicons were used as template for the *in vitro* transcription with themMessage mMachine T7 transcription kit, but the nucleotides were replaced with DIG RNA labeling mix. The anti-sense probe from the reaction was purified with Sigmaspin post-reaction purification columns. At day 3 of the WISH protocol, after development of the alkaline phosphatase (AP) staining, samples were fixed with 4% PFA for at least 20 minutes followed by 3X washes with 1X PBST or 1X PBSTTD. If an immunofluorescent staining reaction was required, the protocol was followed by the whole mount immunostaining protocol as described below. For imaging, samples were not embedded in glycerol, instead they were mounted on a 1% LMA (dissolved in 1X PBS) scaffold. Mutants and siblings were placed in the same reaction tube.

3.2.14. Fluorescent *in situ* hybridization (FISH)

A FISH protocol was carried out as described previously (Lauter et al., 2014). Antibody against Wwtr1 (D24E4) was incubated with the anti-DIG-POD antibody after incubation with the anti-sense probes and washing off the excess probes. After the tyramide signal amplification (TSA) reaction, the reaction was quenched followed by incubation with a secondary antibody to detect the D24E4 antibody. The samples were then placed in a glycerol gradient before flat-mounting.

3.2.15. Whole mount immunofluorescent staining

Fixed samples were washed with 1X PBSTTD for half an hour. This was followed by one incubation with blocking buffer (immunostaining). Primary antibodies were diluted in blocking buffer and incubated with samples overnight at 4°C. After incubation with primary antibody(ies), samples were rinsed 3X with 1X PBSTTD and then washed every half hour with 1X PBSTTD over a duration of at least 6 hours. This was followed by secondary antibody incubation overnight at 4°C and a similar washing regiment the next day. Samples were post-fixed with 4% PFA for at least 20 minutes prior to imaging. Phalloidin conjugated to Alexa-568 (Life Technologies) was diluted at 1:500 ratio and DAPI (Life Technologies), 1:10,000. Endogenous transgenic fluorescent signal perdures through all the procedures and no further antibody staining was required. An equal number of control group and treatment

group samples were placed in the same reaction tube. For 14-18ss embryos, they were placed in a glycerol gradient before mounting.

3.2.16. Microscopy

3.2.16.1. Stereo microscopy

Stereo micrographs were obtained with the Nikon SMZ25 system. Samples were embedded in 1% low melting temperature agarose (LMA) or mounted on a 1% agarose scaffold.

3.2.16.2. Confocal microscopy (Spinning Disk/LSM800/LSM700/LSM880)

Live embryos or larvae were embedded in 1% LMA dissolved in egg media. To image stopped hearts, the 1% LMA contained 0.2% (w/v) tricaine, otherwise 0.04% of tricaine was used. Hearts that were manually isolated from fixed fish were embedded in 1% LMA dissolved in 1X PBS on glass-bottom dishes.

To image whole mount immunostaining of 14-18 ss embryos, the embryos were manually deyolked and flat-mounted on a microscope slide. All 4 corners of a microscope cover slip was dipped in plasticine, so that the plasticine acts as a "pedestal", and then placed on the flat-mounted sample. Gentle pressure was applied evenly on the cover slip to keep the flat-mounted sample in place.

3.2.17. Image processing and analysis

Image analyses were carried out in Imaris (Bitplane), Zen Blue (Zeiss) or Fiji (Schindelin et al., 2012). Details for image analyses can be found in their individual subsections.

3.2.18. Statistical analysis

Analyses were carried out in R. The packages used for data management and plotting includes *ggplot2* (Wickham, 2010), *beeswarm*, *RColorBrewer*, and *plyr*. Poisson regression was used on count data, otherwise standard linear models (i.e. Student t-test, linear regression, etc.) were used for continuous data. Distribution of cardiomyocytes between compact and trabecular layer was tested with Binomial test.

3.2.19. Quantifying expression of Hsa.CTGF reporter line

An incross of *yap1$^{+/-}$;wwtr1$^{+/-}$* fish were performed to obtain embryos for this experiment. Double homozygous mutants die by 30 hpf and are excluded from analysis. Remaining

siblings that are *etv2:*EGFP and *Hsa.CTGF:*nlsmCherry positive were embedded in 1% low melting agarose and images were acquired with spinning disk confocal microscope (25X objective) at 48 hpf. Image analyses were done with Imaris software. Firstly, EGFP positive cells were selected to delineate endothelial cell nuclei expressing mCherry. Only endothelium on the side of the embryo closest to the objective lens was analyzed. Endothelial cells of arterial (aISV), venous (vISV) and lymphatic identities were quantified separately. aISVs are vessels connected to the DA, vISVs are vessels connected to the PCV and lymphatic vessels are vessels on the horizontal myoseptum. For each nucleus, average signal intensity of mCherry channel was normalized to average signal intensity of EGFP. The normalized values for all selected nuclei were averaged per animal.

3.2.20.   Analyzing PCV deviation from the midline

yap1$^{-/-}$*;wwtr1*$^{+/-}$ embryos and randomly sampled siblings were embedded in 1% low melting agarose for image acquisition with LSM800 (25X objective) at 30 and 48 hpf. Orthogonal projection function on Zen software was utilized to obtain a series of transverse sections of the trunk. The neural tube (NT), dorsal aorta (DA) and posterior cardinal vein (PCV) were manually demarcated with an ellipse tool in Fiji. The center points of each ellipse were connected to form a triangle. The angle on the vertex of the DA (Θ) was measured, and the angle of the PCV from the midline can be inferred by calculating $180° - \Theta$.

For cryosections of 72 hpf larvae, *yap1*$^{-/-}$*;wwtr1*$^{+/-}$ larvae with blood circulation and randomly sampled siblings were fixed with 4% PFA and genotyped using a small piece of the tail. After fixation, fixed larvae were transferred to a sucrose gradient before embedding in OCT. Each section is 12 μm thick. Sections were permeabilized with 0.1% Triton X-100 followed by blocking with 5% sheep serum. Standard Immunohistochemistry was performed with anti-EGFP antibody and Alexa-568 conjugated phalloidin. Sections were counterstained with DAPI and imaged with LSM800.

3.2.21.   Characterizing cranial and hyaloid vasculature phenotype

Images of 72 hpf animals from an incross of *yap1* heterozygous adults were obtained with LSM700 confocal microscope (20X objective), and scoring of cranial vasculature phenotypes from an incross of *yap1* heterozygous animals were performed blind under Nikon SMZ25 stereomicroscope. Images of hyaloid vessels of both eyes from 5 dpf animals were taken with spinning disk confocal microscope (40X objective) from the dorsal side of the eye.

49

3.2.22.   Secondary angiogenic sprouting analyses

yap1^{-/-};wwtr1^{+/-} embryos for secondary sprouting analyses were obtained from a cross between *yap1^{+/-};wwtr1^{+/-}* and *yap1^{+/-}* fish. These embryos can be sorted out based on the curved tail phenotype at 30-32 hpf (Figure 12B). The remaining siblings were picked at random and embedded in 1% low melting agarose for data and image acquisition followed by genotyping. Image acquisition was done with LSM800 confocal microscope (25X objective) at 48 and 72 hpf. To quantify *lyve1b*:DsRed positive intersomitic vessel (ISV) sprouts, 48 hpf animals were observed under the spinning disk confocal microscope with a 10X objective. We quantified *lyve1b*:DsRed positive ISVs spanning the upper trunk (along the yolk extension) and the lower trunk separately. At 72 hpf, *yap1^{-/-};wwtr1^{+/-}* with blood circulation and randomly sampled siblings were observed under the spinning disk confocal microscope with a 25X objective to quantify the number of vISVs and parachordal lymphangioblasts (PLs). PLs are *lyve1b*:DsRed positive vessels on the horizontal myoseptum, while vISVs are lumenized *lyve1b*:DsRed positive ISV structures. The same quantification strategy was employed for *vegfc^{+/-}* larvae. For *sih* morpholino experiment, 1 ng of *sih* and control morpholinos were injected into 1-cell stage embryos. Quantification of vISVs and PLs were done as described for the *yap1/wwtr1* mutants, except vISVs of *sih* morphants were not lumenized.

3.2.23.   Genotyping *vegfc^{hu6410}*

Two PCR reactions were performed per DNA sample. The first reaction amplifies the WT allele (primer pairs: 1_vegfc_WT and 2_vegfc_WT), while the second reaction amplifies the *vegfc^{hu6410}* allele (primer pairs: 1_vegfc_hu6410 and 2_vegfc_hu6410). The PCR reaction mix was as follows:

Reagent	Volume (μL)
KAPA 2G master mix	5
DNA template	1
Premixed primer pairs (5 mM)	0.8
Water	3.2
Total	10

The amplification cycles were:

Step	Temperature (°C)	Time	Description
1	95	5 minutes	Template denaturation
2	95	10 seconds	PCR amplification, 40 cycles
	60	15 seconds	
	72	5 seconds	

The products were resolved by gel electrophoresis on a 1% gel.

3.2.24.   Real-time PCR (qPCR)

3.2.24.1.   Sample collection

Single embryos were crushed in 20 µL of Trizol and mechanically dissociated with a filtered pipette tip. The samples were frozen in -80°C overnight. For *yap1$^{-/-}$;wwtr1$^{+/-}$* experiments, the heads were dissected out for genotyping and the trunks were homogenized in Trizol. Trunk samples from the genotypes of interest were kept for further analyses. For *sih* and control morphant samples, only the trunks were homogenized in Trizol.

3.2.24.2.   RNA isolation and cDNA synthesis

An equal volume of ethanol was added to the frozen Trizol mix. This mixture is then passed through a Direct-zol RNA micro prep kit. The first flow-through can be used for DNA isolation and genotyping if necessary. The remaining steps of RNA isolation were according to manufacturer's instructions (including in-column DNase digestion). 6 µL of nuclease free water was used to elute the RNA. A fixed amount of RNA for each sample was used for the reverse-transcriptase reaction with the High-Capacity RNA-to-cDNA kit or Maxima First Strand cDNA Synthesis Kit for RT-qPCR following manufacturer's instructions. cDNA was stored in -80°C for long term storage.

3.2.24.3.   Amplification and analysis

The qPCR reaction mix was as follows:

Reagent	Volume (µL)
SYBR Green PCR master mix	5
cDNA template	1

Premixed primer pairs (5 mM)	0.8
Water	3.2
Total	10

The amplification cycles were programmed as below:

Step	Temperature (°C)	Time	Description
1	95	10 minutes	Polymerase activation
2	95	10 seconds	PCR amplification, 40 cycles
	60	15 seconds	
	72	10 seconds	
3	55	15 seconds	HRM analysis
	95	15 seconds	

The C_T values were determined with a linear threshold setting. All C_T values were normalized against the C_T values of *rpl13* to obtain the ΔC_T values. The $\Delta\Delta C_T$ values reflect the $\log_2$(fold-change) of a given gene, which were used to plot the graphs. Two-sample t-tests were used to compare the ΔC_T values of mutant/morphant to the ΔC_T values of controls.

3.2.25.   Cryosections of adult hearts

Images of adult fish were taken with Nikon SMZ25 system before they were sacrificed for experiments. Adult hearts were surgically removed and imaged with Nikon SMZ25. Hearts were fixed in 4% PFA for 45 minutes at 4°C, followed by a sucrose gradient before embedding in OCT. Cryosections of 15 µm thick were obtained and stored in -20°C before performing AFOG staining by Beate Grohmann.

3.2.26.   Transplantation

Mutant and heterozygous embryos were obtained from a cross between *wwtr1$^{-/-}$*; *Tg(myl7:mKate-CAAX)* (♂) and *wwtr1$^{+/-}$*; *Tg(tp1:Venus-PEST)* (♀). WT embryos were obtained from a cross between *Tg(myl7:BFP-CAAX)* and *Tg(tp1:Venus-PEST)*. Donors were kept alive to screen for presence of the transgenes as well as for genotyping (when applicable). Both transgenes must be present in donors, but only the *Tg(tp1:Venus-PEST)* transgene was needed in hosts. When analyzing distribution of donor cardiomyocytes

between compact and trabecular layer (Figure 28A and B), only the *myl7* transgenics were examined.

3.2.27. Wwtr1 expression analyses

Images were acquired on the Spinning Disk and analyzed with Imaris. Individual nuclei were selected using the Surface creation tool on DAPI channel. Nuclei of trabecular cardiomyocytes were manually selected, as well as nuclei of adjacent compact cardiomyocytes. These cardiomyocytes can be identified with the aid of the *Tg(myl7:mKate-CAAX)* marker. The average intensity of Wwtr1 channel were extracted out and analyzed in R.

To calculate the correlation of cardiomyocyte size to Wwtr1 immunostaining intensity, the mKate-CAAX membrane marker was used to delineate the apical surface area of individual cardiomyocytes. The area, perimeter, circularity, aspect ratio were measured and correlated to the nuclear Wwtr1 immunostaining intensity of individual cardiomyocytes.

3.2.28. Analyzing trabecular cardiomyocytes

Images were acquired on the Spinning Disk and processed in Imaris. To obtain surface reconstruction of the *Tg(myl7:EGFP-Hsa.HRAS)* signal, we used the Normal Shading function in Volume tool. To analyze number of total ventricular cardiomyocytes, we utilized *Tg(myl7:EGFP-Hsa.HRAS)* in conjunction with *Tg(myl7:DsRed2-NLS)*. The same animal was followed for all three time points: 58, 72 and 96 hpf. All nuclei were selected with the "Spot Creation" tool. Cardiomyocytes in the atrium, atrio-ventricular canal (AVC), and outflow tract were manually excluded. For simplicity, a binary assignment of ventricular cardiomyocytes was made: "Compact wall cardiomyocytes" was defined as the outermost layer of cardiomyocytes, otherwise cardiomyocytes were assigned to "Trabecular cardiomyocytes".

Mosaic analyses of trabecular cardiomyocyte morphology was done by injecting the pTol2 *myl7:mKate* plasmid into one-cell stage embryos from an incross of *wwtr1*^{+/-} fish. Trabecular cardiomyocytes expressing mKate were selected with the "Surface Creation" tool to apply channel masking on the LA-GFP channel.

3.2.29. Analyzing myocardial *tp1* activity

Images were acquired on the Spinning Disk and analyzed with Imaris. Maximum intensity projections were made to count the number of cardiomyocytes that express the *tp1* Notch reporter.

To test which domain of Wwtr1 is required for myocardial Notch signaling, the various Wwtr1 constructs were injected into one-cell stage embryos from an incross of *wwtr1*$^{+/-}$ animals. *tp1*$^{+}$ hearts were hearts that show at least one *tp1*$^{+}$ cardiomyocyte, otherwise assigned as *tp1*$^{-}$.

For transplantation experiment, we relied on the donor/host cardiomyocyte marker to assign *tp1*$^{+}$ donor/host cardiomyocytes. As donor animals were pre-screened for presence of both transgenics marking cardiomyocytes and reporting *tp1* activity, we can infer if a *tp1*$^{+}$ cardiomyocyte belongs to the host, if the host cardiomyocyte marker is absent.

3.2.30. Quantifying cardiomyocyte distribution between compact and trabecular layer

As the transplant and the mosaic CAWwtr1 experiments lacked a nuclear marker, strategy to quantify number of cardiomyocytes in the compact versus the trabecular layer has to be modified. As cardiomyocytes express transgenes that mark the membranes (EGFP-Hsa.HRAS, mKate-CAAX or BFP-CAAX), we carefully classified outer-curvature ventricular cardiomyocytes as "compact" or "trabecular" through the z-stacks. "Compact" cardiomyocytes are cells on the outermost layer, otherwise classified as "trabecular".

3.2.31. Cortical actin thickness

Images were acquired with the Spinning Disk and analyzed on Fiji. A background subtraction is applied on LA-GFP channel using a 30 pixel rolling ball radius. A maximum intensity projection was generated followed by an automatic binary threshold of the gray values. We drew lines perpendicular to the cortical actin, sampling across the whole ventricular outer-curvature wall, to generate a kymograph for calculation of cortical actin thickness.

3.2.32. "Tilting" extent of cardiomyocytes

Images were acquired with the Spinning Disk and analyzed on Fiji. First, a maximum intensity projection of the mKate-CAAX (cardiomyocyte membranes) and Cdh2-EGFP (N-

cadherin) channels were generated separately. Cardiomyocyte membranes were manually drawn on the mKate-CAAX channel to demarcate individual cells as a Region of Interest (ROI) and to calculate the "total area". The ROI is then applied on the Cdh2-EGFP channel to guide selection of the "tilt area" (see Fig. 30F for schematic).

3.2.33.   RNA-sequencing (RNAseq)

Embryos from an incross of *wwtr1*$^{+/-}$ fish were grown to 48 hpf. The fin-fold of these embryos were dissected out for genotyping. WT and mutant siblings were identified and placed into separate dishes. Hearts were isolated starting from 57 hpf, for over a maximum of 2 hours. Collections were made over 5 separate occasions to obtain 23 hearts per biological replicate (3 WT and mutant biological replicates each). Collection order was randomized over the genotype and biological replicates, and was never identical between collection sessions. Embryos were dissected in 1X MBS (protocol provided by David Kimelman). Isolated hearts were snap frozen in liquid nitrogen and stored overnight in -80 °C. Qiazol solution (Qiagen) was added followed by pipetting to mechanically dissociate the tissue. The samples were then passed through QIAshredder homogenizer column (Qiagen) followed by RNA extraction with miRNeasy micro kit (Qiagen). In-column DNase digestion was performed to eliminate DNA contamination. RNA and library preparation integrity were verified with a BioAnalyzer 2100 (Agilent) or LabChip Gx Touch 24 (Perkin Elmer). 6.5 ng of total RNA was used as input for Pico Input Mammalian (Takara Clontech). Sequencing was performed on the NextSeq500 instrument (Illumina) using v2 chemistry, resulting in minimum of 30M reads per library with 1x75bp single end setup. The resulting raw reads were assessed for quality, adapter content and duplication rates with FastQC (Andrews S. 2010, FastQC: a quality control tool for high throughput sequence data. Available online at: http://www.bioinformatics.babraham.ac.uk/projects/fastqc). Reaper version 13-100 was employed to trim reads after a quality drop below a mean of Q20 in a window of 10 nucleotides (Davis et al., 2013). Only reads between 30 and 75 nucleotides in length were cleared for further analyses. Trimmed and filtered reads were aligned against the Ensembl Zebrafish genome version DanRer10 (GRCz10.87) using STAR 2.4.0a with the parameter "--outFilterMismatchNoverLmax 0.1" to increase the maximum ratio of mismatches to mapped length to 10% (Dobin et al., 2013). The number of reads aligning to genes was counted with featureCounts 1.4.5-p1 tool from the Subread package (Liao et al., 2014). Only reads mapping at least partially inside exons were admitted and aggregated per gene. Reads overlapping multiple genes or aligning to multiple regions were excluded. Differentially

expressed genes were identified using DESeq2 version 1.62 (Love et al., 2014). Only genes with a combined minimum mean of 5 reads were used for subsequent analyses. The Ensembl annotation was enriched with UniProt data (release 24.03.2017) based on Ensembl gene identifiers (Activities at the Universal Protein Resource (UniProt)). Genes are classified to four groups by the following thresholds: significantly differentially expressed: ± 1.0 log$_2$FC (fold-change) and adjusted $P < 0.05$; moderately differentially expressed: adjusted $P < 0.05$; not significantly differentially expressed: ± 1.0 log$_2$FC; not differentially expressed otherwise.

3.2.34. Podxl localization analysis

Hearts were imaged with the Spinning Disk and analyzed on Zen Blue software. We analyzed 20 μm of sagittal sections surrounding the mid-sagittal plane. Each section was 1 μm thick. Method to quantify apical constriction as described before (Jiménez-Amilburu et al., 2016).

4. RESULTS

Part of chapter "4. RESULTS" will be used in the following unpublished manuscripts:

1. **Lai, J. K. H.**, Collins, M. M., Jiménez-Amilburu, V., Günther, S., Maischein, H.-M. & Stainier, D. Y. R. (submitted). Multiple roles for the Hippo pathway effector Wwtr1 in cardiac wall maturation in zebrafish. *Development.*

2. Kimelman, D., Smith, N. L., **Lai, J. K. H.** & Stainier, D. Y. R. (in revision). Regulation of posterior body and ectodermal morphogenesis in zebrafish by localized Yap1 and Wwtr1 (Taz). *eLife.*

3. Astone, M., **Lai, J. K. H.**, Dupont, S., Stainier, D. Y. R., Argenton, F. & Vettori, A. (resubmission in preparation). Hippo pathway transducers Yap1/Wwtr1 control secondary sprouting during vascular development. *Development*.

Results produced by a collaborator will not be displayed as figures, instead will be described with text accompanied by appropriate citations of one of these three manuscripts.

4.1. Generation of zebrafish *yap1* and *wwtr1* mutants

I generated zebrafish mutants for both *yap1* and *wwtr1* genes to investigate their roles during vertebrate development. Here, I designed guide RNAs (gRNA) against the first exon of zebrafish *yap1* and the second exon of zebrafish *wwtr1*. In my screening of F0 founders, a variety of lesions were isolated from a single clutch of F1 spawnlings. A frame-shift mutation is desired to potentially introduce nonsense-mediated decay. In my screen, I have identified a *yap1* allele carrying a 41 bp deletion (designated *yap1^{bns19}*), and a *wwtr1* allele carrying a 29 bp insertion (designated *wwtr1^{bns35}*) (Figure 4A). These alleles can be genotyped by PCR followed by separation by gel electrophoresis (Figure 4B, C). The sequences of these alleles were confirmed by TA cloning followed by Sanger Sequencing (data not shown). To evaluate the stability of the transcripts of these alleles, I performed real-time PCR (qPCR) for these genes in the respective mutants. I find that the abundance of *yap1* and *wwtr1* transcripts correlates with their respective genotypes, i.e. the abundance of the mutant transcripts are lower than their WT counterparts (Figure 4D). Additionally, I do not observe an upregulation of *yap1* and *wwtr1* in a reciprocal manner (i.e. *yap1* is upregulated in *wwtr1* mutants) (Figure 4D).
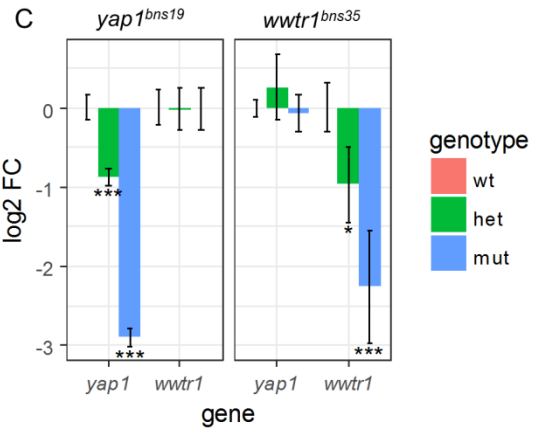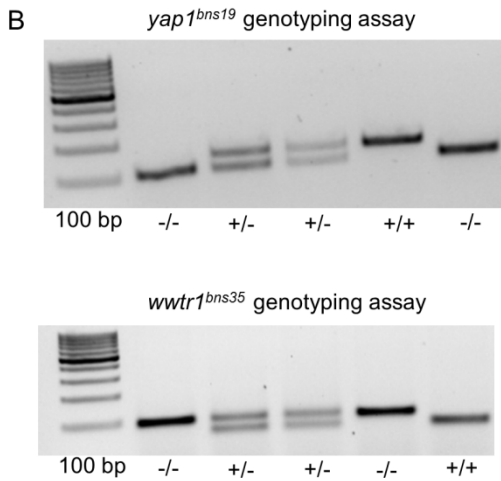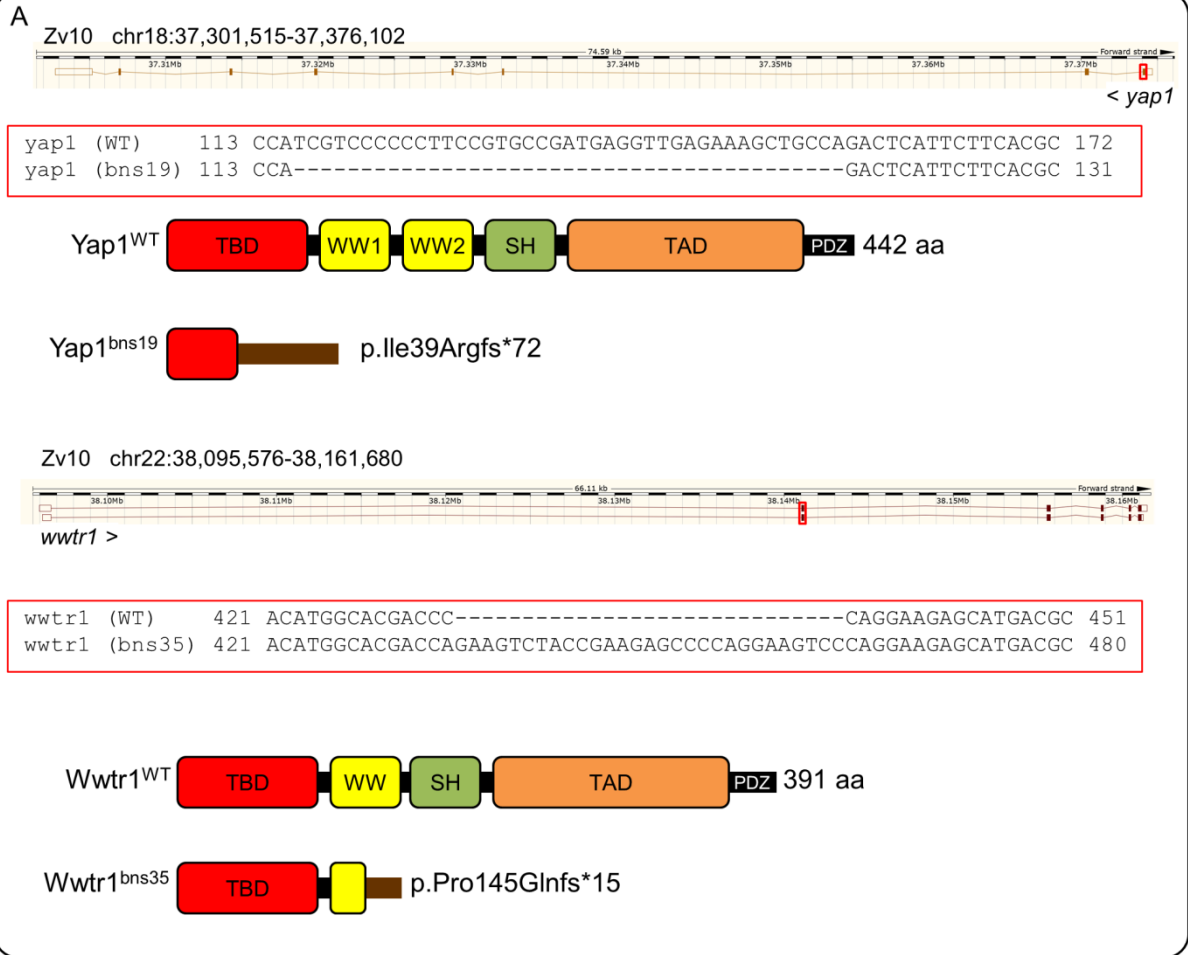
A

Zv10 chr18:37,301,515-37,376,102

```
yap1 (WT)     113  CCATCGTCCCCCCTTCCGTGCCGATGAGGTTGAGAAAGCTGCCAGACTCATTCTTCACGC  172
yap1 (bns19)  113  CCA------------------------------------------GACTCATTCTTCACGC  131
```

Yap1^WT [TBD] [WW1] [WW2] [SH] [TAD] [PDZ] 442 aa

Yap1^bns19 [TBD] ■ p.Ile39Argfs*72

Zv10 chr22:38,095,576-38,161,680

wwtr1 >

```
wwtr1 (WT)     421  ACATGGCACGACCC----------------------------CAGGAAGAGCATGACGC  451
wwtr1 (bns35)  421  ACATGGCACGACCAGAAGTCTACCGAAGAGCCCCAGGAAGTCCCAGGAAGAGCATGACGC  480
```

Wwtr1^WT [TBD] [WW] [SH] [TAD] [PDZ] 391 aa

Wwtr1^bns35 [TBD] [■] p.Pro145Glnfs*15

B

yap1^bns19 genotyping assay

100 bp   -/-   +/-   +/-   +/+   -/-

wwtr1^bns35 genotyping assay

100 bp   -/-   +/-   +/-   -/-   +/+

C

Figure 4. *yap1* and *wwtr1* zebrafish mutants. (A) Schematic of the *yap1*^{bns19} and *wwtr1*^{bns35} alleles generated by CRISPR/CAS9 and their predicted truncated protein products. TBD - Tead-binding domain; WW1/2 - WW domains; SH - Src homology domain; TAD - transcription activation domain; PDZ - PDZ binding motif. (B) Example genotyping assay by PCR followed by separation by gel electrophoresis on a 2% gel. (C) Relative expression of *yap1* and *wwtr1* in *yap1* and *wwtr1* mutants at 30 hpf. Expression levels are normalized to *rpl13* and n = 4 for each genotypes.

4.1.1. Concurrent loss of Yap1 and Wwtr1 result in embryos lacking posterior body extension

To obtain double homozygous mutants for *yap1* and *wwtr1* (i.e. *yap1*$^{-/-}$;*wwtr1*$^{-/-}$), I made an incross between double heterozygotes. At 1 dpf, about 1/16 of embryos exhibit severe developmental defects and the body appears necrotic (Figure 5A). In addition, the tails of *yap1*$^{-/-}$;*wwtr1*$^{-/-}$ embryos did not extend out, reminiscent of the *kugelig* mutants, although the phenotype of *yap1*$^{-/-}$;*wwtr1*$^{-/-}$ embryos are more severe in that the tail bud appear to be less developed. To further characterize this phenotype, I performed time-lapse experiments to study the developmental progression of these mutants. At about 14 somite stage (ss), siblings have executed eversion of the tail bud, 'pinching' of the yolk sac and formation of the yolk tube while straightening of the posterior body (Figure 5B). However, this process does not take place in the *yap1*$^{-/-}$;*wwtr1*$^{-/-}$ embryos (Figure 5B). Furthermore, I observed cell death specifically in the enveloping layer (EVL) (Figure 6), suggesting that Yap1/Wwtr1 plays a role for EVL survival. Additionally, I observed an undulating notochord in *yap1*$^{-/-}$;*wwtr1*$^{+/-}$ and *yap1*$^{-/-}$;*wwtr1*$^{-/-}$ embryos by 20 hpf (Figures 5A, 7) (Kimelman et al., in revision).

I then tested whether the somite clock is perturbed in the double *yap1;wwtr1* mutants by performing whole mount *in situ* hybridization (WISH) with a *myod* anti-sense probe. With the help of Dr. Michelle Collins we counted the number of somites from embryos collected at the 6-8 and 14-16 ss. We found that the number of somites between mutants and siblings are roughly equal (Figure 8), suggesting that the somite clock remains robust despite massive morphological deformities in the double mutants.
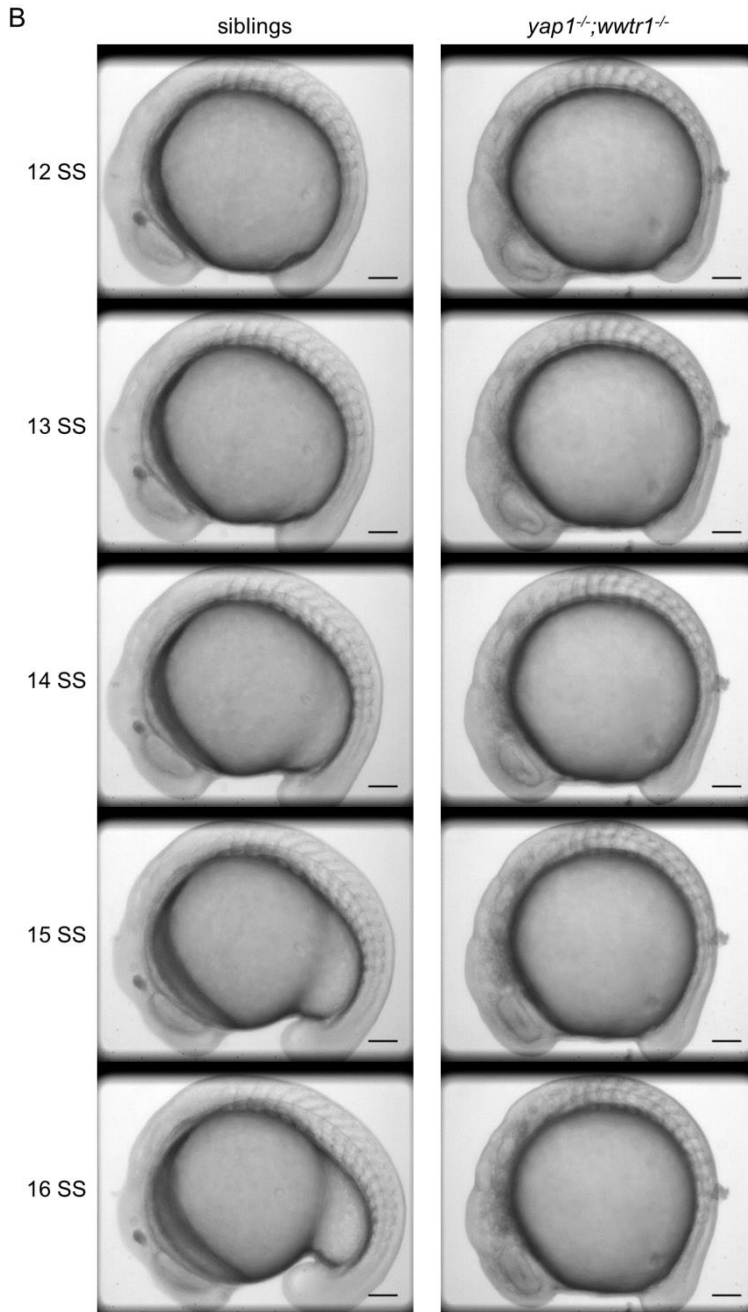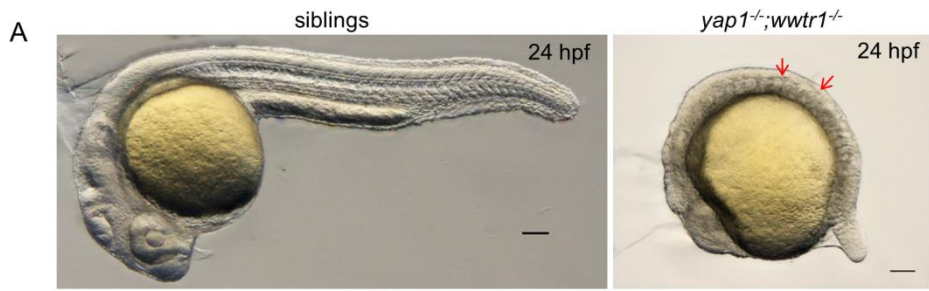
A

siblings   *yap1⁻/⁻;wwtr1⁻/⁻*
24 hpf   24 hpf

B

siblings   *yap1⁻/⁻;wwtr1⁻/⁻*

12 SS

13 SS

14 SS

15 SS

16 SS

Figure 5. Gross morphological phenotype of double *yap1;wwtr1* mutants. (A) Still photographs of 24 hpf sibling and double *yap1;wwtr1* mutants. Red arrows point to undulating notochord in mutants. (B) Selected frames from a timelapse experiments of siblings and mutants. Scale bars, 100 µm. SS - somite stage.
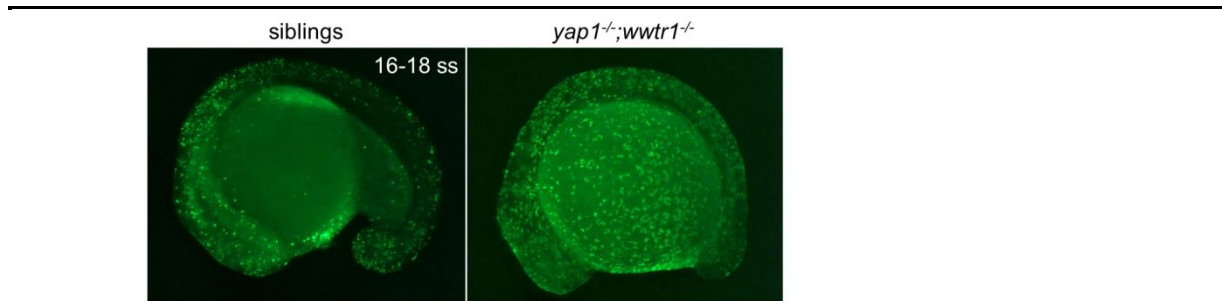

Figure 6. Cell death in EVL of double *yap1;wwtr1* mutants. Aberrant cell death is predominantly observed in cells of the EVL of double *yap1;wwtr1* mutants, compared to siblings. Green signal is from acridine orange dye that has intercalated with genomic DNA of dying cells.
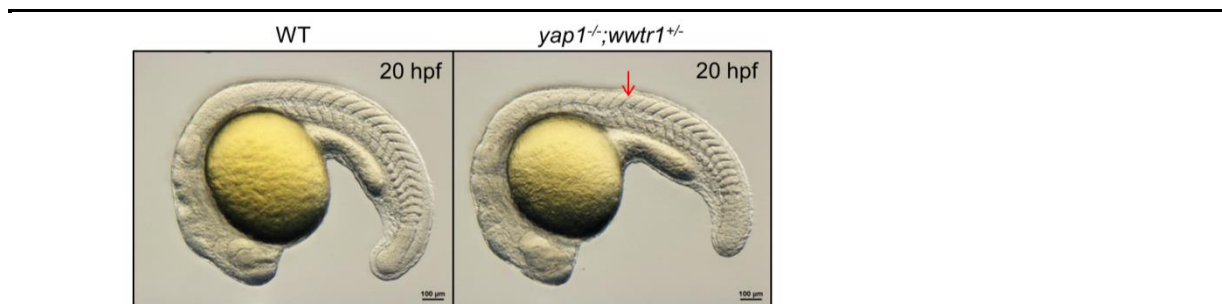
Figure 7. *yap1$^{-/-}$;wwtr1$^{+/-}$* mutants exhibit an undulating notochord at 20 hpf. Similar to the double *yap1;wwtr1* mutants, the compound *yap1$^{-/-}$;wwtr1$^{+/-}$* mutants have an undulating notochord (red arrow) by 20 hpf. Scale bars, 100 µm.
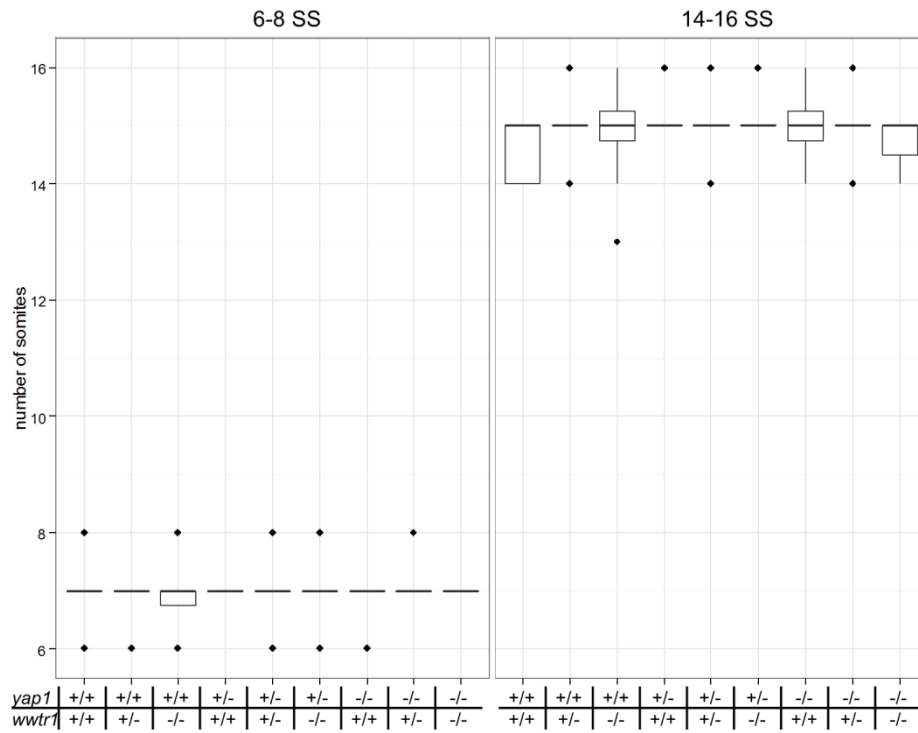
Figure 8. The somite clock remains robust in the double *yap1;wwtr1* mutants. The number of somites as revealed by a *myod* anti-sense probe from fixed embryos raised in 28.5°C incubators.

4.1.2. Expression of Yap1 and Wwtr1 in the developing zebrafish embryo

From available public datasets, *yap1* is maternally contributed but not *wwtr1* (Figure 9A). As Yap1 and Wwtr1 are tightly regulated at the post-translational level (Johnson and Halder, 2014), it will be informative to evaluate the spatio-temporal expression at the protein level. Therefore, I investigated the expression of these proteins by whole mount immunostaining. To understand the phenotypes of the *yap1⁻/⁻;wwtr1⁻/⁻* embryos, I will focus my characterization on the posterior body. For the purpose of this thesis, I will characterize the expression of Wwtr1, as Professor David Kimelman has characterized the expression of Yap1 as part of a collaboration (Kimelman et al., in revision). Although the antibody I have used is a rabbit monoclonal antibody raised from a human C-terminal WWTR1 peptide, it recognizes both YAP1 and WWTR1 antigens. However, in zebrafish, the antibody specifically recognizes Wwtr1 (Figure 9B), as similarly shown by another research group (Miesfeld et al., 2015a). Strikingly, I observed that Wwtr1 is primarily localized to the nuclei of the notochord, adaxial cells, anterior somites (Figure 9C), floor plate, hypochord (Figure 9D), and epidermis (Figure 9E). Curiously, the nuclear-localization of Wwtr1 in the notochord is invariantly limited from the posterior end of the embryo up to the third newest somite (S-III) (Figure 9C).
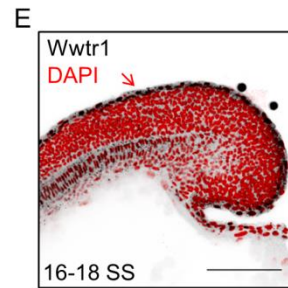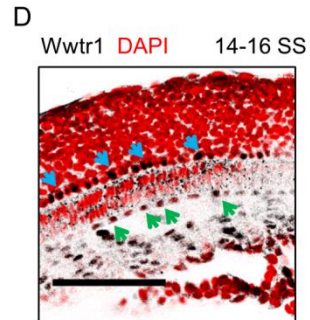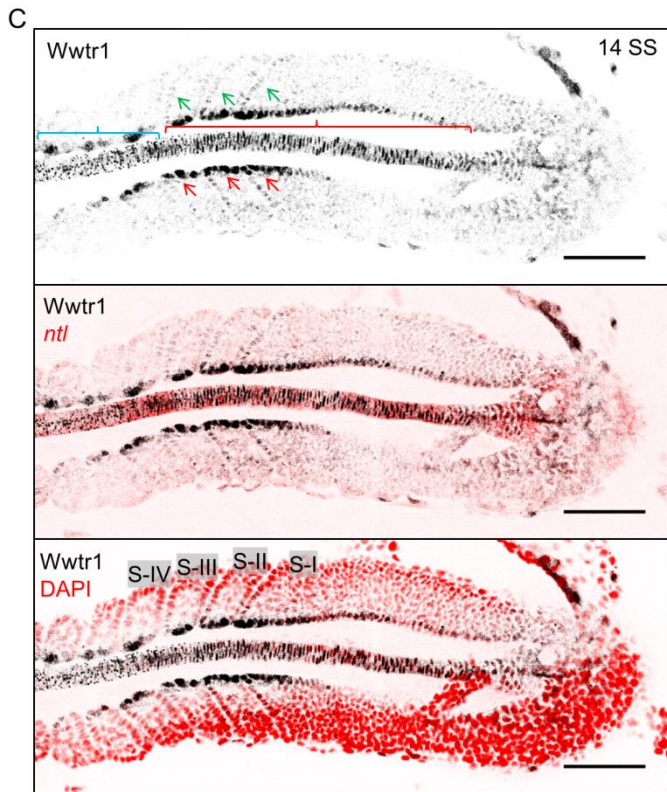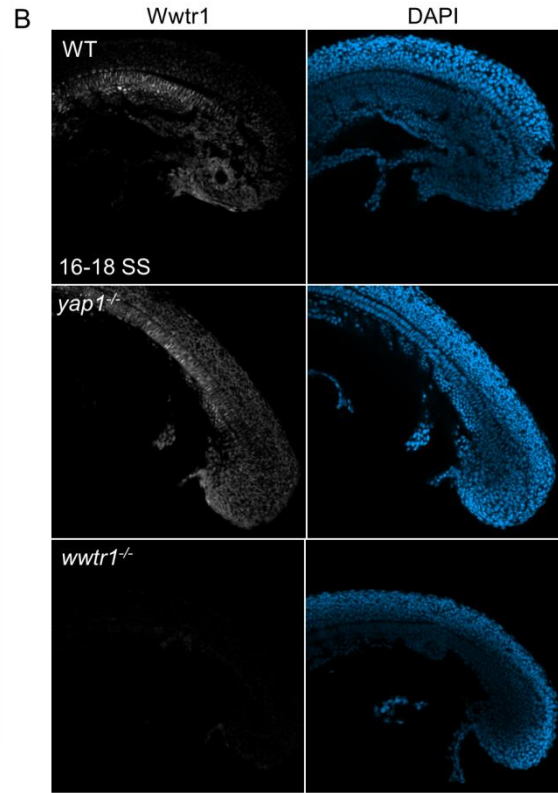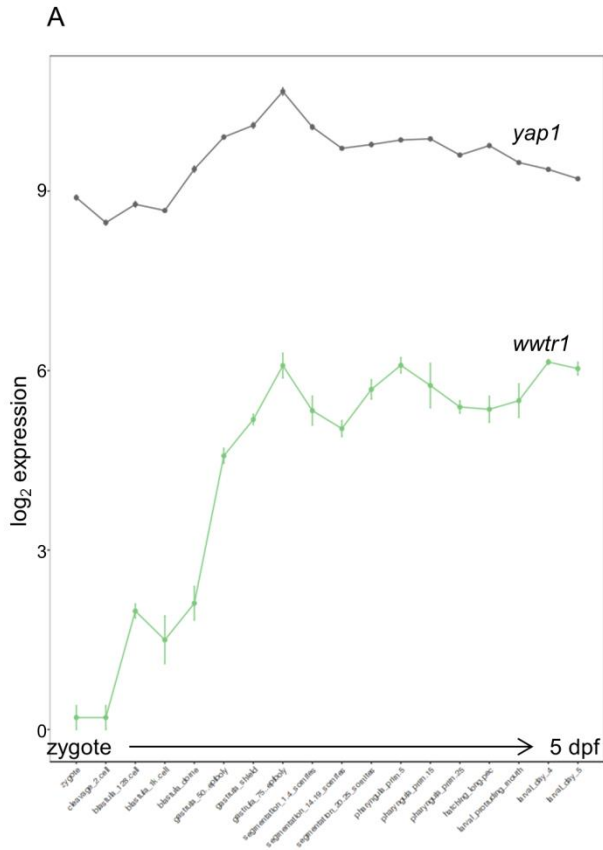
A

B

C

D

E

Figure 9. Expression of Wwtr1 in the developing zebrafish embryo. (A) Transcript abundance of *yap1* and *wwtr1* mRNA at various stages of zebrafish development. Data taken from an in-house database. (B) Whole mount immunostaining with an antibody against human YAP1/WWTR1 in zebrafish. Antibody is reactive in WT and *yap1*^{-/-} samples but not *wwtr1*^{-/-} samples. Lateral flat mount, anterior to the left, and dorsal to the top. (C) Flat mounts of 14 SS WT embryos stained for Wwtr1. Nuclear Wwtr1 immunostaining is evident in the notochord from the third newest somite (S-III) all the way to the caudal end of the notochord (red brackets), notochord rostral to the level of S-III do not show nuclear Wwtr1 (blue brackets). Nuclear Wwtr1 is also evident in the anterior somites (green arrows) and adaxial cells (red arrows). Anterior to the left. (D) Lateral flat mount of WT embryos show nuclear Wwtr1 in floor plate cells (blue arrows) and hypochord cells (green arrows). (E) Lateral flat mount of WT embryos show nuclear Wwtr1 in epidermis cells (red arrow).

4.2.   Role for Yap1/Wwtr1 in vascular development

4.2.1.   Expression of Hsa.CTGF reporter in the developing endothelium

YAP1 can respond to shear stress by relocalizing into the nuclei of endothelial cells in culture and *in vivo* (Nakajima et al., 2017; Sabine et al., 2015; Wang et al., 2016). However, expression of *yap1/wwtr1* in endothelial cells by WISH or by immunostaining of whole mount embryos was not detected (based on our work and personal communication with Professor Naoki Mochizuki). Nevertheless, a Tead reporter line, in which a TEAD2 DNA binding domain was substituted for a Gal4 DNA binding domain, was active in the endothelium indicating that Yap1/Wwtr1 was active in the zebrafish endothelium *in vivo* (Nakajima et al., 2017). In a collaboration with the laboratory of Professor Francesco Argenton, we investigated the expression of a reporter line made in his laboratory. The reporter is a promoter from the human *CTGF* gene, a canonical target of YAP1/WWTR1. The reporter line is designated *Tg(Hsa.CTGF:nlsmCherry)[ia49]*. The reporter is ubiquitously expressed, including the endothelium (Figure 10A). To test whether the reporter is a proxy readout for Yap1/Wwtr1 activity in the endothelium, I crossed the reporter line into the *yap1;wwtr1* mutant background. I observed a modest decrease in reporter intensity in the endothelium of *yap1*^{-/-} and *wwtr1*^{-/-} embryos (Figure 10B). Only embryos in the *yap1*^{-/-} background showed statistical significance. However, the *Hsa.CTGF:*nlsmCherry expression trend was unexpected, as I had anticipated lower *Hsa.CTGF:*nlsmCherry expression in the

compound mutants than the single mutants. Additionally, Dr. Andrea Vettori has observed that this reporter line is downregulated in the endothelium of *sih* (*tnnt2a*) morphants which lacks blood circulation (Astone et al., resubmission in preparation). These data corroborate with the Tead reporter line developed in the Mochizuki Lab (Nakajima et al., 2017). Taken together, the endothelium is responsive to blood flow *in vivo* and modulates Yap1/Wwtr1 activity.

4.2.2.   *yap1*$^{-/-}$ animals show truncation of cranial vasculature and fewer hyaloid vessels

I did not observe any overt trunk vasculature phenotypes in zygotic and maternal zygotic *yap1*$^{-/-}$ larvae (Figure 11A), as well as *yap1*$^{+/-}$*;wwtr1*$^{-/-}$ larvae (Figure 11B). Instead, I observed that the cranial vasculature network of *yap1*$^{-/-}$ animals is truncated (Figure 11C). Additionally, the hyaloid vessels are fewer. However as some *yap1*$^{-/-}$ eyes exhibit coloboma, in which the optic fissure did not close completely, these eyes have even fewer hyaloid vessels (Figure 11D).
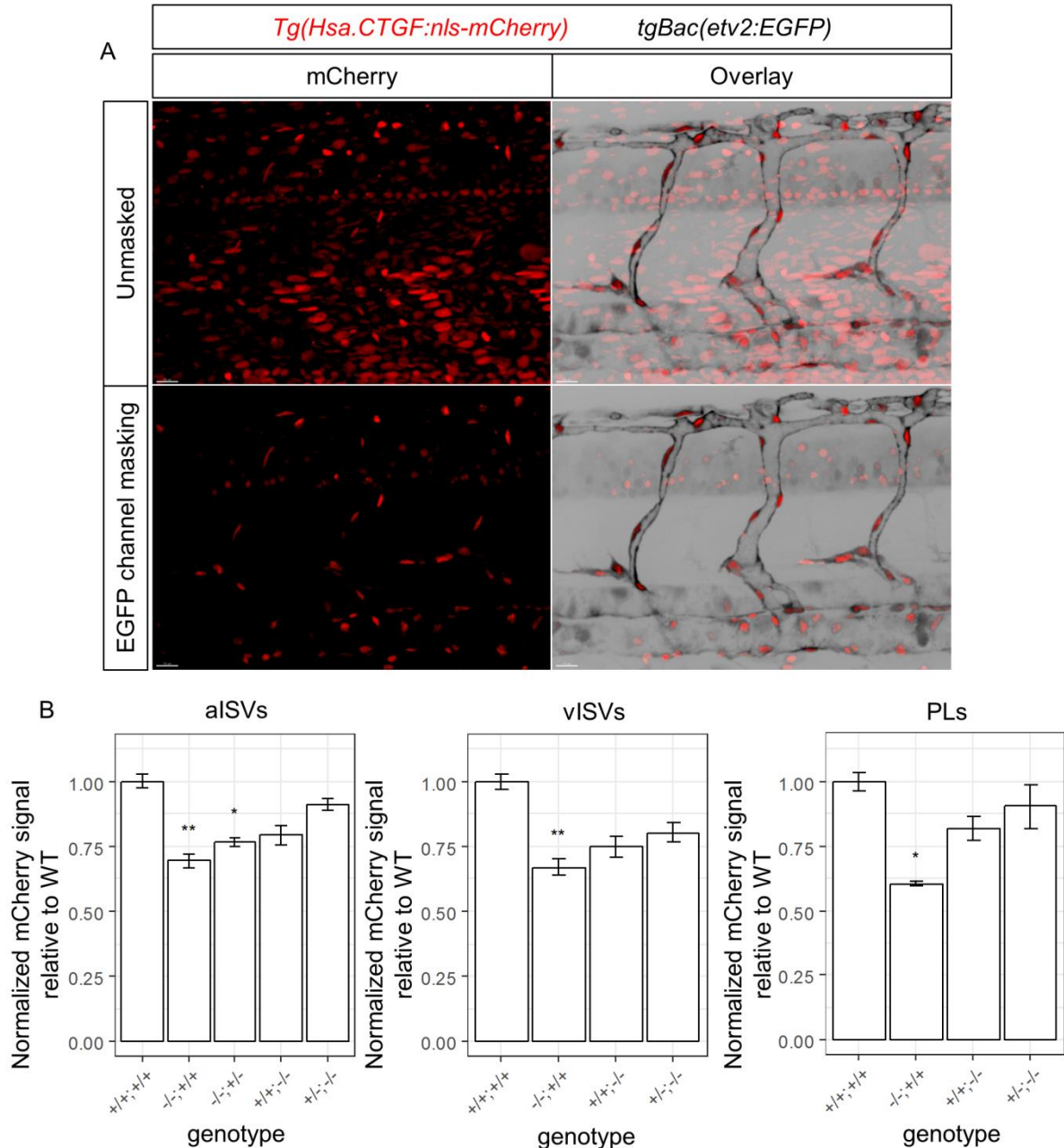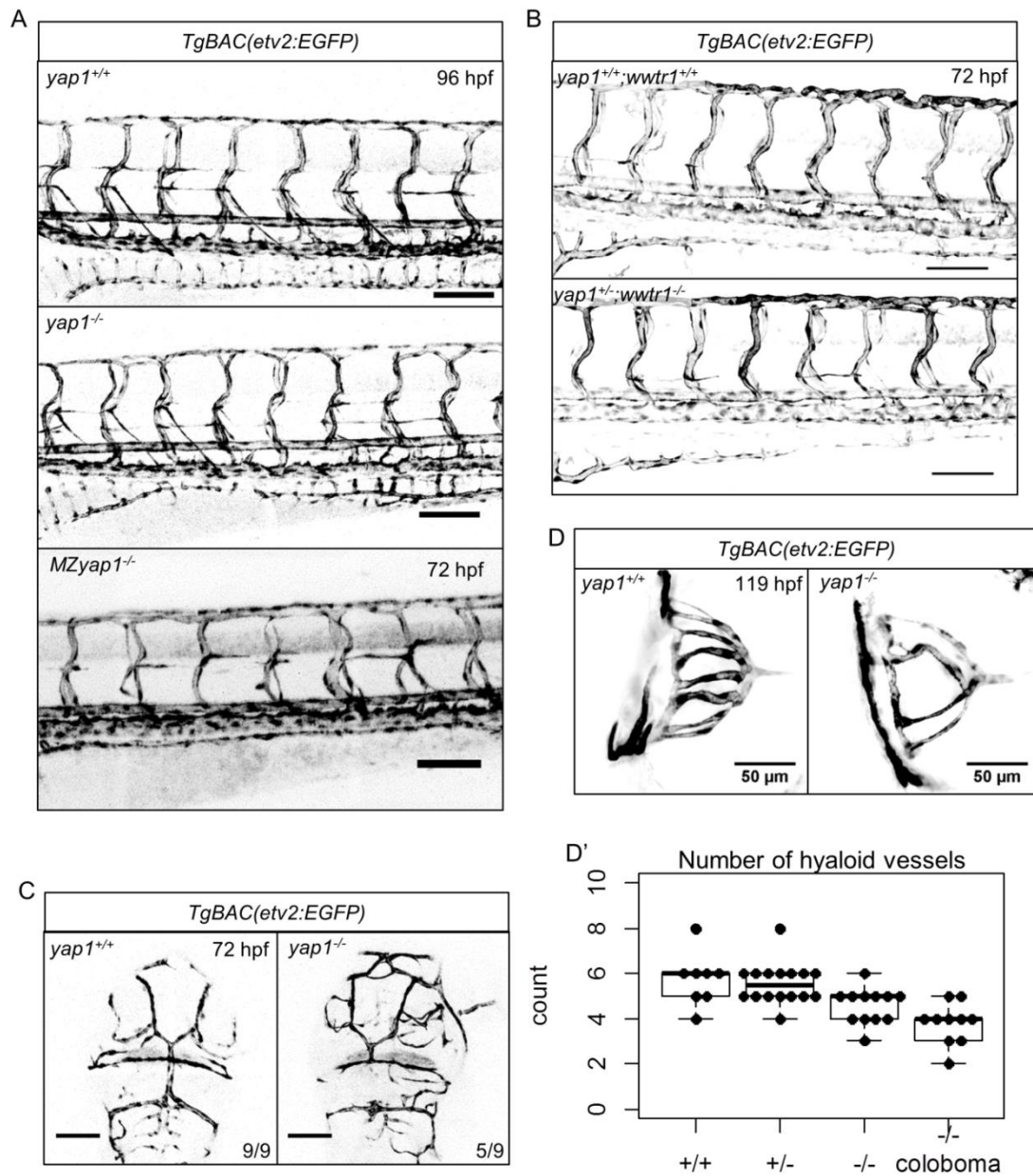
Figure 10. Endothelial cells express the *Hsa.CTGF* reporter and is reduced in *yap1*$^{-/-}$ endothelial cells. (A) Maximum intensity projections of zebrafish trunks expressing *Hsa.CTGF:*nls-mCherry and an endothelial reporter, *etv2*:EGFP. The endothelial reporter was used to demarcate the endothelium as a region of interest (channel masking) to highlight the expression of the *Hsa.CTGF* reporter in endothelial cells. (B) Quantification of normalized *Hsa.CTGF*:nls-mCherry signal in the endothelium of 48 hpf embryos from different combinations of *yap1* and *wwtr1* genotypes. Double *yap1;wwtr1* mutants are not quantified as they are not viable by 48 hpf. Quantification of vISVs and PLs from *yap1*$^{-/-}$;*wwtr1*$^{+/-}$ embryos are missing as these mutants have severely reduced numbers of vISVs and PLs. * - $P < 0.05$; ** - $P < 0.01$ by two-sample t-test against WT samples.

Figure 11. Vascular phenotypes of *yap1^-/-* and *wwtr1^-/-* mutants. (A) Maximum intensity projections of trunks showing trunk vascular pattern of 96 hpf WT and zygotic *yap1^-/-* sibling larvae, as well as 72 hpf maternal zygotic (MZ) *yap1^-/-* larvae. (B) Maximum intensity projections of trunks showing trunk vascular pattern of 72 hpf WT and *yap1^+/-;wwtr1^-/-* sibling larvae. (C) Dorsal view of zebrafish heads revealing cranial vascular pattern of 72 hpf WT and *yap1^-/-* sibling larvae. Some *yap1^-/-* larvae exhibit defects in cranial vasculature patterning. (D) Dorsal view of zebrafish hyaloid vascular network from 119 hpf WT and *yap1^-/-* larvae. (D') Quantification of the number of hyaloid vessels. The *P*-value calculated by Poisson regression was just shy of significance. Scale bars, 100 μm, unless stated. (C), (D) and (D') will be used in a manuscript in preparation by Astone, et al. to be resubmitted to *Development*.

68

4.2.3. The compound $yap1^{-/-};wwtr1^{+/-}$ animals exhibit a posterior cardinal vein (PCV) that deviates from the midline and fewer secondary angiogenic sprouts

As Wwtr1 could play overlapping roles with Yap1, as evidenced by the example of posterior body development, I investigated whether the compound mutants (i.e. $yap1^{-/-};wwtr1^{+/-}$) would exhibit more severe vascular developmental defects. While it is ideal to investigate the double homozygous mutants, these mutant embryos die prematurely by 30 hpf. I found that some $yap1^{-/-};wwtr1^{+/-}$ embryos exhibit cardia bifida, and a majority of them did not establish any blood circulation (Figure 12A, A'). A small percentage (9% or 4/45) of these embryos show weak blood circulation (Figure 12A). Moreover, these mutants show distortions in the tail (Figure 12B).

At 30 hpf, I observed that the axial vessels, starting with the DA are properly formed and lumenized. However, some $yap1^{-/-};wwtr1^{+/-}$ embryos showed a PCV that deviated from the midline (Figure 12C, D). By 48 hpf, this PCV phenotype has worsened and become fully penetrant (Figure 12C, E). Moreover, I observe that the PCV appear to have 'split' into two separate lumens (Figures 12E, 13A-C). Concurrently, the distance between the DA and PCV, as well as the distance between the DA and neural tube (NT) of $yap1^{-/-};wwtr1^{+/-}$ animals are reduced (Figure 13D-F). I then investigated the segregation of the arterial and venous fate of the DA and PCV by WISH. Here, I observed that while the expression of *efnb2a*, an arterial marker, was not affected, the expression of *mrc1a*, a venous marker, had perdured in the DA of $yap1^{-/-};wwtr1^{+/-}$ embryos at 32 hpf (Figure 14). These data suggest that Yap1/Wwtr1 could be involved in PCV morphogenesis.
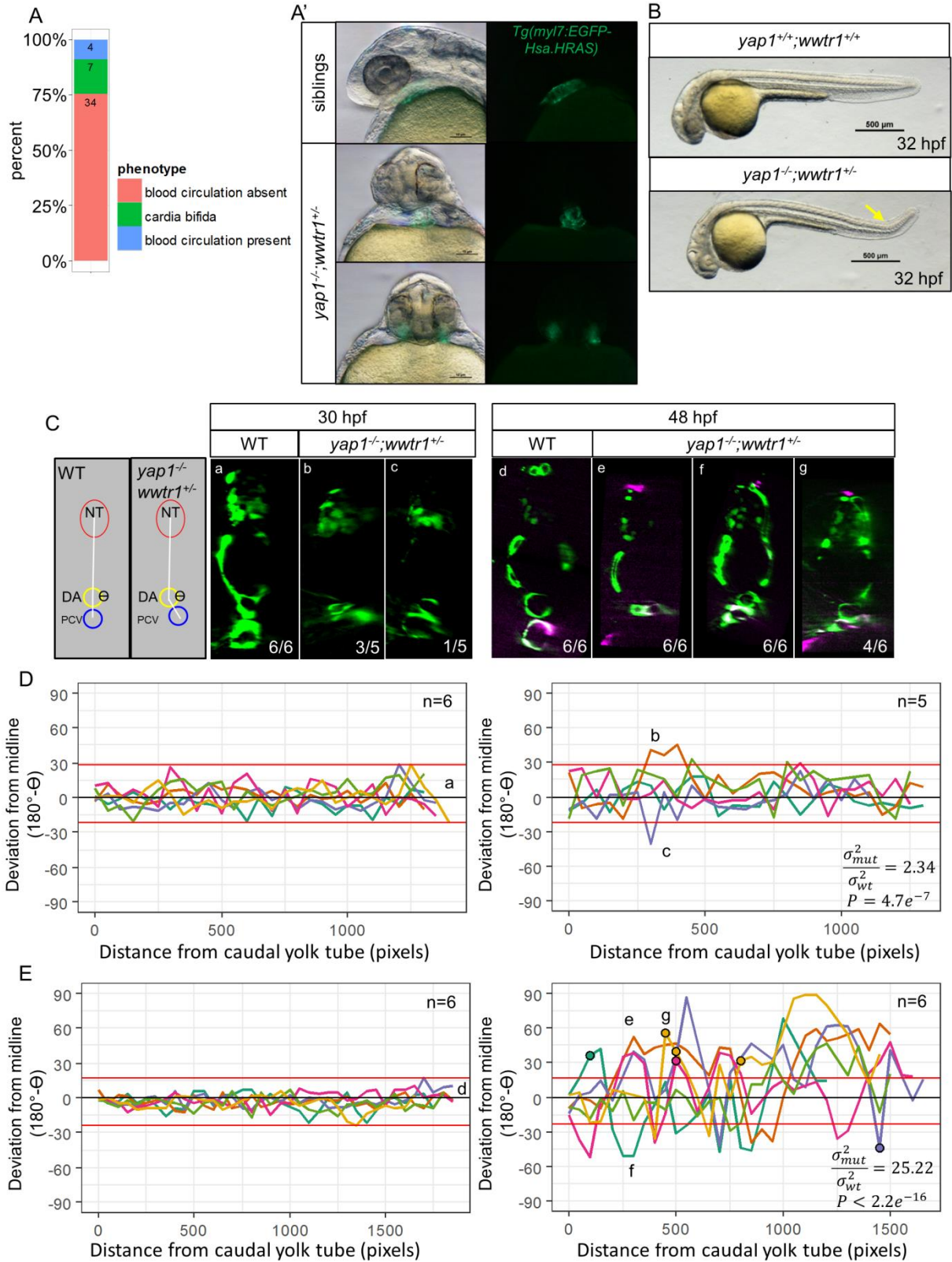
A

percent

phenotype
- blood circulation absent
- cardia bifida
- blood circulation present

A'

siblings

yap1⁻/⁻;wwtr1⁺/⁻

Tg(myl7:EGFP-Hsa.HRAS)

B

yap1⁺/⁺;wwtr1⁺/⁺

500 µm

32 hpf

yap1⁻/⁻;wwtr1⁺/⁻

500 µm

32 hpf

C

WT

yap1⁻/⁻ wwtr1⁺/⁻

NT

NT

DA

Θ

DA

Θ

PCV

PCV

30 hpf

WT | *yap1⁻/⁻;wwtr1⁺/⁻*

a | b | c

6/6 | 3/5 | 1/5

48 hpf

WT | *yap1⁻/⁻;wwtr1⁺/⁻*

d | e | f | g

6/6 | 6/6 | 6/6 | 4/6

D

Deviation from midline (180°-Θ)

Distance from caudal yolk tube (pixels)

n=6

a

$$\frac{\sigma^2_{mut}}{\sigma^2_{wt}} = 2.34$$
$$P = 4.7e^{-7}$$

n=5

b

c

E

Deviation from midline (180°-Θ)

Distance from caudal yolk tube (pixels)

n=6

d

n=6

e

g

f

$$\frac{\sigma^2_{mut}}{\sigma^2_{wt}} = 25.22$$
$$P < 2.2e^{-16}$$

70

Figure 12. Gross developmental and PCV phenotypes of *yap1^{-/-};wwtr1^{+/-}* embryos. (A) Quantification of 45 *yap1^{-/-};wwtr1^{+/-}* embryos exhibiting different cardiovascular defects. (A') Examples stereomicrographs of cardiac phenotypes of *yap1^{-/-};wwtr1^{+/-}* embryos that are unable to pump blood and establish a circulation. (B) *yap1^{-/-};wwtr1^{+/-}* embryos show a kinked tail by 32 hpf. (C) Schematic of confocal transverse sections of zebrafish trunks. The neural tube (NT), dorsal aorta (DA), and posterior cardinal vein (PCV) were demarcated with an ellipse tool and their center points are used to draw linear lines to connect each ellipse. The angle on the DA vertex (Θ) is the PCV angle of deviation from the midline. (C-a to C-g) examples confocal transverse sections of WT and *yap1^{-/-};wwtr1^{+/-}* trunks. Green signal is from *etv2*:EGFP transgenic and magental signal is from *lyve1b*:dsRed transgenic (48 hpf only). Quantification of (Θ) from serial transverse sections starting from the caudal end of the yolk tube at 30 hpf (D) and 48 hpf (E). Lower case letters correspond to the representative images in (C-a to C-g). Highlighted points in (E) are transverse sections that show "splitting" of the PCV as shown in (C-g). Some images in this figure will be used in a manuscript in preparation by Astone, et al. to be resubmitted to *Development*.
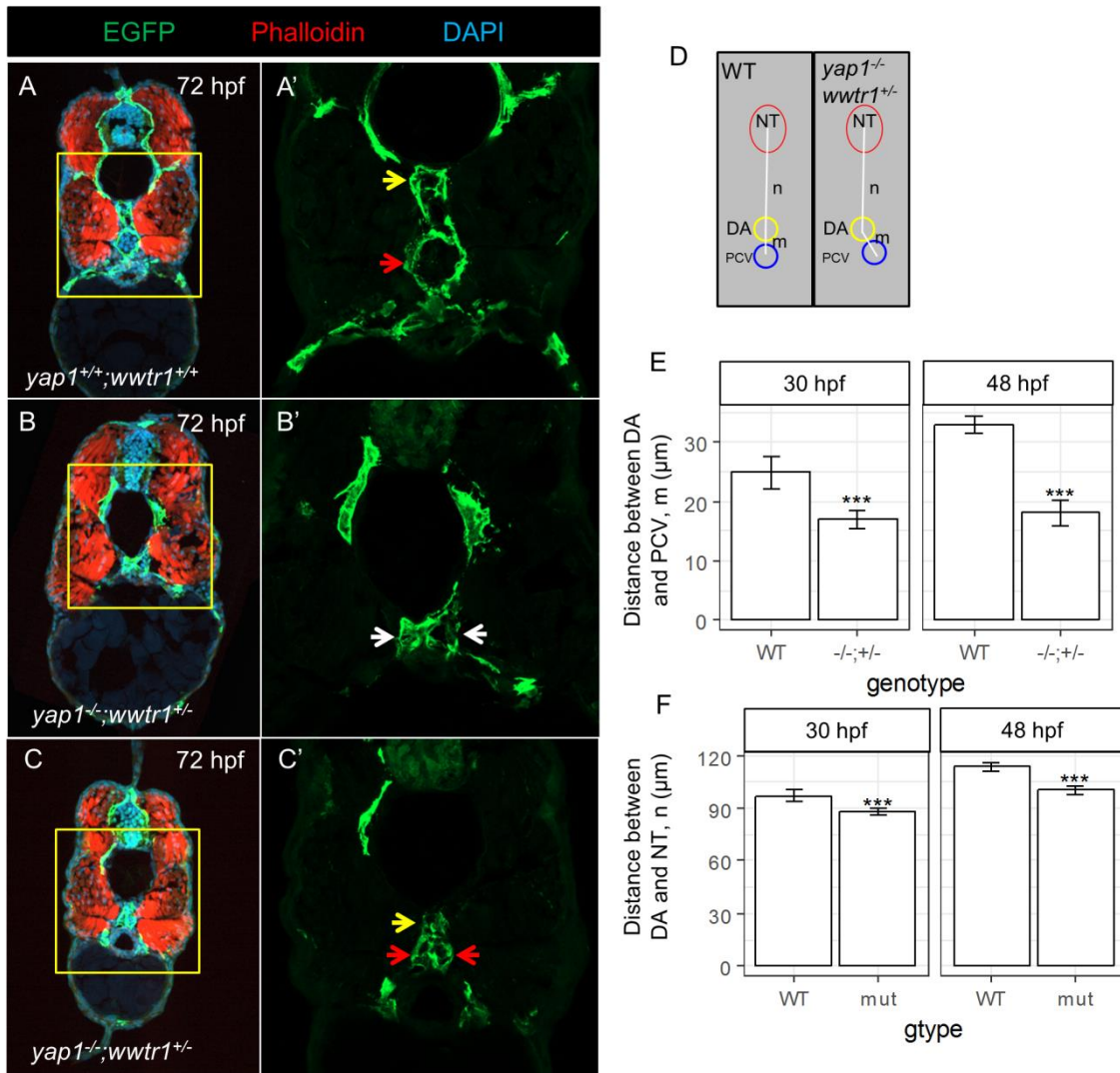
Figure 13. *yap1⁻/⁻;wwtr1⁺/⁻* **animals exhibit a shorter dorsoventral axis along the trunk.** (A-C) Confocal micrographs of cryosections from 72 hpf WT and *yap1⁻/⁻;wwtr1⁺/⁻* larvae trunks. EGFP signal is from the *etv2:*EGFP transgene. Yellow arrows point to the DA and red arrows, the PCV. White arrows point to DA/PCV. (D) Schematic of quantifying the length of the dorsoventral axis (NT to DA) and DA to PCV of zebrafish trunks. (E) Quantification of distance between DA and PCV. (F) Quantification of the length of the dorsoventral axis. *** - *P* < 0.001 by two-sample t-test. (A-C) will be used in a manuscript in preparation by Astone, et al. to be resubmitted to *Development*.
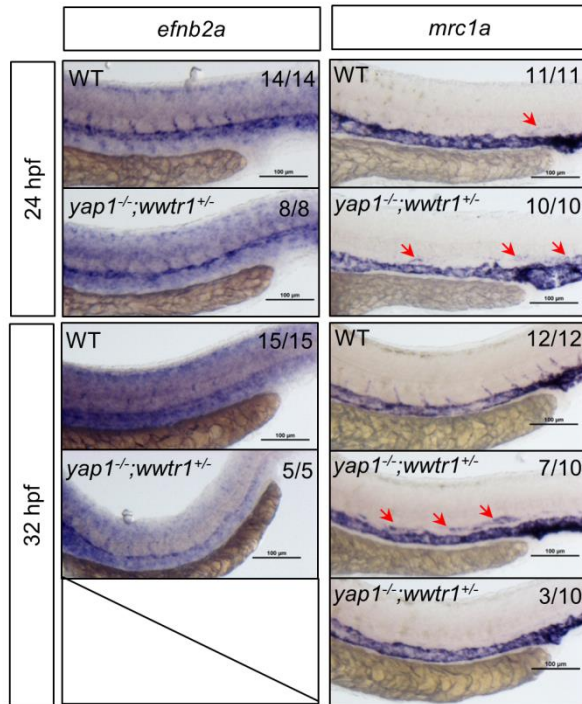
Figure 14. Expression pattern of an arterial and a venous marker in *yap1⁻ᐟ⁻;wwtr1⁺ᐟ⁻* trunks. Whole mount *in situ* hybridization (WISH) for *efnb2a* (an arterial marker) and *mrc1a* (a venous marker) expression in WT and *yap1⁻ᐟ⁻;wwtr1⁺ᐟ⁻* trunks at 24 and 32 hpf. Red arrows point to expression of *mrc1a* in the DA. This figure will be used in a manuscript in preparation by Astone, et al. to be resubmitted to *Development*.

Next, I characterized the development of angiogenic sprouts. By 30 hpf, I did not observe any overt perturbation to the patterning of the aISVs in *yap1$^{-/-}$;wwtr1$^{+/-}$* embryos (Figure 15A). Following primary angiogenic sprouting, a second wave of angiogenic sprouts (secondary sprouting) occur to give rise to the venous intersegmental vessels (vISVs) and parachordal lymphangioblasts (PLs) (Bussmann et al., 2010; Isogai et al., 2003; Yaniv et al., 2006). Here, I observed that *yap1$^{-/-}$;wwtr1$^{+/-}$* larvae showed fewer secondary sprouts, and is worsened by the absence of blood circulation (Figure 15B, C). However, as the absence of blood circulation could indicate poorer overall condition of these mutants, I decided to exclude them from future analyses. Taken together, Yap1/Wwtr1 could play a role in the emergence of the venous and lymphatic vascular network.

4.2.4.   Blood flow is required for venous intersegmental vessels (vISVs) sprouting

After excluding *yap1$^{-/-}$;wwtr1$^{+/-}$* larvae that lacked blood circulation, the remaining ones show weaker blood circulation. To elucidate whether blood circulation could influence the sprouting of vISVs and PLs, I used the *sih* morpholino to block cardiac contractility and blood circulation. The *sih* morphants, compared to control morphants (injected with a control morpholino), show markedly fewer vISVs, and to a lesser extent, fewer PLs (Figure 16A). In addition, *yap1$^{-/-}$;wwtr1$^{+/-}$* larvae similarly show fewer vISVs and PLs (Figure 16B). This observation indicates that blood flow and Yap1/Wwtr1 modulate secondary angiogenic sprouting.
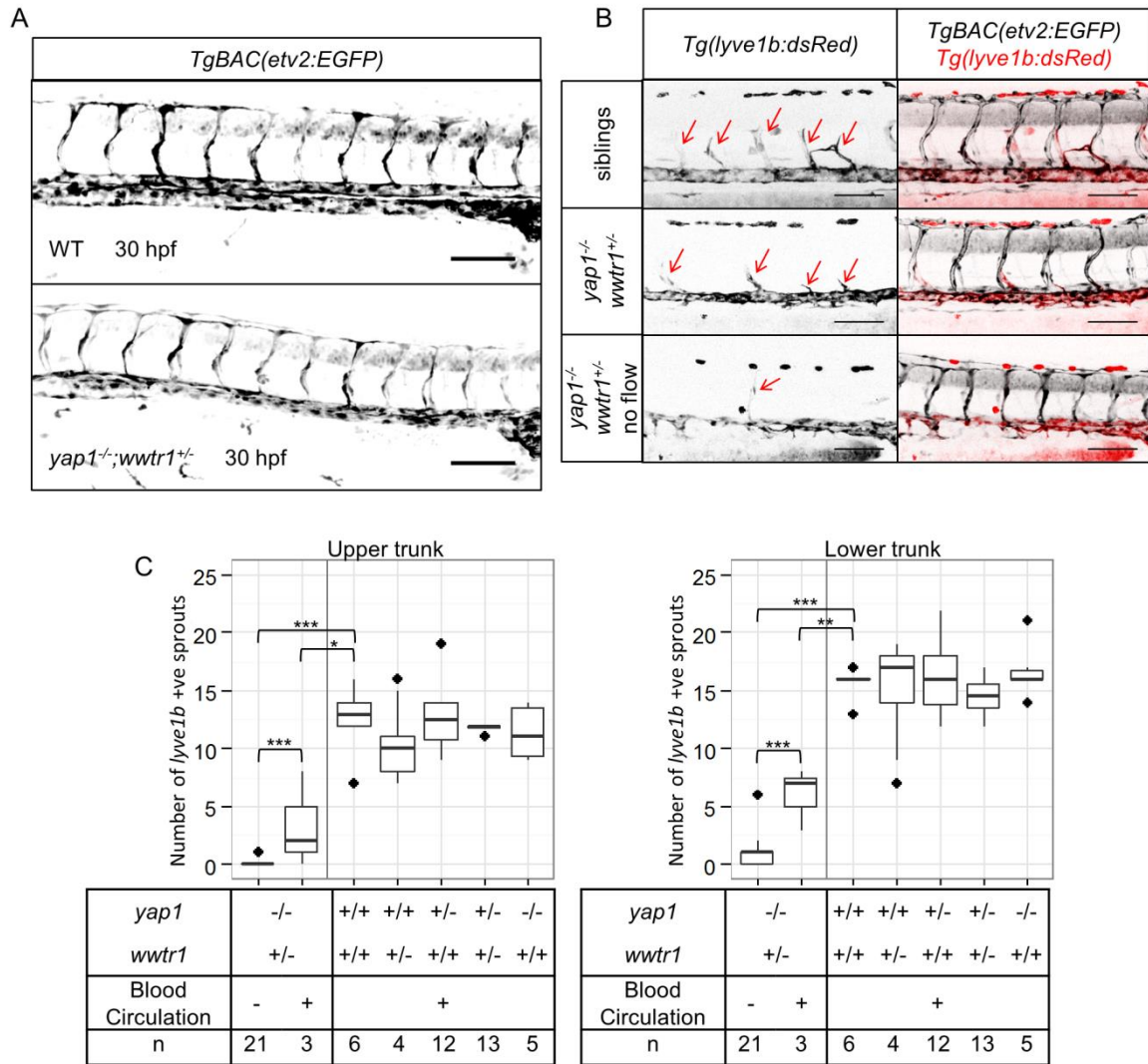
Figure 15. Trunk vascular phenotypes of *yap1^-/-;wwtr1^+/-* embryos. (A) Maximum intensity projections of 30 hpf WT and *yap1^-/-;wwtr1^+/-* trunks showing patterning of the primary segmental vessels. (B) Maximum intensity projections of 48 hpf WT and *yap1^-/-;wwtr1^+/-* trunks showing emergence of secondary sprouts marked by *lyve1b* reporter (red arrows). Most mutant embryos do not establish blood circulation by this stage due to severe cardiac phenotypes (see FIgure 12A) and resulted in a more severe reduction in the number of secondary sprouts. Scale bars, 100 μm. (C) Quantification of the number of secondary sprouts at 48 hpf in the upper trunk (spanning the yolk tube) and lower trunk (caudal to the yolk tube). * - $P < 0.05$; ** - $P < 0.01$; *** - $P < 0.001$ by Poisson regression.
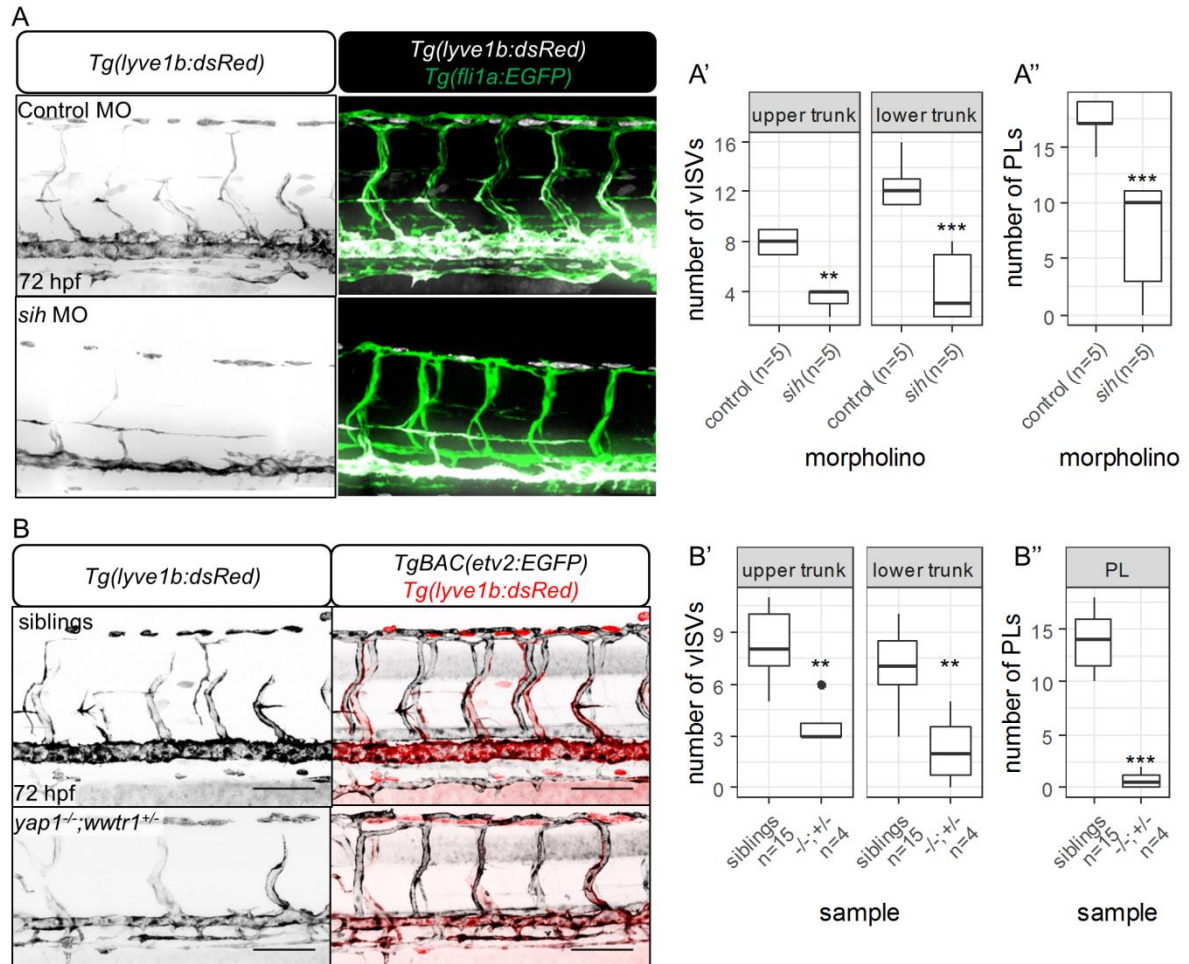
Figure 16. Number of vISVs and PLs in *sih* morphants and *yap1*^{-/-}*;wwtr1*^{+/-} larvae. (A) Maximum intensity projections of 72 hpf control and *sih* morphants' trunks. (A'-A'') Quantification of the number of vISVs (*lyve1b*[+] vessels connected to primary segmental vessels) and PLs (*lyve1b*[+] vessels on the horizontal myoseptum). (B) Maximum intensity projections of 72 hpf WT and *yap1*^{-/-}*;wwtr1*^{+/-} trunks. Mutants that do not establish blood circulation are discarded from analyses. (B'-B'') Quantification of the number of vISVs and PLs. Scale bars, 100 μm. ** - $P < 0.01$; *** - $P < 0.001$ by Poisson regression. Images from this figure will be used in a manuscript in preparation by Astone, et al. to be resubmitted to *Development*.

4.2.5. Yap1/Wwtr1 modulate the expression of *vegfc*, *cxcl12a* and *cyr61*

To further investigate the secondary sprouting phenotypes of *yap1$^{-/-}$;wwtr1$^{+/-}$* embryos, I assayed the expression of genes involved in this process, such as *vegfc*, *vegfr3*, *ccbe1*, *cxcl12a* and *cxcr4a* (Cha et al., 2012; Hogan et al., 2009a; Le Guen et al., 2014). Among these genes, I found that *vegfc* and *cxcl12a* were significantly downregulated in 36 hpf *yap1$^{-/-}$;wwtr1$^{+/-}$* trunks compared to WT siblings (Figure 17A). Furthermore, I observed the spatial distribution of *vegfc* expression in the DA is intermittent (Figure 17B). In addition, I assayed two canonical transcriptional targets of Yap1/Wwtr1, *cyr61* and *ctgfa*, and found that *cyr61* was also significantly downregulated (Figure 17C). In contrast, *sih* morphant trunks did not downregulate *vegfc* expression (Figure 17D). As recombinant CYR61 was shown to induce mouse embryonic fibroblasts (MEFs) to express *Vegfc* transcript (Mo et al., 2002), it is possible that Yap1/Wwtr1 controls the expression of *vegfc* through *cyr61*, which is expressed in the hypochord.

4.2.6. *vegfc$^{+/-}$* animals show severe reduction in the number of parachordal lymphangioblasts (PLs)

To functionally assess whether partial loss of *vegfc* could affect secondary sprouting, I counted the number of vISVs and PLs from 72 hpf *vegfc$^{+/-}$* and WT larvae. I found that while the number of vISVs were marginally fewer, the number of PLs was strongly affected compared to WT siblings (Figure 18). This observation suggests that partial loss of *vegfc* has impact on both vISVs and PLs, but PLs appear to be more sensitive.

4.2.7. Proposed model

Taken together, we show here that activity of Yap1/Wwtr1 in the endothelium can be modulated by blood flow. In addition, as Yap1 and Wwtr1 are expressed in the hypochord (Figure 9D), they could drive the expression of *cyr61*, and perhaps through Cyr61, modulates the expression of *vegfc*. The partial loss of Vegfc and Cxcl12a availability then lead to fewer vISVs and PLs in *yap1$^{-/-}$;wwtr1$^{+/-}$* larvae. Furthermore, I also postulate that blood flow, through modulation of Yap1/Wwtr1 activity in the endothelium, is required for vISV emergence (Figure 19).
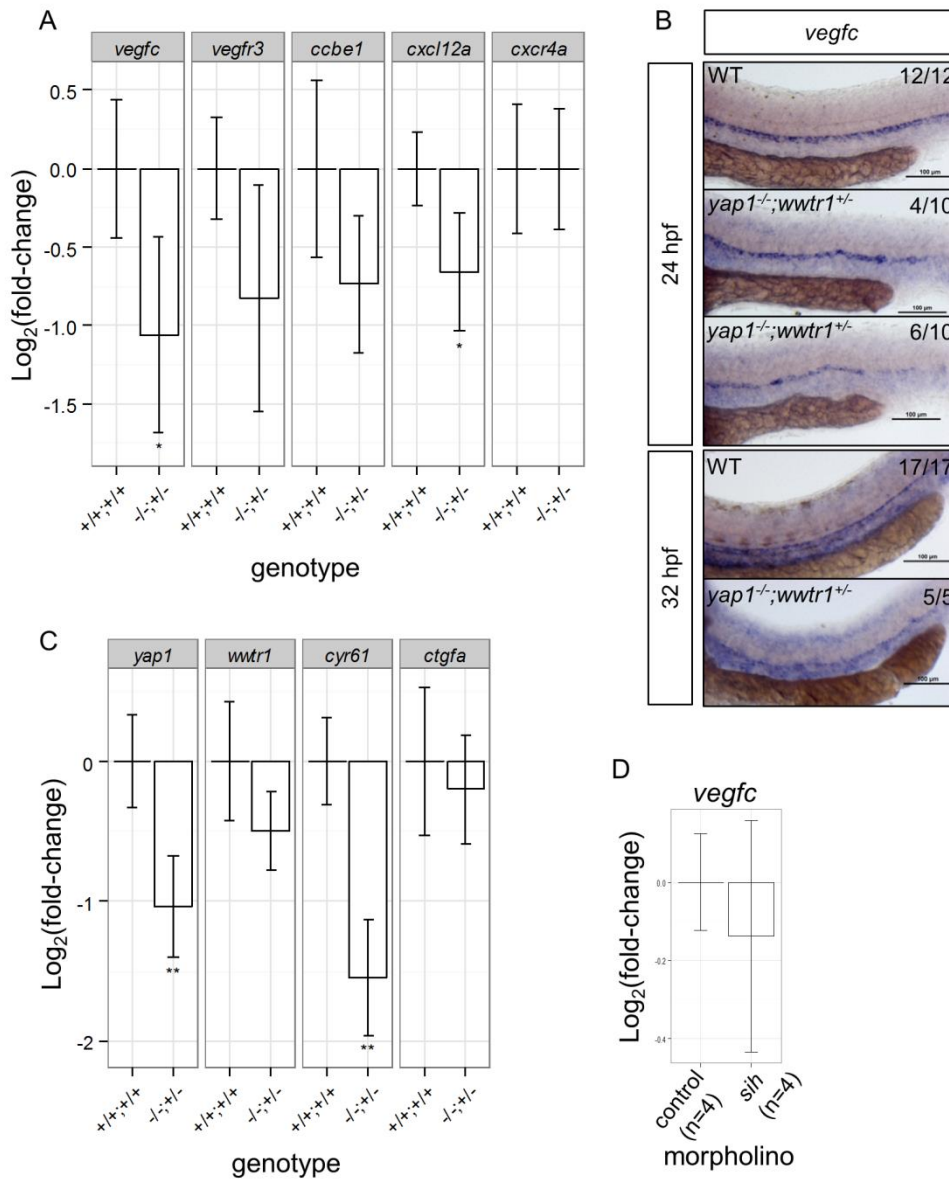
Figure 17. Expression of genes involved in modulating secondary sprouting. (A) Relative expression of genes involved in modulating secondary sprouting in 36 hpf WT and *yap1^-/-^;wwtr1^+/-^* trunks. (B) WISH for *vegfc* expression pattern in WT and *yap1^-/-^;wwtr1^+/-^* trunks. (C) Relative expression of *yap1/wwtr1* and canonical targets, *ctgfa* and *cyr61* in 36 hpf WT and *yap1^-/-^;wwtr1^+/-^* trunks. (D) Relative expression of *vegfc* in 36 hpf control and *sih* morphants trunk. * - $P < 0.05$; ** - $P < 0.01$ by two-sample t-test. Images from this figure will be used in a manuscript in preparation by Astone, et al. to be resubmitted to *Development*.
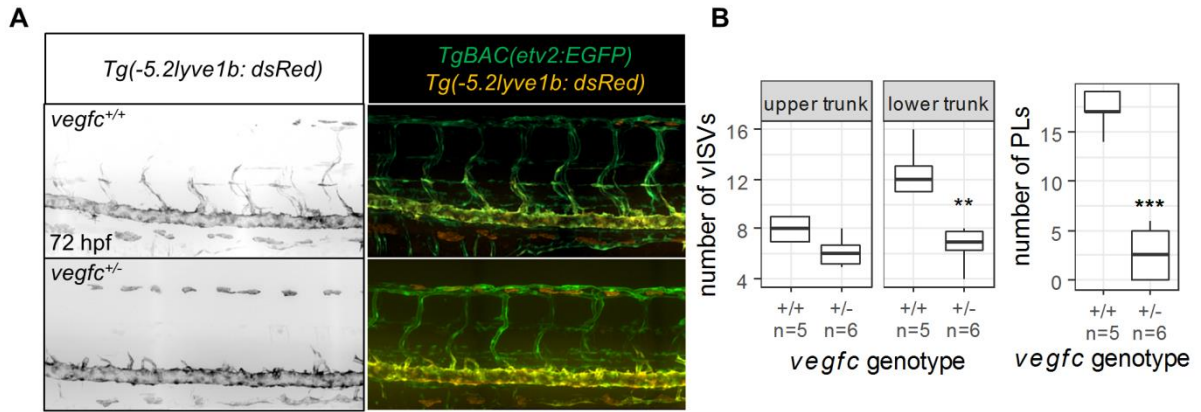
Figure 18. Number of vISVs and PLs in *vegfc*^{+/-} larvae. (A) Maximum intensity projections of 72 hpf WT and *vegfc*^{+/-} sibling larvae. (B) Quantification of the number of vISVs and PLs. ** - $P < 0.01$; *** - $P < 0.001$ by Poisson regression.
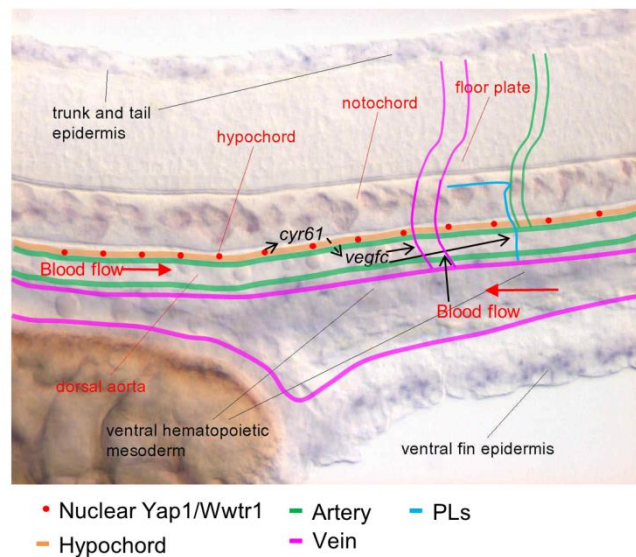
Figure 19. Proposed model of the modulation of secondary angiogenic sprouting by Yap1/Wwtr1 and blood flow. Blood flow regulates the activity of Yap1/Wwtr1 as revealed by the *Hsa.CTGF* reporter expression. When blood flow is absent, the number of vISVs are severely reduced, similar to the *yap1;wwtr1* mutants. *yap1;wwtr1* mutants show a more severe reduction in the number of PLs, concurrently with a reduced expression of *vegfc* and *cxcl12a*. Yap1/Wwtr1, which is expressed in the hypochord, modulates the expression of *cyr61* which is also expressed in the hypochord. Cyr61 may be secreted out to induce expression of *vegfc* in the DA. Image adapted from zfin.org

4.3. Roles for Yap1/Wwtr1 in heart development

4.3.1. *yap1$^{-/-}$* ventricles appear smaller and its wall is thinner

To elucidate the function of Yap1/Wwtr1 in heart development, I characterized the heart phenotypes in these mutants, beginning with *yap1$^{-/-}$* animals. At 78 and 96 hpf, I observed that the overall morphology of the *yap1$^{-/-}$* hearts appear normal, including formation of trabeculae (Figure 20A). Although the *yap1$^{-/-}$* ventricular chambers appear smaller at 78 hpf, the phenotype is not consistent and not evident at 96 hpf (quantification not shown). Homozygous mutants can survive to adulthood, but I did not formally quantify with a survival curve. The adult mutant hearts show variable sizes and morphology of the atrioventricular chambers (Figure 20B). With the help of Beate Grohmann who performed AFOG staining on the cryosections, the ventricular wall appears to be very thin, and trabecular structures are present (Figure 20C). These data are consistent with the phenotype of CKO *Yap1* mouse mutant, indicating that the primary role of YAP1 is in myocardial growth. Therefore, I focused my investigation to its vertebrate duplicate, Wwtr1 (Hilman and Gat, 2011).
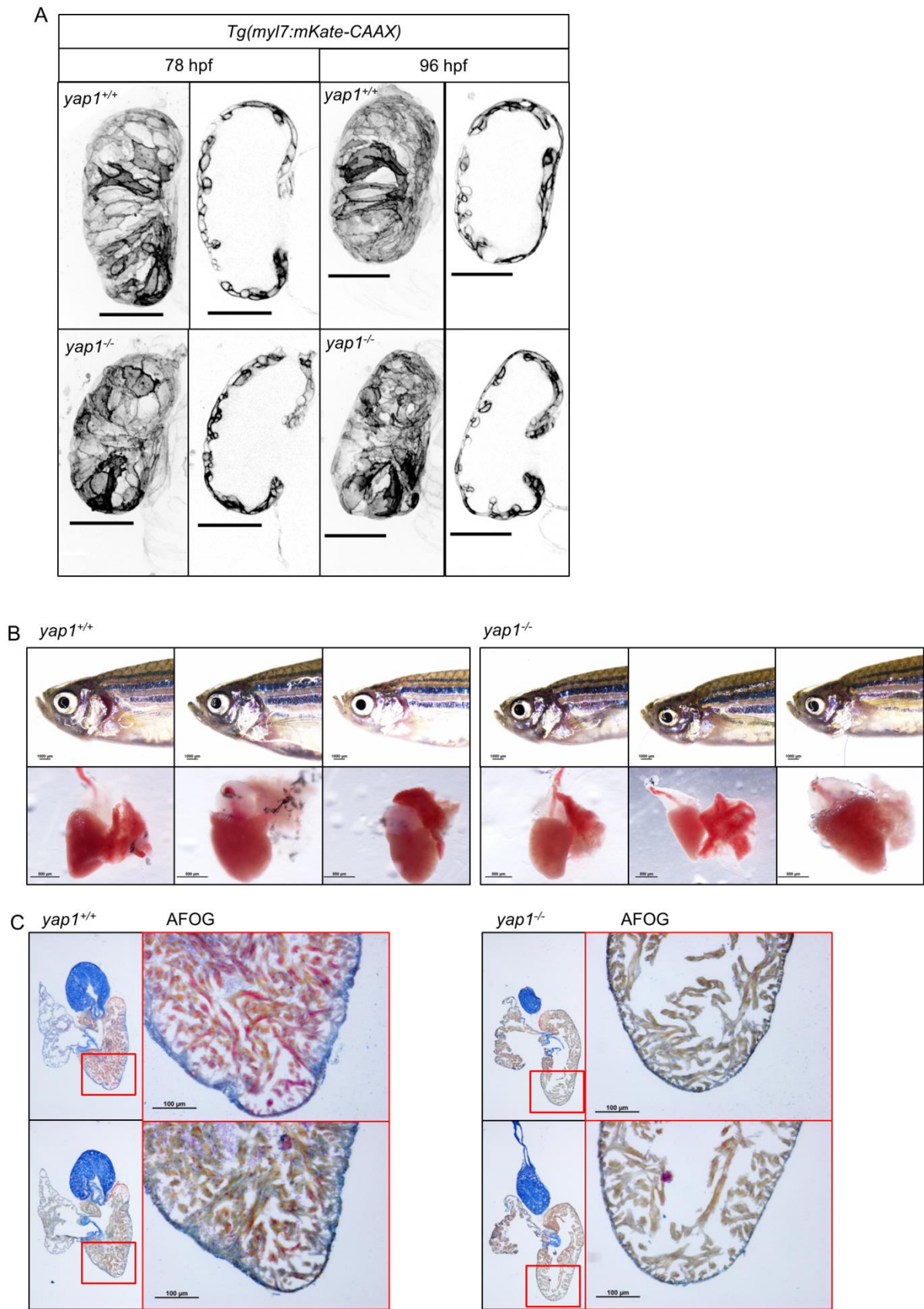
Figure 20. Myocardial growth phenotype of *yap1*^{-/-} animals. (A) Maximum intensity projections and sagittal sections of WT and *yap1*^{-/-} larvae hearts. Scale bars, 50 µm. (B)

Stereomicrographs of adult WT and *yap1*^{-/-} animals and the corresponding isolated hearts. Ventricle to the left, atrium to the right. (C) Cryosections of adult hearts (2 WT and mutant hearts each) stained with AFOG protocol. High magnification images correspond to the demarcated red boxes.

4.3.2. Expression of Wwtr1 in the developing heart

In the developing zebrafish heart, Wwtr1 is predominantly localized to the nuclei of ventricular cardiomyocytes (Figure 21). Some of the punctate immunostaining signal in the cytoplasm are non-specific (Figure 22A). Wwtr1 is also expressed in the epicardium, but not evidently in the endocardium. The Wwtr1 immunostaining intensity from one cardiomyocyte to another is also variable. Firstly, in the compact wall, I observed a mild correlation between cardiomyocyte apical surface area and perimeter to Wwtr1 immunostaining intensity (Figure 22B). I tested other parameters such as circularity and aspect ratio but did not yield any obvious correlations. Additionally, I found that Wwtr1 immunostaining is fainter in the nuclei of trabecular cardiomyocytes than that of the compact wall cardiomyocytes (Figures 21 and 22C). Taken together, Wwtr1 is localized to the nuclei of cardiomyocytes but is variably regulated from one cell to another.

4.3.3. *wwtr1*^{-/-} hearts lacked trabecular ridges

I then investigated the function of Wwtr1 in heart development by analyzing the hearts of *wwtr1* mutants. Interestingly, I found that the *wwtr1* mutants have a trabeculation phenotype. Specifically, trabecular ridges can be observed lining the ventricular wall in 96 hpf WT zebrafish hearts but not *wwtr1*^{-/-} hearts (Figure 23A, B). Although the morphology of the luminal wall of *wwtr1*^{-/-} hearts is reminiscent of the *erbb2*^{-/-} hearts, there are distinctive differences. Firstly, the *wwtr1*^{-/-} cardiac wall is composed of multi layered cardiomyocytes unlike the *erbb2*^{-/-} hearts which are single layered (Liu et al., 2010). Although multi layered, there are fewer cardiomyocytes in the trabecular layer of *wwtr1*^{-/-} hearts (Figure 23C). Secondly, I did not observe fewer cardiomyocytes undergoing apical constriction (Figure 24A, B), as is observed in previously described trabeculae-null hearts, such as embryos treated with Erbb2 inhibitor and *nrg2a*^{-/-} hearts (Jiménez-Amilburu et al., 2016). Finally, I investigated the morphology of *wwtr1*^{-/-} cardiomyocytes in the trabecular layer and found that not only they appear flat instead of tubular, they do not exhibit any organized sarcomeric actin (Figure 24C).
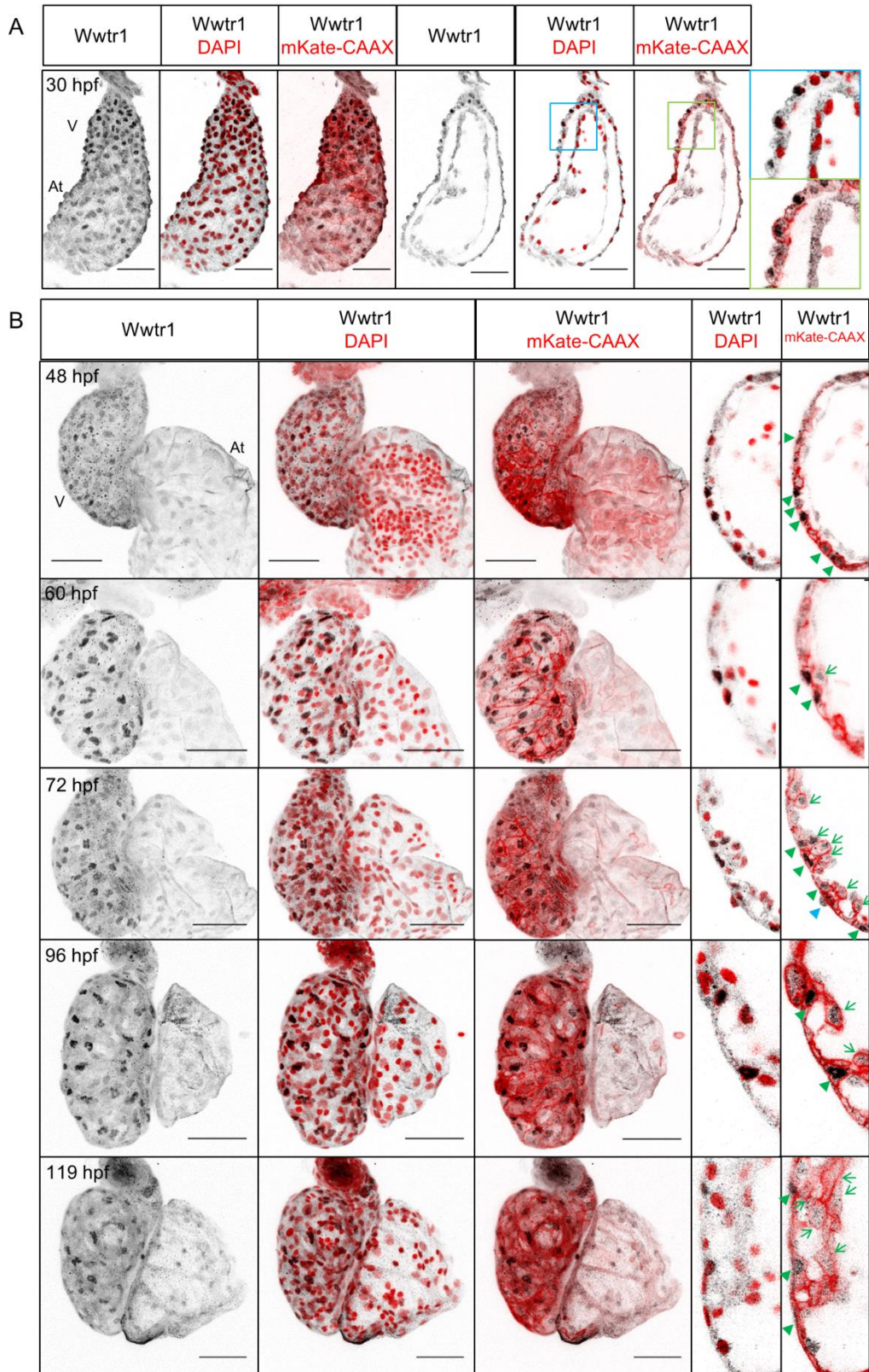
Figure 21. Expression and localization of Wwtr1 in the developing zebrafish heart. (A) Maximum intensity projection and sagittal section of a whole mount zebrafish heart at 30 hpf. Inset images (blue and lime green squares) clearly show that the nuclei of cardiomyocytes (membranes marked by mKate-CAAX) but not of endocardial cells are positive for Wwtr1 expression. (B) Maximum intensity projections and sagittal sections of whole mount zebrafish hearts at 48 to 119 hpf. Wwtr1 is predominantly nuclear-localized in some ventricular cardiomyocytes (green arrowheads) and moderately expressed in epicardial cells (blue arrowhead), but absent from endocardial cells. During trabeculation, some cardiomyocytes delaminate from the compact wall and exhibit weaker nuclear expression of Wwtr1 compared to adjacent compact cardiomyocytes (green arrows and Figure 22B). Nuclei are counterstained with DAPI and cardiomyocyte membranes are marked by the expression of *myl7:*mKate-CAAX. Scale bars, 50 μm. V – Ventricle; At – Atrium. 30 - 72 hpf: n > 3; 96 and 119 hpf: n = 2. This figure has been used in a manuscript by Lai et al. submitted to *Development*.
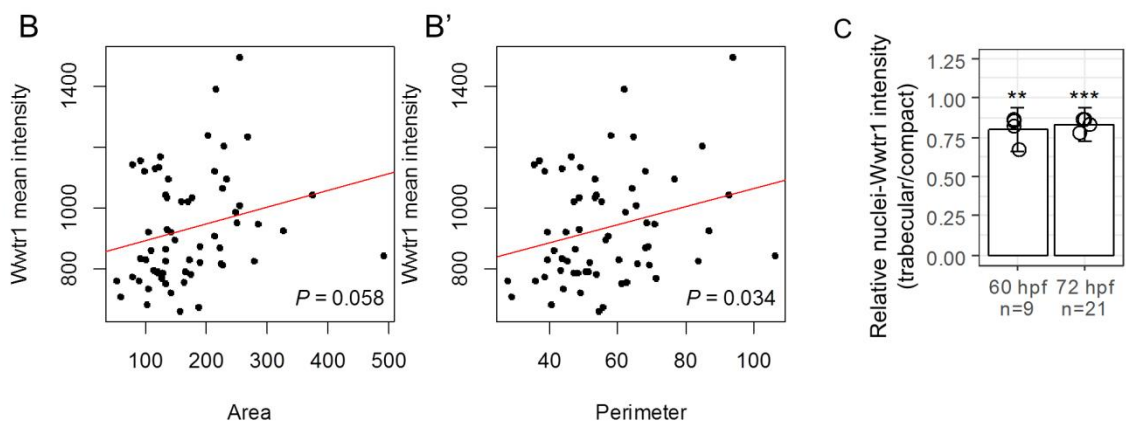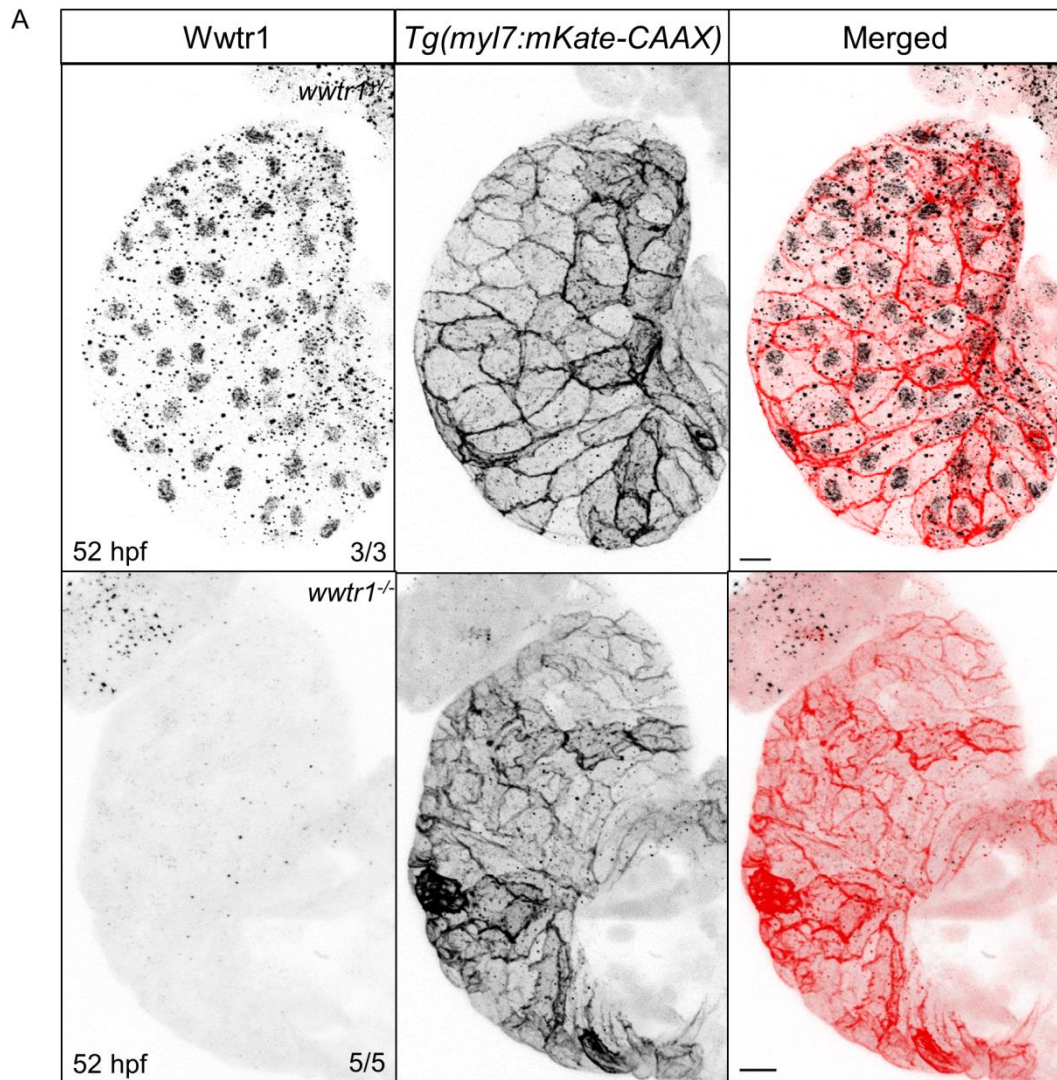
A

Wwtr1	*Tg(myl7:mKate-CAAX)*	Merged

wwtr1⁺/⁺ 52 hpf 3/3

wwtr1⁻/⁻ 52 hpf 5/5

B

Wwtr1 mean intensity vs Area, *P* = 0.058

B'

Wwtr1 mean intensity vs Perimeter, *P* = 0.034

C

Relative nuclei-Wwtr1 intensity (trabecular/compact)

60 hpf n=9 **

72 hpf n=21 ***

Figure 22. Antibody against human YAP1 and WWTR1 is specific for zebrafish Wwtr1. (A) Maximum intensity projections of cardiac ventricles stained for Wwtr1. Punctae observed in *wwtr1⁻ᐟ⁻* samples are non-specific signal. Scale bars, 10 μm. Correlation of nuclear Wwtr1 immunostaining intensity to cardiomyocyte apical surface area (B) and perimeter (B'). *P*-values calculated by Pearson correlation. (C) Quantification of Wwtr1 staining intensity in the nuclei of trabecular cardiomyocytes relative to nuclei of adjacent compact cardiomyocytes at 60 and 72 hpf. 'n' number of trabecular cardiomyocyte nuclei were assayed from 4 hearts at each time point. Error bars are one unit of standard deviation. ** - $P < 0.01$; *** - $P < 0.001$ by two-sample t-test. This figure has been used in a manuscript by Lai et al. submitted to *Development*.
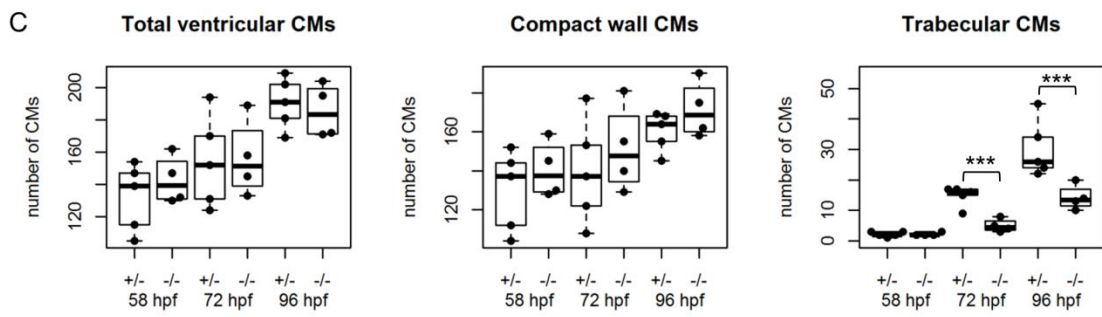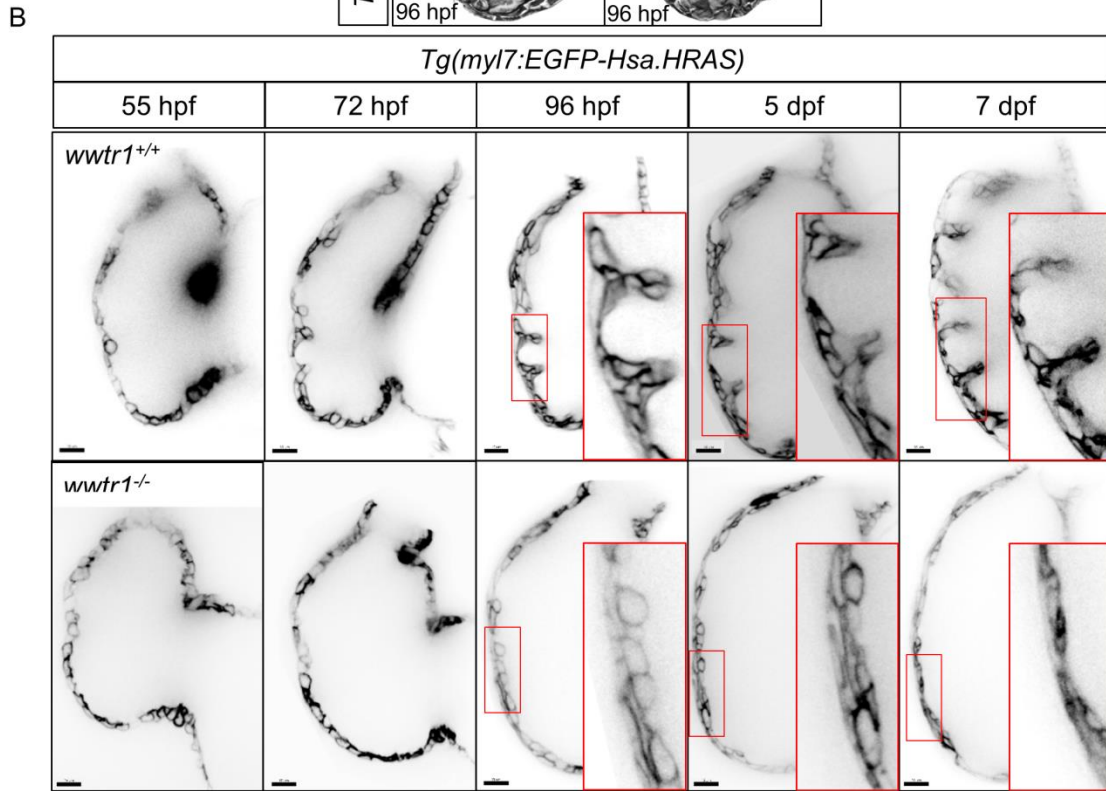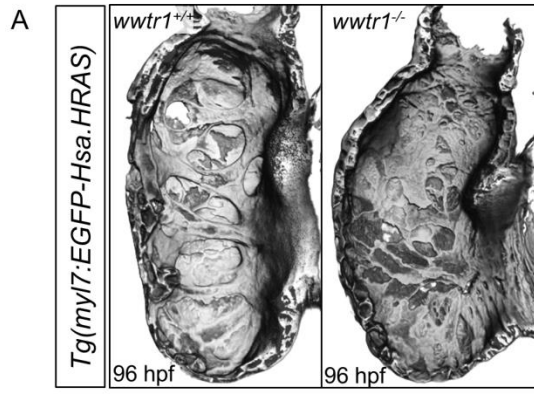
Figure 23. *wwtr1* mutant hearts do not develop trabecular ridges. (A) 3D surface reconstruction of ventricular chambers at 96 hpf shows distinct muscular ridges in *wwtr1$^{+/+}$* (8/8) and *wwtr1$^{+/-}$* (7/7), but not *wwtr1$^{-/-}$* (11/13) hearts. (B) Confocal sagittal sections of WT and *wwtr1$^{-/-}$* ventricular chambers of the same animal from 55 hpf to 7 dpf. Scale bars, 15 μm. (C) Longitudinal quantification of the number of ventricular cardiomyocytes (CMs) from 5 *wwtr1$^{+/-}$* and 4 *wwtr1$^{-/-}$* hearts. The total number of ventricular CMs is divided into two groups: 'compact wall CMs' and 'trabecular CMs'. Each point represents a heart. *** - $P < 0.001$ by Poisson regression. This figure has been used in a manuscript by Lai et al. submitted to *Development*.
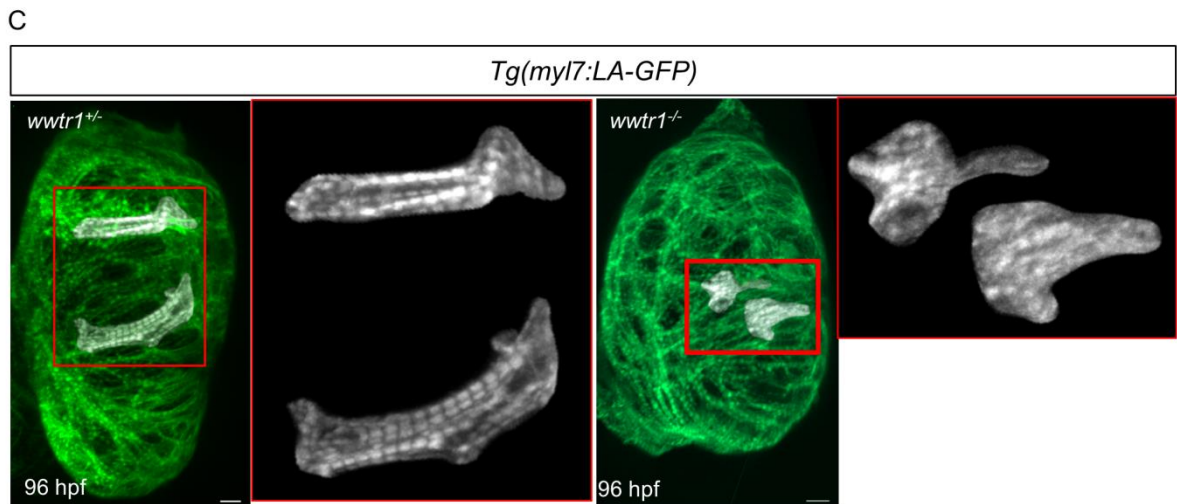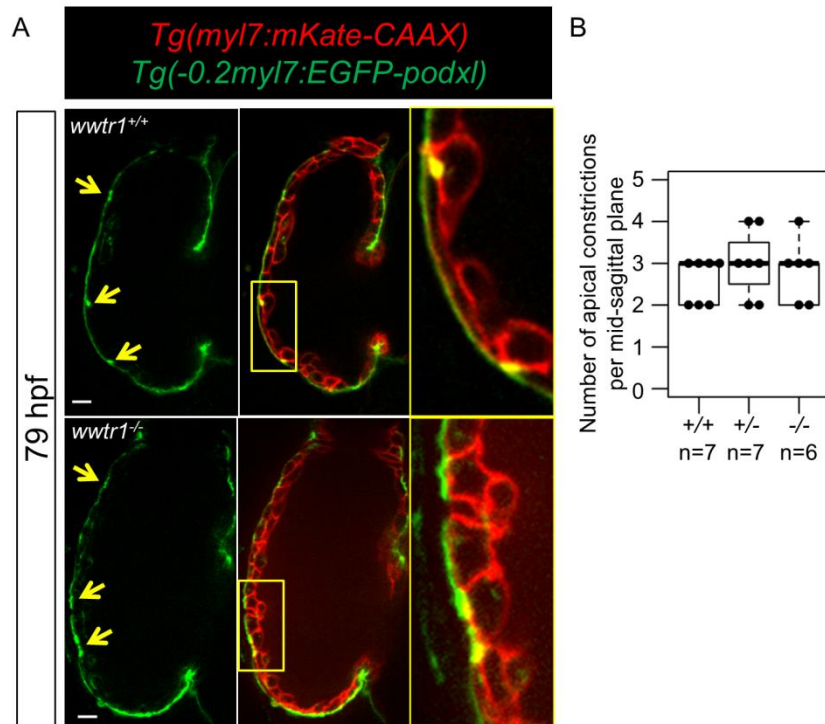
Figure 24. Number of cardiomyocytes undergoing apical constriction and morphology of trabecular cardiomyocytes. (A) Mid-sagittal sections of 79 hpf hearts showing cardiomyocytes undergoing apical constriction (yellow arrows). Scale bars, 10 μm. (B) Number of cardiomyocytes undergoing apical constriction. Each point represents a heart. (C) Maximum projections of 96 hpf hearts. Clusters of cardiomyocytes in the trabecular layer (*myl7:*mKate$^+$) were selected to extract the GFP channel (shown in insets). 3/3 of *wwtr1$^{+/+}$* or *wwtr1$^{+/-}$* trabecular cardiomyocytes from 2 hearts have tubular morphology and striated cortical actin and 4/4 of *wwtr1$^{-/-}$* trabecular cardiomyocytes from 2 hearts have flattened morphology and indistinct cortical actin. Scale bars, 10 μm. This figure has been used in a manuscript by Lai et al. submitted to *Development*.

90

4.3.4. Wwtr1 mediates myocardial Notch signaling by its Tead-binding domain in a cell-autonomous manner

As manipulating Notch signaling in the developing heart can affect trabeculation (D'Amato et al., 2016; Grego-Bessa et al., 2007; Han et al., 2016), I used a *tp1* reporter which expresses the destabilized Venus when Notch signaling is active (Ninov et al., 2012). The endocardium of WT and *wwtr1*^{-/-} hearts invariably express the *tp1* Notch reporter at 48 hpf (Figure 25A). However, at 72 and 96 hpf, while all WT and *wwtr1*^{+/-} hearts have some cardiomyocytes expressing the *tp1* Notch reporter, most *wwtr1*^{-/-} hearts do not (Figure 25A, B). Interestingly, when I mosaically expressed *myl7:*mKate-2A-Wwtr1 in *wwtr1*^{-/-} hearts, it is able to cause some cardiomyocytes in *wwtr1*^{-/-} hearts to express the *tp1* Notch reporter (Figure 26). I then constructed variants of Wwtr1 affecting the WW domain (WW*: W142A, P145A) (Linn et al., 1997) and the Tead-Binding Domain (TBD*: S48A; ΔTBD: P46_D65del) (Miesfeld et al., 2015; Vassilev et al., 2001; Zhao et al., 2008). Whereas mosaic expression of WW* variant could result in some cardiomyocytes in *wwtr1*^{-/-} hearts to express the *tp1* Notch reporter, the TBD* and ΔTBD variants could not (Figure 26). These data indicate that the Tead-Binding Domain (TBD) of Wwtr1 is indispensable for cardiomyocytes to express the *tp1* Notch reporter.

With the help of Hans-Martin Maischein, we performed transplantation studies to understand whether Wwtr1 has a cell-autonomous function on the *tp1* Notch reporter. When WT cells were transplanted into *wwtr1*^{+/-} or *wwtr1*^{-/-} hosts, both WT and *wwtr1*^{+/-} cardiomyocytes could express the *tp1* Notch reporter, but not *wwtr1*^{-/-} cardiomyocytes (Figure 27A). Conversely, when *wwtr1*^{+/-} or *wwtr1*^{-/-} cells were transplanted into WT hosts, again both WT and *wwtr1*^{+/-} cardiomyocytes could express the *tp1* Notch reporter, but not *wwtr1*^{-/-} cardiomyocytes (Figure 27B). However, a given WT/*wwtr1*^{+/-} mosaic heart may contain *tp1*[+] exclusively in WT or heterozygous cardiomyocytes, as this is largely because not all compact wall cardiomyocytes will express this reporter. This transplantation experiment shows that Wwtr1 functions in a cell-autonomous manner in cardiomyocytes to express the *tp1* Notch reporter.
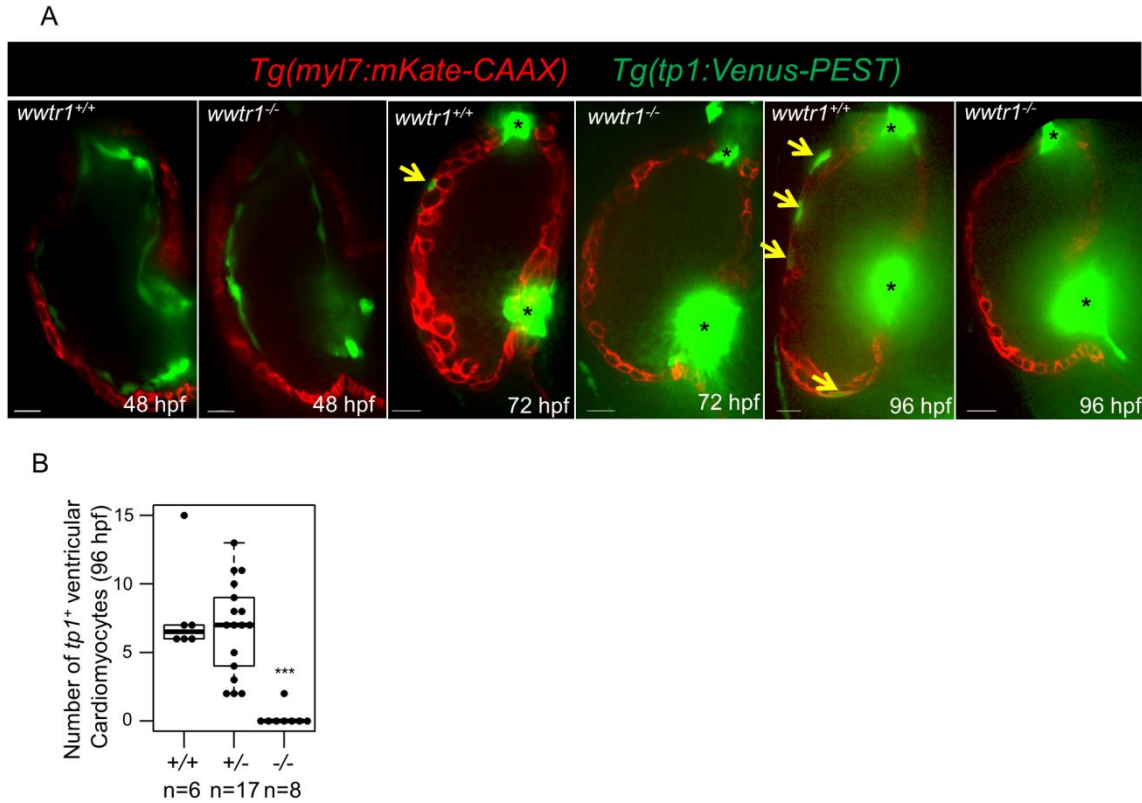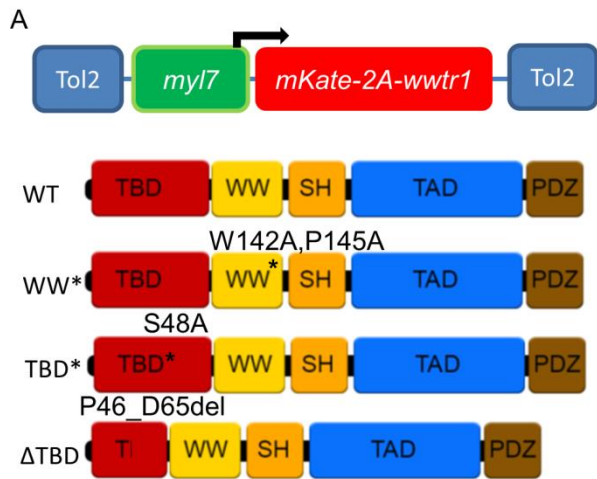
Figure 25. Cardiomyocytes in *wwtr1* mutants fail to express the *tp1* Notch reporter. (A) Representative sagittal sections of ventricular chambers at 48, 72 and 96 hpf. Yellow arrows point to cardiomyocytes expressing the *tp1* Notch reporter. The out of focus green signal is from endocardial cells at the valve regions (black asterisks). Scale bars, 15 μm. (B) Number of *tp1*[+] ventricular cardiomyocytes at 96 hpf. Each point represents a heart. *** - $P < 0.001$ by Poisson regression. This figure has been used in a manuscript by Lai et al. submitted to *Development*.

(This page has been intentionally left blank)

A

Tol2 | myl7 | mKate-2A-wwtr1 | Tol2

WT — TBD | WW | SH | TAD | PDZ

W142A,P145A
WW* — TBD | WW* | SH | TAD | PDZ

S48A
TBD* — TBD* | WW | SH | TAD | PDZ

P46_D65del
ΔTBD — TI | WW | SH | TAD | PDZ

B

```
Human YAP1   195-QTTTWQDPRK-204
Mouse YAP1   180-QTTTWQDPRK-189
Zfish Yap1   150-QTTTWQDPRK-149
Zfish Wwtr1  138-KITTWHDPRK-147
Wwtr1 WW*    138-KITTAHDARK-147

Human YAP1   90-KLPDSFFKPP-99
Mouse YAP1   75-KLPDSFFKPP-84
Zfish Yap1   50-KLPDSFFTPP-59
Zfish Wwtr1  44-DMPQSFFQEP-53
Wwtr1 TBD*   44-DMPQAFFQEP-53

Human YAP1   89-RKLPDSFFKPPEPKSHSRQASTDAGT-114
Mouse YAP1   74-RKLPDSFFKPPEPKSHSRQASTDAGT-99
Zfish Yap1   49-RKLPDSFFTPPEPKSHSRQASTDAGT-74
Zfish Wwtr1  43-KDMPQSFFQEPDSGSHSRQSSADSGS-68
Wwtr1 ΔTBD   43-KDM--------------------SGS-48
```

C

Number of $tp1^+$ and $tp1^-$ hearts

number of $wwtr1^{-/-}$ hearts (y-axis, 0 to 8)

Legend: $tp1^+$ (blue), $tp1^-$ (red)

Injected construct (x-axis): WT, WW*, TBD*, ΔTBD

D

Tg(tp1:Venus-PEST)
pTol2-myl7:mKate-2A-wwtr1

$wwtr1^{-/-}$
79 hpf

Tg(tp1:Venus-PEST)
pTol2-myl7:mKate-2A-wwtr1_WW*

$wwtr1^{-/-}$
80 hpf

Tg(tp1:Venus-PEST)
pTol2-myl7:mKate-2A-wwtr1_TBD*

$wwtr1^{-/-}$
80 hpf

Tg(tp1:Venus-PEST)
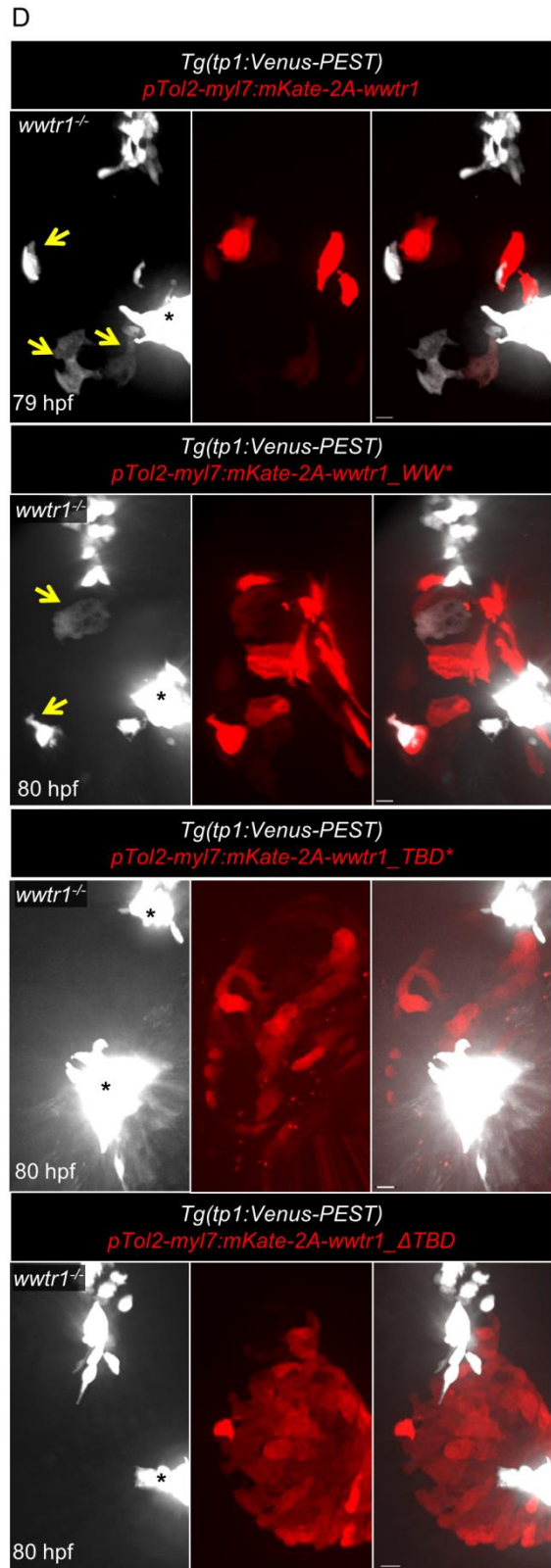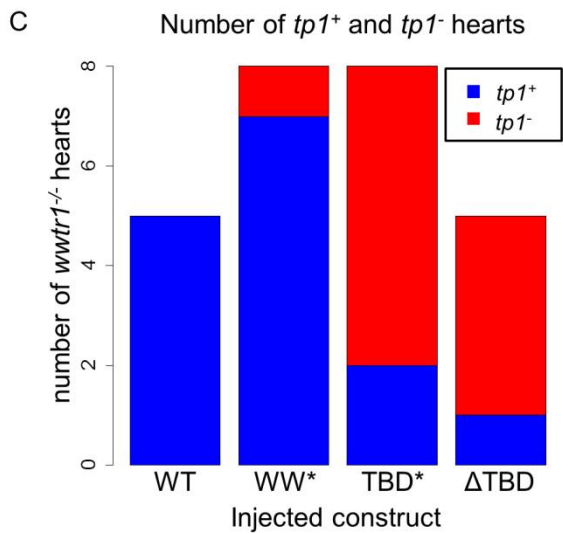*pTol2-myl7:mKate-2A-wwtr1_ΔTBD*

$wwtr1^{-/-}$
80 hpf

Figure 26. The Tead-binding domain of Wwtr1 is required for cardiomyocyte expression of the *tp1* Notch reporter. (A) Schematic of tol2 plasmid constructs to express mKate and Wwtr1, connected by a self-cleavable 2A peptide, under the *myl7* promoter. WT *wwtr1* was substituted with different variants in the WW domain (WW*: W142A, P145A) and Tead-binding domain (TBD*: S48A; ΔTBD: P46_D65del). (B) Sequence alignments of zebrafish (Zfish) Yap1/Wwtr1 to human and mouse YAP1 corresponding to the WW domain and Tead-Binding domain (TBD). Underlined amino acid residues were changed to generate the mutant proteins shown in (A). (C) Quantification of $tp1^+$ and $tp1^-$ $wwtr1^{-/-}$ hearts after injection with the constructs shown on the x-axis. $tp1^+$ hearts show at least one $tp1^+$ cardiomyocyte. (D) Representative maximum intensity projections of $wwtr1^{-/-}$ hearts after injection with the constructs shown in (A). Yellow arrows point to $tp1^+$ cardiomyocytes. The out of focus white signal is from endocardial cells at the valve regions (black asterisks). Scale bars, 10 μm. This figure has been used in a manuscript by Lai et al. submitted to *Development*.
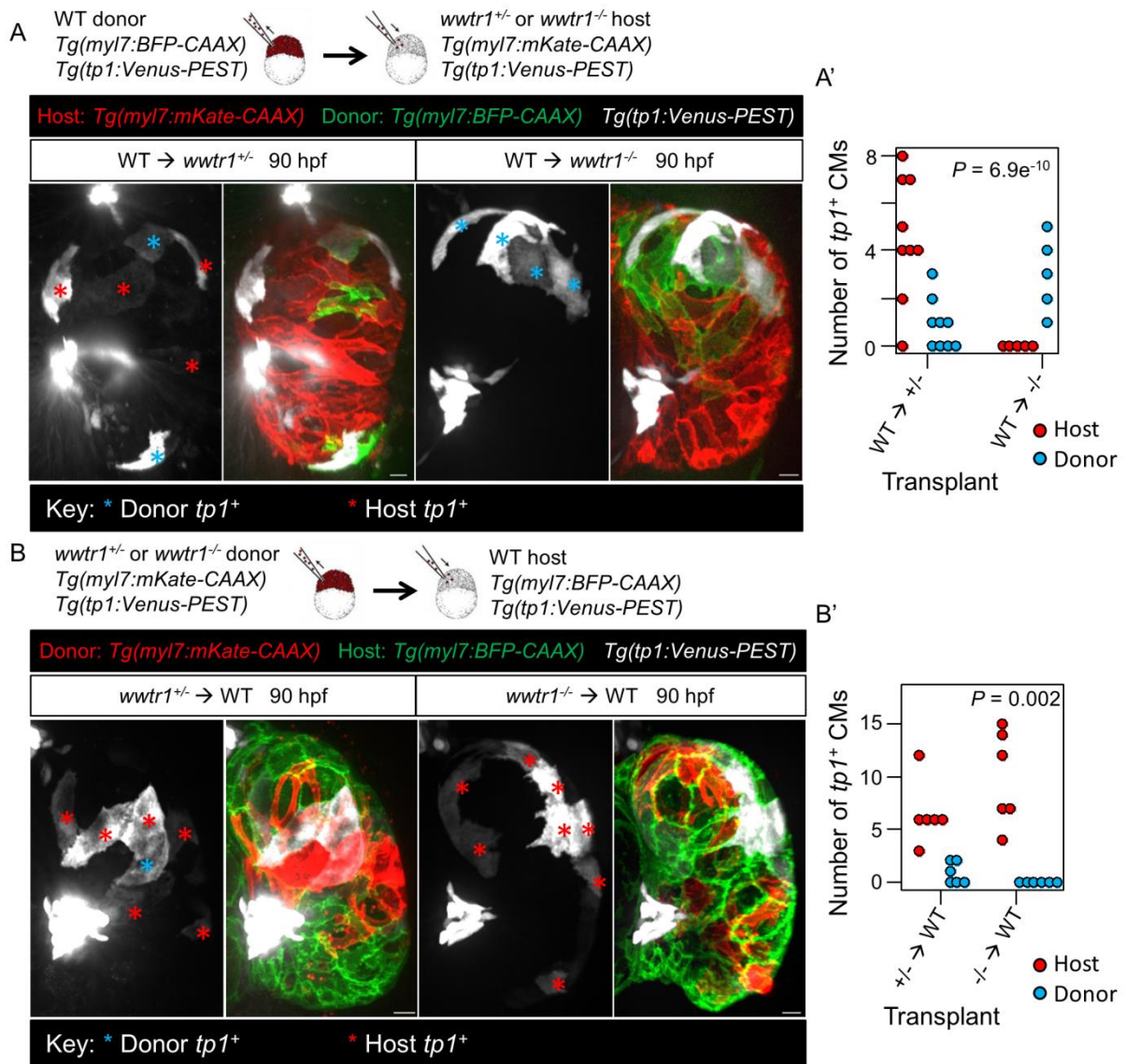
Figure 27. Wwtr1 functions cell-autonomously in cardiomyocytes for *tp1* Notch reporter expression. Maximum intensity projections of hearts derived from transplanting WT cells into *wwtr1*^{+/-} or *wwtr1*^{-/-} hosts (A), and *vice versa* (B). Scale bars, 10 μm. (A', B') Number of *tp1*[+] donor and host cardiomyocytes (CMs) according to the respective transplantation schemes as indicated on the x-axis. *P*-values were calculated by exact Binomial test. This figure has been used in a manuscript by Lai et al. submitted to *Development*.

4.3.5. Preference for *wwtr1*^{-/-} cardiomyocytes to populate the trabecular layer of WT hearts

Surprisingly, in the above mentioned transplant experiments, I observed that *wwtr1*^{-/-} cardiomyocytes were able to contribute to the trabecular layer of WT hosts. In fact, I found in these mosaic animals that *wwtr1*^{-/-} cardiomyocytes were located more frequently than *wwtr1*^{+/-} cardiomyocytes in the trabecular layer of WT hearts (Figure 28A). In the controls (i.e. *wwtr1*^{+/-} → WT), we observed that ~60% of cardiomyocytes are located in the trabecular layer, a similar proportion that was reported previously (Liu et al., 2010). Conversely, in *wwtr1*^{-/-} hearts, WT cardiomyocytes contributed about ~25% cardiomyocytes in the trabecular layer (Figure 28B). These data suggest that Wwtr1 could modulate trabeculation. Consistent with this idea, the Wwtr1 immunostaining in nuclei of trabecular cardiomyocytes are reduced than that of the compact wall cardiomyocytes (Figure 22C). I thus complemented these findings by performing a gain-of-function experiment. The constitutively active Wwtr1 (CAWwtr1) is generated by a S79A substitution, which is homologous to the constitutively active Yap1 (S89A) protein. I mosaically expressed *myl7*:mKate (control) and *myl7*:mKate-2A-CAWwtr1 in WT hearts and found that cardiomyocytes expressing mKate-2A-CAWwtr1 were more likely to be in the compact layer than the controls (Figure 28C). These observations support the idea that Wwtr1 can modulate a cardiomyocyte's decision to enter the trabecular layer.

4.3.6. WT trabecular cardiomyocytes in *wwtr1*^{-/-} hearts show abnormal morphology

From the transplant experiments, I not only observed that there are fewer WT cardiomyocytes in the trabecular layer of *wwtr1*^{-/-} hearts, but also that the morphology of these cardiomyocytes is reminiscent of the morphology of cardiomyocytes in the trabecular layer of *wwtr1*^{-/-} hearts. Some of these trabecular cardiomyocytes make "fork-like" extensions that are in contact with the compact wall cardiomyocytes. WT trabecular cardiomyocytes in *wwtr1*^{+/-} hearts make extensions that are ~30 μm long, but in *wwtr1*^{-/-} hearts they are ~ 12 μm long. *wwtr1*^{-/-} trabecular cardiomyocytes in WT hearts make extensions that are ~ 20 μm long (Figure 29). These transplantation data are in discordance with the reduced trabeculation phenotype of *wwtr1*^{-/-} hearts, perhaps indicating that prior to trabeculation, the development of the *wwtr1*^{-/-} compact wall is affected and unable to support trabeculation.

97

A Host CM: *Tg(myl7:BFP-CAAX)*
Donor CM: *Tg(myl7:mKate-CAAX)*

| *wwtr1⁺/⁻* → WT | *wwtr1⁻/⁻* → WT |

90 hpf

A' WT host

Donor Cardiomyocytes
- trabecular
- compact

Donor Genotype
+/− n=8   −/− n=13

B Host CM: *Tg(myl7:mKate-CAAX)*
Donor CM: *Tg(myl7:BFP-CAAX)*

| WT → *wwtr1⁺/⁻* | WT → *wwtr1⁻/⁻* |

90 hpf

B' WT donor

Donor Cardiomyocytes
- trabecular
- compact

Host Genotype
+/− n=6   −/− n=5

C CAWwtr1

S79A
TBD — WW — SH — TAD — PDZ

Yap1: 80-PHHVRAHSSPA-90
Wwtr1: 72-RVHFRSRSSPA-82
HXRXXS motif: HXRXXS

C' *Tg(myl7:EGFP-Hsa.HRAS)*

| *pTol2-myl7:mKate* | *pTol2-myl7:mKate-2A-CAWwtr1* |

96 hpf

C"
- trabecular
- compact

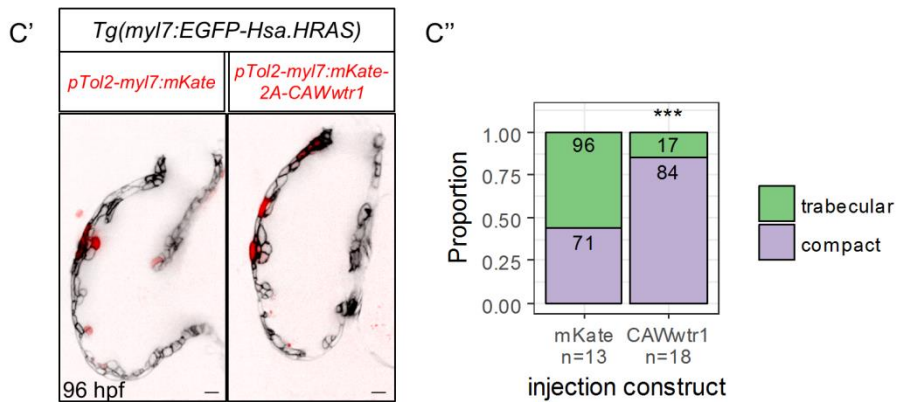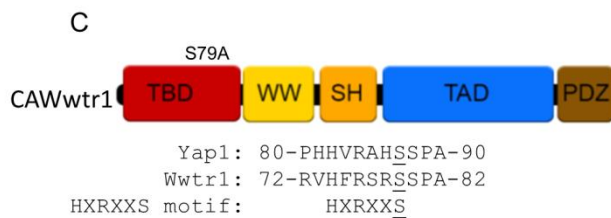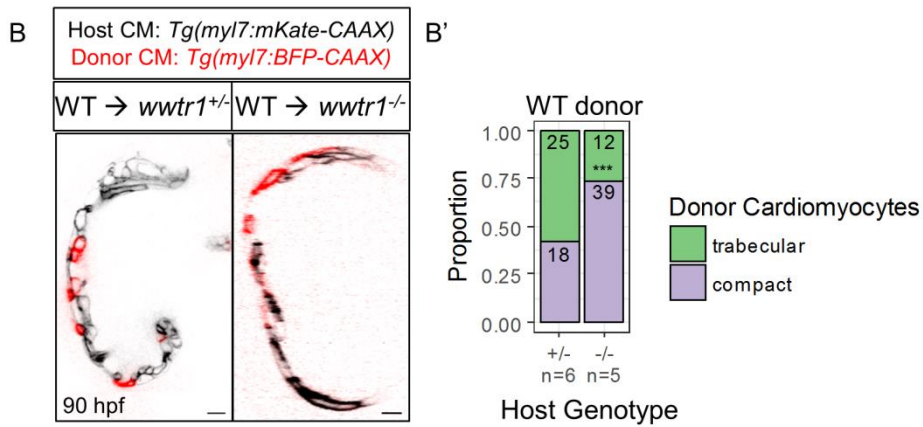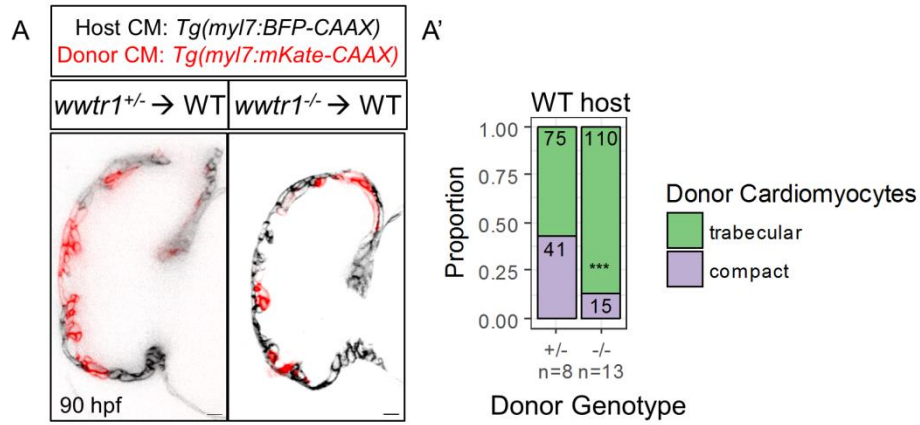injection construct
mKate n=13   CAWwtr1 n=18

98

Figure 28. Preference for *wwtr1* mutant cardiomyocytes to enter the trabecular layer in WT hearts. Sagittal or transverse (WT → *wwtr1^-/-^*) sections of mosaic hearts derived from transplanting *wwtr1^+/-^* or *wwtr1^-/-^* cells into WT hosts (A), and *vice versa* (B). Scale bars, 10 μm. (A', B') Proportion and number of donor cardiomyocytes contributing to the trabecular (green) and compact (purple) layers. *** - *P* < 0.001 by exact Binomial test. (C) The S79A substitution of Wwtr1 results in a constitutively active Wwtr1 protein (CAWwtr1). Peptide alignment of Wwtr1 to Yap1 surrounding the HXRXXS motif corresponding to S87 of Yap1. Substitution of S87 to Alanine renders Yap1 constitutively active. (C') Mid-sagittal sections of hearts from WT larvae injected with *myl7:mKate* (control) or *myl7:mKate-2A-CAWwtr1* plasmids. Scale bars, 10 μm. (C'') Proportion and number of cardiomyocytes positive for mKate or CAWwtr1 found in the trabecular (green) and compact (purple) layers. *** - *P* < 0.001 by exact Binomial test. This figure has been used in a manuscript by Lai et al. submitted to *Development*.
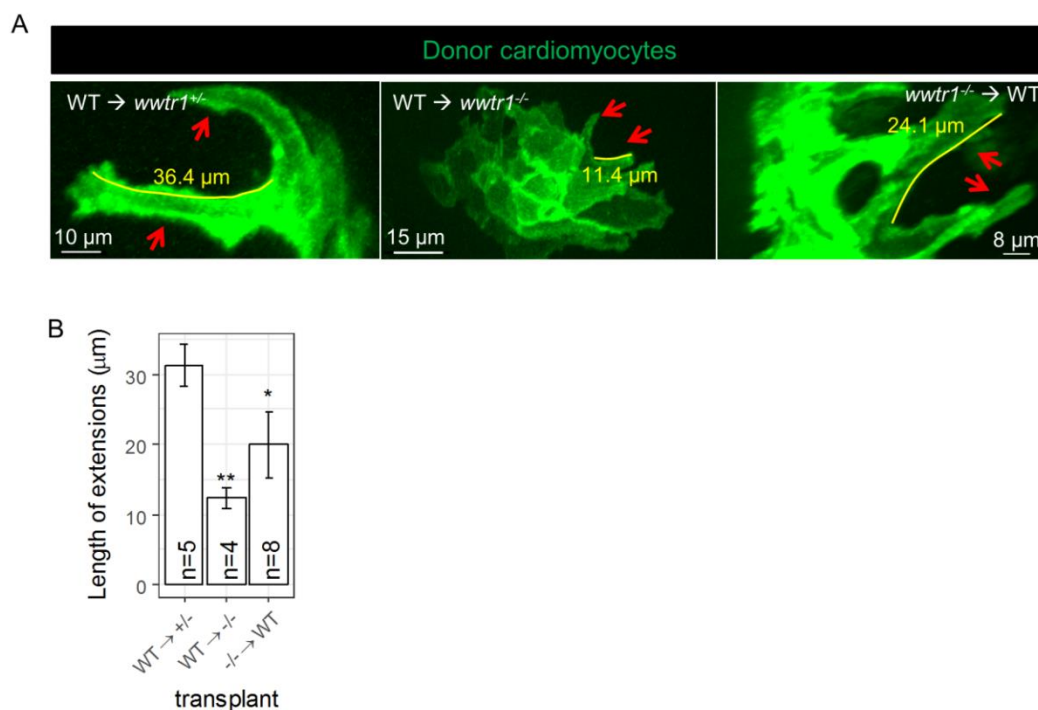

Figure 29. Trabecular cardiomyocyte morphology of donor cells. (A) Maximum intensity projections of donor cardiomyocytes (transplantation scheme on top left or top right). Red arrows point to "fork-like" extensions formed by a single trabecular cardiomyocyte. Yellow annotations show measurements of extension lengths. (B) Quantification of the length of these extensions. 'n' number of extensions from 3 WT →

wwtr1^{+/-}, 2 WT → *wwtr1*^{-/-}, and 3 *wwtr1*^{-/-} → WT hearts. Error bars are one unit of standard deviation. * - *P* < 0.05; ** - *P* < 0.01 by linear regression.
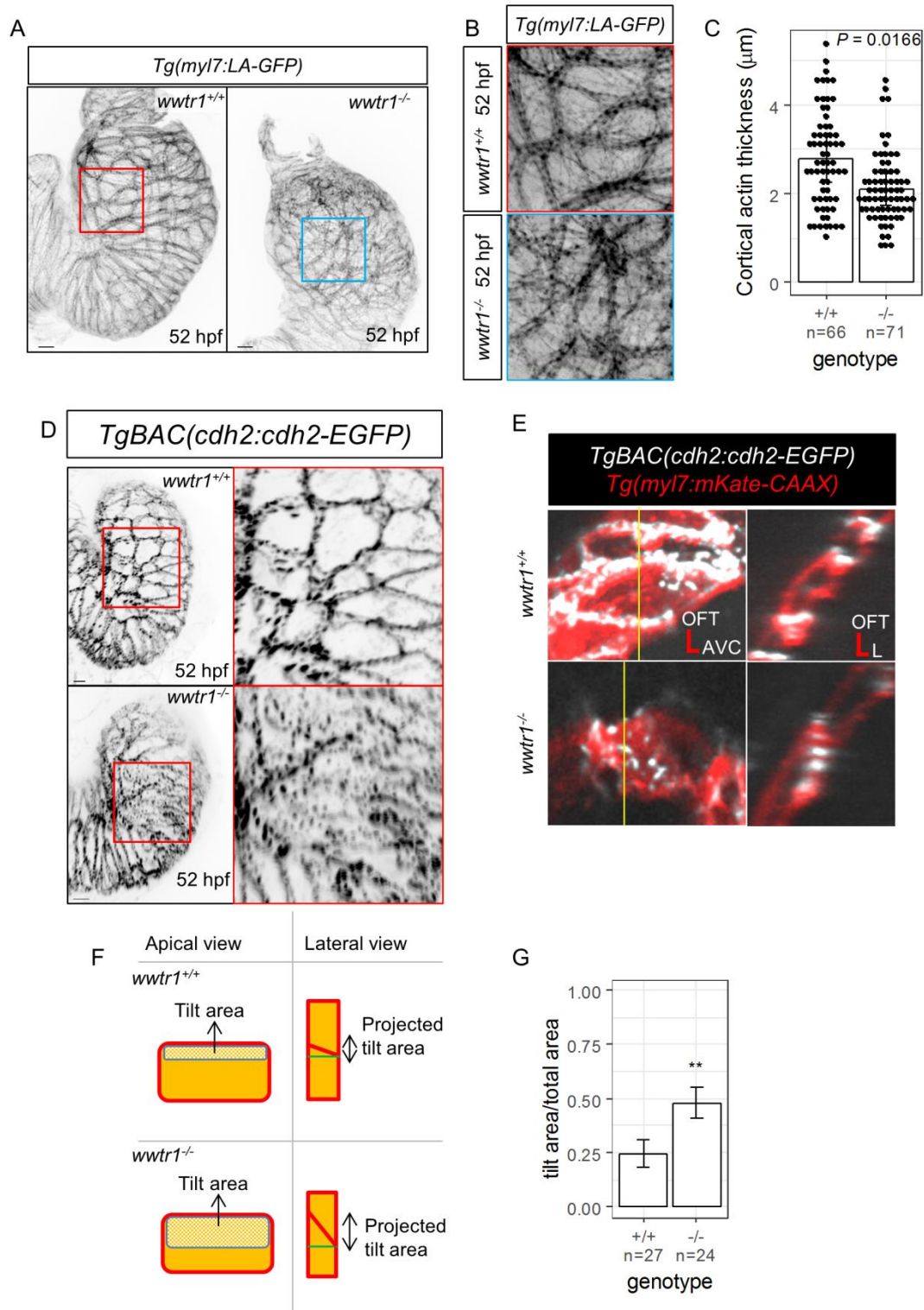
Figure 30. Disruptions to the architecture of the *wwtr1^{-/-}* compact wall myocardium. (A) Maximum intensity projections of 52 hpf zebrafish hearts showing the overall expression pattern of Lifeact-GFP (LA-GFP) which marks F-actin localization (8/8 *wwtr1$^{+/+}$* and 6/7 *wwtr1$^{-/-}$* hearts). Scale bars, 10 μm. (B) Apical views of cardiomyocytes corresponding to the area demarcated in their respective colors in (A). (C) Quantification of cortical actin thickness in ventricular cardiomyocytes. Each dot represents a cortical actin bundle ('n' number of cortical actin bundles were assessed from 6 *wwtr1$^{+/+}$* and 7 *wwtr1$^{-/-}$* hearts). *P*-value was calculated by two-sample t-test. (D) Maximum intensity projections of 52 hpf zebrafish hearts showing the distribution of N-cadherin in ventricular cardiomyocytes. 9/11 *wwtr1$^{+/+}$* hearts show distinct N-cadherin localization to cardiomyocyte junctions while 11/15 *wwtr1$^{-/-}$* hearts show punctate distribution of N-cadherin. Scale bars, 10 μm. (E) Apical views of cardiomyocytes and an optical cross-section corresponding to the yellow vertical lines. The N-cadherin distribution in *wwtr1$^{-/-}$* cardiomyocytes is punctate along the cell junctions and the lateral contacts are oblique to the apical surface (or 'tilted'). OFT - outflow tract; AVC - atrioventricular canal; L - lumen. (F) Schematic illustration of (E) and strategy to quantify 'tilting' of lateral contacts. The rectangle outlined in red is the 'total area', while the inner rectangle outlined in blue is the 'tilt area'. The green horizontal line in the "Lateral view" is perpendicular to the apical surface. (G) Proportion of 'tilt area' to 'total area' of ventricular cardiomyocytes ('n' number of cardiomyocytes were assessed from 4 hearts of each genotype). Error bars are one unit of standard deviation. ** - *P* < 0.01 by two-sample t-test. This figure has been used in a manuscript by Lai et al. submitted to *Development*.

4.3.7. Wwtr1 is required for myocardial wall architecture

At 52 hpf, while WT cardiomyocytes have organized striated cortical actin, $wwtr1^{-/-}$ cardiomyocytes have disorganized cortical actin that are also marginally thinner (Figure 30A-C). Further, I found that N-cadherin localization in $wwtr1^{-/-}$ cardiomyocytes appear to distribute about the apical and/or basal surfaces instead of the junctions (Figure 30D) (Cherian et al., 2016). To better visualize this phenotype, I took an optical cross section but found that N-cadherin in $wwtr1^{-/-}$ cardiomyocytes is indeed localized to the junctions but they are punctate and that the lateral membranes are oblique to the apical surface (Figure 30E-F). Nevertheless, the apico-basal polarity of $wwtr1^{-/-}$ cardiomyocytes is maintained as shown by the correct localization of the apical marker EGFP-Podxl and the basal marker Mark3a-tagRFP transgenes (Figure 31).

To understand this phenotype, I performed RNA-sequencing on isolated 57 -59 hpf hearts from $wwtr1^{-/-}$ and WT sibling embryos. I found 33 genes to be significantly differentially expressed (Figure 32A). With the help of Dr. Stefan Günther, these genes can be categorized into muscle and actomyosin genes, Wnt signaling, metabolism, extracellular matrix (ECM), ECM degradation and others (Figure 32B). To understand the actomyosin network and junctional phenotypes of $wwtr1^{-/-}$ hearts, I focused on genes that are related to these cellular structures that have been reported to express in the developing zebrafish hearts, namely *abraa (Chong et al., 2012)*, *myh10 (Huang et al., 2013)*, and *mybphb* (Figure 32C). Interestingly, I observed heart-specific downregulation of *mybphb* in $wwtr1^{-/-}$ embryos (Figure 32D). Interestingly, constitutive expression of *myl7*:EGFP-Wwtr1 could rescue the expression of *mybphb* (Figure 33A) as well as restore trabecular morphogenesis in $wwtr1^{-/-}$ hearts (Figure 33B).

4.3.8. Proposed model

This study revealed that Wwtr1, through the expression of *mybphb* and *myh10*, modulates compact wall morphogenesis that is important for trabeculation. Subsequently, Wwtr1 in the compact wall cardiomyocytes then regulate their decision to delaminate and initiate trabeculation (Figure 34).
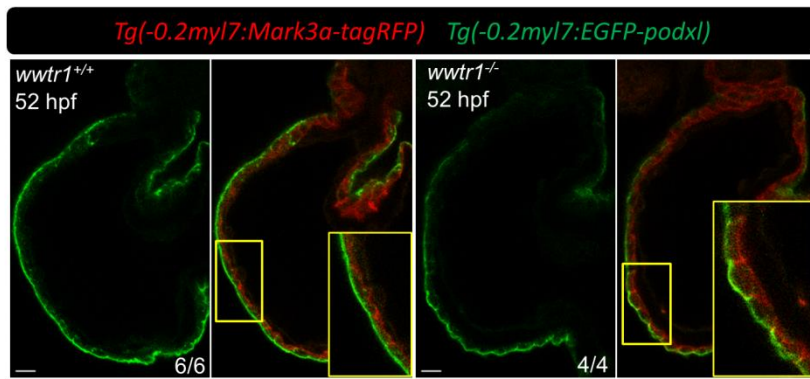
Figure 31. Apico-basal polarity of cardiomyocytes prior to trabeculation. Mid-sagittal sections of 52 hpf zebrafish hearts showing polarization, and correct localization of apico-basal transgene markers, EGFP-Podxl and Mark3a-tagRFP, in both *wwtr1$^{+/+}$* and *wwtr1$^{-/-}$* cardiomyocytes. Scale bars, 10 μm. This figure has been used in a manuscript by Lai et al. submitted to *Development*.
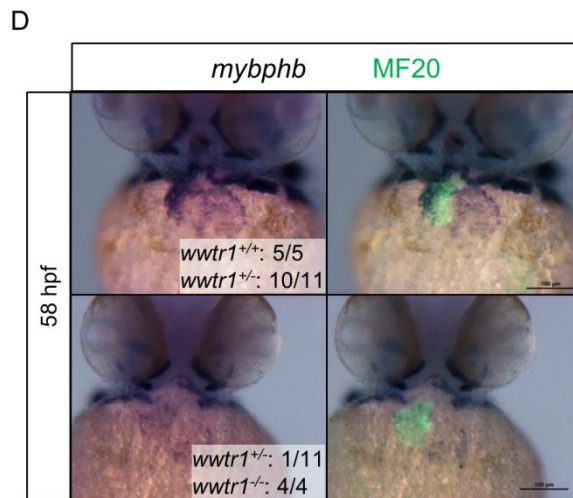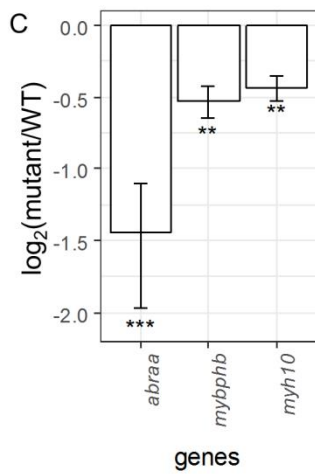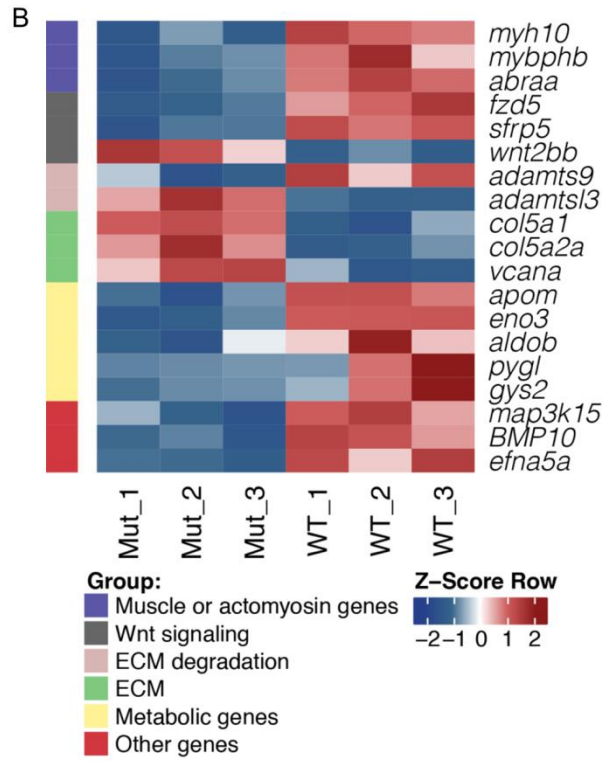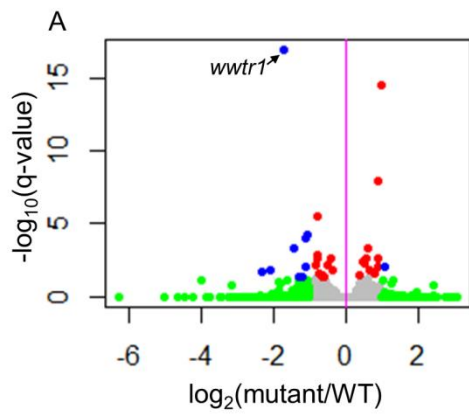
Figure 32. Transcriptomic analyses of *wwtr1*^{-/-} hearts compared to *wwtr1*^{+/+} hearts at 57-59 hpf. (A) Volcano plot comparing the transcriptomes of *wwtr1*^{-/-} to *wwtr1*^{+/+} sibling hearts collected at 57 – 59 hpf. As expected, *wwtr1* is significantly downregulated in *wwtr1*^{-/-} hearts. Each point represents a gene. Blue points are genes that are significantly differentially expressed; red points are genes that are moderately differentially expressed; green points are genes not significantly differentially expressed (see Materials and Methods for thresholds). (B) Heat map of z-scores of selected significantly differentially expressed genes assigned to functional categories. (C) Significantly differentially expressed genes that regulate muscle maturation and actin dynamics. Error bars are one unit of standard deviation from three RNAseq biological replicates of each genotype. ** - adjusted $P < 0.01$; *** - adjusted $P < 0.001$ calculated by DESEQ2. (D) Whole mount *in situ* hybridization for *mybphb* expression counterstained with MF20 reveals cardiac-specific loss of *mybphb* expression in *wwtr1*^{-/-} hearts. This figure has been used in a manuscript by Lai et al. submitted to *Development*.
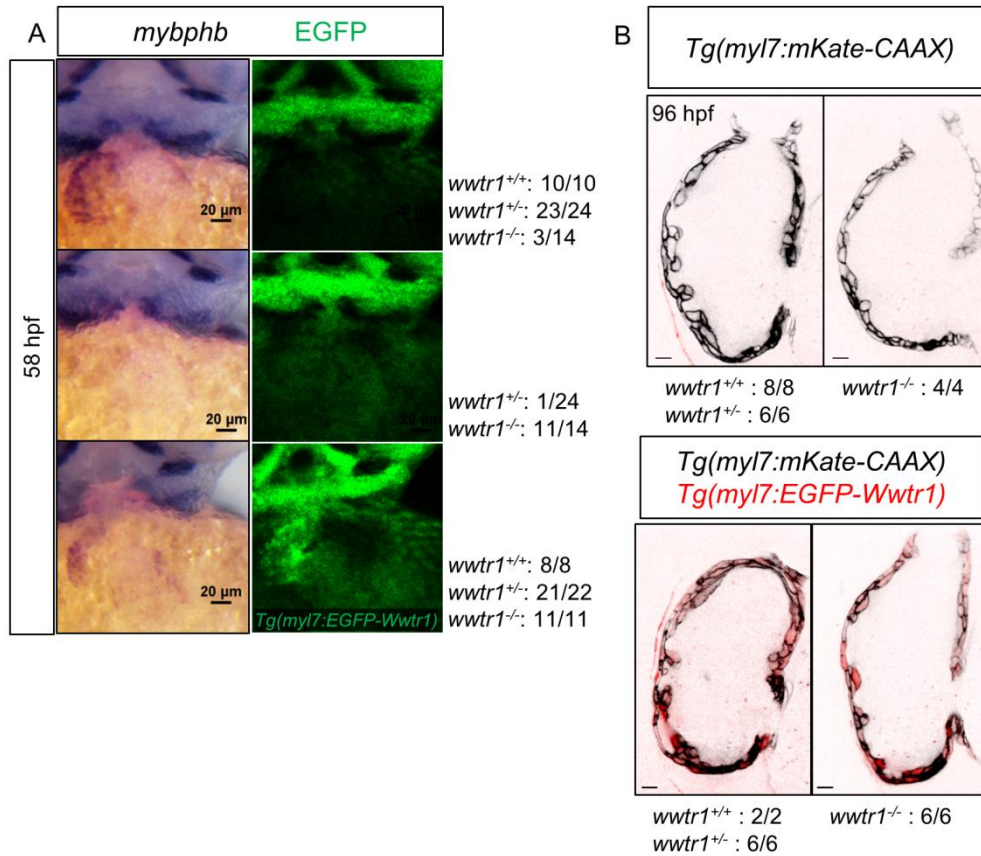
Figure 33. Constitutive myocardial expression of EGFP-Wwtr1 rescues the cardiac phenotypes of *wwtr1*^{-/-}. (A) Whole mount *in situ* hybridization for *mybphb* expression counterstained with EGFP reveals cardiac-specific loss of *mybphb* expression in *wwtr1*^{-/-} hearts. Mutant hearts with concurrent expression of *myl7*:EGFP-Wwtr1 show restoration of *mybphb* expression in the heart. (B) The *Tg(myl7:EGFP-Wwtr1)* line rescues the trabeculation phenotype of *wwtr1*^{-/-} hearts. Scale bars, 10 μm.
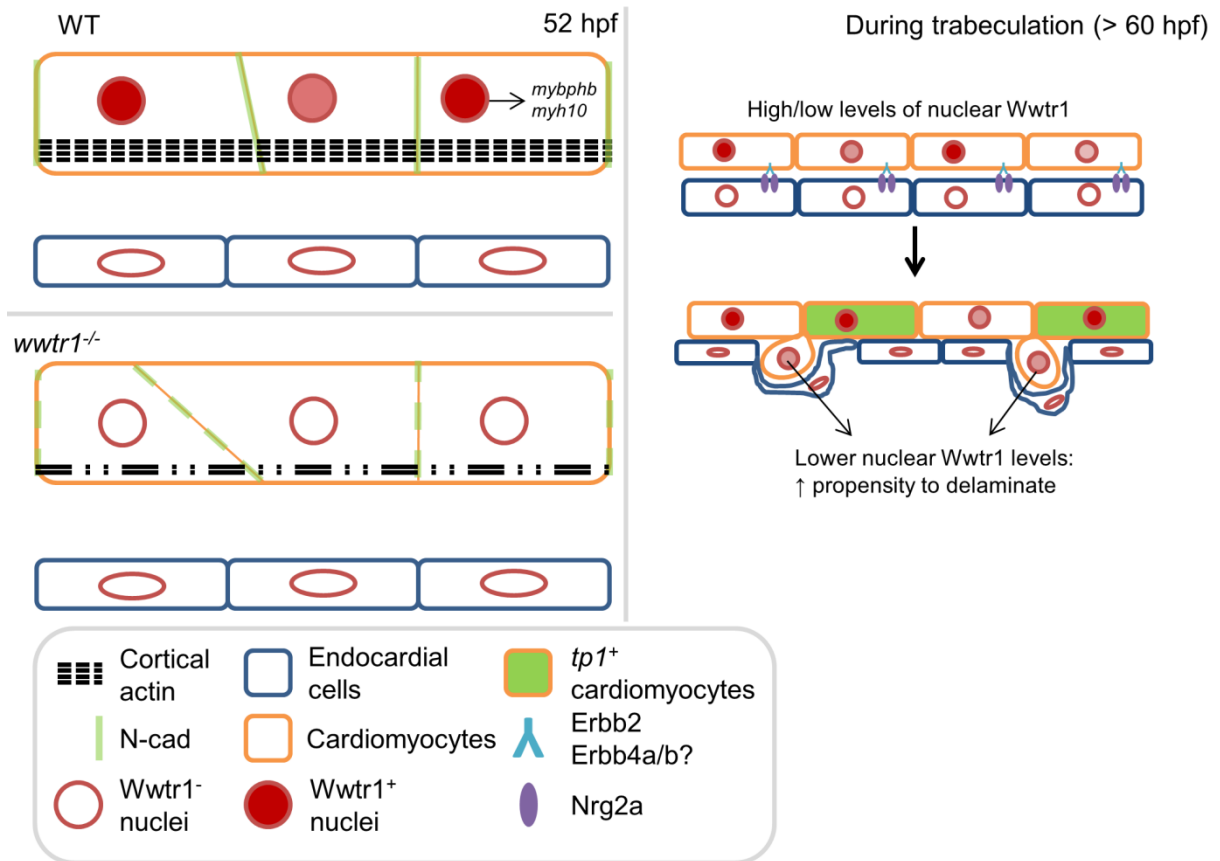
Figure 34. Proposed model: Wwtr1 maintains compact wall architecture and its activity modulates trabeculation. Wwtr1 is required for the compact wall architecture, as its loss leads to disorganized cortical actin and abnormal cell-cell junctions. Target genes of Wwtr1 likely involved in modulating muscle maturation or actomyosin contractility include *mybphb* and *myh10*. During trabeculation, cardiomyocytes in the compact wall show varying levels of nuclear Wwtr1 protein. Nuclear Wwtr1 protein levels appear to decrease in cardiomyocytes that enter the trabecular layer. Additionally, myocardial Notch signaling activity requires Wwtr1 function in a cell-autonomous manner. This figure has been used in a manuscript by Lai et al. submitted to *Development*.

5. DISCUSSION

5.1. Generation of zebrafish *yap1* and *wwtr1* mutants

The advent of next generation gene editing tools has enabled individual laboratories to generate their own mutants. To date, three (including this work) independent laboratories have generated their own *yap1* and *wwtr1* zebrafish mutants, and have invariably recapitulated the double homozygous mutant phenotype (Miesfeld et al., 2015; Nakajima et al., 2017). Therefore, the mutants generated for this thesis have no further surprises, except for the fact that each laboratory has investigated, in detail, different developmental processes, such as the LLP, eye, and vascular stability.

5.1.1. Overlapping roles of Yap1 and Wwtr1 - a comparative observation between zebrafish and medaka

It is worth noting that the observations made with the double *yap1;wwtr1* mutants recapitulates the *hirame* (*hir*) or *yap1* medaka mutant (Porazinski et al., 2015). However, a key difference is that the zebrafish mutant bodies are able to withstand gravitational force and maintain its 3D body morphology. Interestingly, it has been noted by other researchers that, to date, the medaka *wwtr1* gene is yet to be found (unpublished observations). This gap is either due to gene loss, or unresolved loci in the medaka genome or an incomplete expressed sequence tags (ESTs) collection.

Together with David Kimelman, we both found that the protein localization of Yap1 and Wwtr1 during zebrafish development overlaps considerably. Given that only double homozygous mutants exhibit the severe posterior body extension phenotype, it is likely that Yap1 and Wwtr1 have largely overlapping roles (Zanconato et al., 2015), due to the fact that *wwtr1* is a vertebrate paralog of *yap1* (Hilman and Gat, 2011). Nevertheless, single *yap1* and *wwtr1* mutants exhibit distinctive phenotypes in both murine and fish models (Hossain et al., 2007; Miesfeld et al., 2015; Morin-Kensicki et al., 2006; Xin et al., 2013), which does suggest that Yap1 and Wwtr1 can have exclusive roles in different contexts.

5.2. Role for blood flow and Yap1/Wwtr1 in vascular development

Secondary angiogenic sprouting contributes to the venous and lymphatic vascular network. Many signaling molecules have been shown to be involved in this process (Cha et al., 2012; Hogan et al., 2009a; Le Guen et al., 2014). In this study, I show that blood flow can regulate

Yap1/Wwtr1 activity in zebrafish endothelium and can modulate secondary angiogenic sprouting. However, the direct relationship of Yap1/Wwtr1 to secondary angiogenic sprouting is not clear, as the mutant embryos exhibit prior developmental phenotypes that can potentially affect this process.

5.2.1. Yap1/Wwtr1 modulates notochord and PCV morphogenesis

I showed here that the *yap1/wwtr1* compound mutants (*yap1$^{-/-}$;wwtr1$^{-/-}$* and *yap1$^{-/-}$;wwtr1$^{+/-}$*) exhibit an undulating notochord. The notochord is usually linear along the anterio-posterior axis, and this structure is thought to be mechanically coupled to the posterior growth of the embryo (Dray et al., 2013; McMillen and Holley, 2015). In collaboration with David Kimelman, he found that Fibronectin deposition around the notochord tissue is reduced, which could lead to uncoupling of the tissue mechanics between the notochord and its surrounding tissue (Kimelman et al., in revision). Given the intriguing expression pattern of Wwtr1 in the notochord, it would be interesting to investigate whether the nuclear/cytoplasmic regulation of Wwtr1 is modulated by mechanical inputs of the elongating trunk.

The midline is important for sending signaling cues to guide angioblasts to migrate to the midline and form the axial vessels (Fouquet et al., 1997; Helker et al., 2015; Sumoy et al., 1997). In addition, the midline expresses sonic hedgehog ligands to stimulate neighboring myotome to express *vegfaa*, which will induce arterial differentiation of endothelial cells as well as promote primary angiogenic sprouting (Lawson et al., 2002). The *yap1$^{-/-}$;wwtr1$^{+/-}$* embryos do not exhibit obvious angioblast migration phenotype, as they are able to form a lumenized DA. However, I observed that the PCV of these mutants are not aligned to the midline at 30-48 hpf. As the PCV is formed by a second wave of angioblast migration (Kohli et al., 2013), presumably guided by the midline as well, it would be interesting to investigate whether the PCV phenotype of *yap1$^{-/-}$;wwtr1$^{+/-}$* is due to the undulating notochord.

5.2.2. Mechanosensitive Yap1/Wwtr1 may relay blood flow signal in the endothelium for vISV sprouting

YAP1 and WWTR1 have been shown to respond to external mechanical cues such as cell shape, extracellular matrix (ECM) rigidity (Dupont et al., 2011), and recently, blood flow (Nakajima et al., 2017; Sabine et al., 2015; Wang et al., 2016). Blood flow was shown to be dispensable for primary angiogenic patterning, but its role in secondary angiogenic sprouting

was not thoroughly characterized (Isogai et al., 2003). Here, I show that blood flow modulates emergence of vISVs, and to a lesser extent, PLs. In my quantification, vISVs are *lyve1b*$^+$ vessels that have emerged from the PCV but not continuous to the horizontal myoseptum. PLs on the other hand, are *lyve1b*$^+$ vessels that line the horizontal myoseptum. As I cannot readily identify whether any of these 'vISVs' are connected to the segmental arteries, and without any blood circulation to confirm the identity of the *lyve1b*$^+$ vessel, a PL can be mistaken for a vISV. Interestingly, in the *yap1*$^{-/-}$;*wwtr1*$^{+/-}$ compound mutants, their trunks exhibit fewer vISVs and almost complete loss of PLs, suggesting that blood flow may modulate vISV emergence through Yap1/Wwtr1. Nevertheless, transplantation experiments will be needed to test if Yap1/Wwtr1 functions in a cell-autonomous manner to promote secondary angiogenic sprouting.

5.2.3.   Yap1/Wwtr1, through Cyr61, could regulate the expression of *vegfc* for the emergence and development of PLs

While the function of blood flow through Yap1/Wwtr1 could explain the reduction of vISVs in *yap1*$^{-/-}$;*wwtr1*$^{+/-}$ and *sih* morphant larvae, the further reductions in the number of PLs in *yap1*$^{-/-}$;*wwtr1*$^{+/-}$ larvae trunk is due to a different reason. I found that in these mutant trunks, expression of *vegfc*, *cxcl12a* are significantly lower. Furthermore, *vegfc*$^{+/-}$ larvae trunk show a more severe reduction in the number of PLs than the number of vISVs, which suggest that emergence of PLs is more sensitive to Vegfc availability than that of vISVs. Moreover, Cxcl12 was shown to specifically guide migration of PLs (Cha et al., 2012).

In summary, I propose that blood flow, through Yap1/Wwtr1 in the endothelium modulates vISV sprouting. In conjunction, Yap1 and Wwtr1 regulate the expression of *cyr61* in the hypochord. Cyr61 is then secreted from the hypochord to stimulate the DA to express *vegfc* (Mo et al., 2002), which in turn is processed by Ccbe1 to promote secondary angiogenic sprouting (Hogan et al., 2009a; Le Guen et al., 2014).

5.3.   Roles for Yap1/Wwtr1 in heart development

The Hippo signaling pathway has been shown to play an exquisite role in myocardial growth regulation (Heallen et al., 2011; von Gise et al., 2012; Xin et al., 2011). Here, I show that Yap1 participate in regulating ventricular wall growth in zebrafish, similarly described by others in mouse hearts (von Gise et al., 2012; Xin et al., 2011). However, I lacked experimental parameters such as cardiomyocyte proliferation. More pertinently, I found a

rather interesting and unexpected role for Wwtr1, which was poorly studied in mouse hearts. Here, I uncover novel functions for Wwtr1 during cardiac wall maturation.

5.3.1.   Wwtr1 modulates trabeculation

Spatiotemporal coordination of cardiomyocytes is key to the non-random arrangement of trabecular ridges that line the ventricular wall. Endocardial cells lining the outer-curvature of the ventricle uniformly express nrg2a (Rasouli and Stainier, 2017), which suggests equal probability for cardiomyocytes to be signaled by Nrg2a. Therefore, coordinating cardiomyocytes during trabeculation will require a lateral inhibition feedback loop, to ensure alternating cardiomyocytes delaminate leading to individual trabecular ridges. The Notch signaling pathway is known to drive lateral inhibition (Siekmann and Lawson, 2007) and was proposed to coordinate cardiomyocytes during trabeculation (Han et al., 2016). Consistent with this idea, lineage tracing of the *tp1* Notch reporter revealed that this signaling pathway could retain cardiomyocytes in the compact layer (Jiménez-Amilburu et al., 2016). We showed here that not only Wwtr1 is required cell-autonomously for the expression of *tp1* Notch reporter in cardiomyocytes, Wwtr1 can also promote cardiomyocytes to remain in the compact layer. However, the underlying mechanism of 'inhibition' remains poorly understood.

An alternative interpretation to the *tp1* lineage tracing experiment (Jiménez-Amilburu et al., 2016) is that only compact wall cardiomyocytes express the *tp1* reporter, which implies predetermination. However, if indeed predetermination is at play, then manipulation of cardiomyocyte Notch signaling has no bearing on trabeculation. Contrary to this expectation, exogenous temporal manipulation of Notch activation/inhibition can inhibit/promote compact wall cardiomyocytes to enter the trabecular layer (Han et al., 2016), similar to what I have observed when cardiomyocytes express CAWwtr1.

5.3.2.   A role for myofibril maturation in trabeculation?

The actomyosin morphology of compact wall cardiomyocytes markedly differs from trabecular cardiomyocytes (Reischauer et al., 2014; Wenink et al., 1996). This may suggest that compact wall cardiomyocytes, after delamination, reconfigure their actomyosin network to form the striated myofibrillar structures. During myofibrillogenesis of quail cardiomyocytes, it was proposed that pre-myofibrils containing Myh10 (non-muscle myosin IIB) first assemble around the cell cortex. Myh10 in the pre-myofibrils is then gradually

replaced with muscle myosins which matures into striated myofibrils that spans across the cell (Du et al., 2003; Sparrow and Schöck, 2009). As *wwtr1*$^{-/-}$ hearts express lower levels of *myh10*, one possibility is that the pre-myofibrils in *wwtr1*$^{-/-}$ cardiomyocytes have fewer Myh10 molecules to displace in order to form the mature striated myofibrils observed in trabecular cardiomyocytes, thereby permitting *wwtr1*$^{-/-}$ cardiomyocytes to enter the trabecular layer more readily. (Certain lines in this section have been quoted verbatim for publication in *Development* by Lai et al.)

5.3.3. Wwtr1 modulates compact wall morphogenesis

In this study, I showed that Wwtr1 is important for the organization of the actomyosin network and cardiomyocyte junctions in the compact wall. I report a likely disruption to the actomyosin contractility of *wwtr1*$^{-/-}$ cardiomyocytes through the downregulation of *myh10* expression. MYH10 plays critical roles in mouse cardiac development (Li et al., 2015; Ma et al., 2009; Tullio et al., 1997), and at the cellular level, MYH10 is essential for the maintenance of cardiomyocyte adherens junctions (Ma et al., 2009). Although the expression of *cdh2* is not significantly changed in *wwtr1*$^{-/-}$ hearts (Table 2), the levels of Cdh2/N-cadherin localized to the apical junctions appears lower (Fig. 30D, E), suggesting disruption to the apical junction complex (AJC), which is known to be important for epithelial organization and morphology (Nishimura et al., 2016; Verma et al., 2012). Therefore, it is possible that the aberrant cardiomyocyte organization in *wwtr1*$^{-/-}$ hearts (Fig. 30D-G) is a result of *myh10* downregulation.

I also found heart-specific downregulation of *mybphb*, a zebrafish ortholog of *MYBPH*, which encodes a protein that localizes to the A-band of the sarcomere (Gilbert et al., 1999). Together with sarcomeric myosin heavy chain, MYBPH is capable of inducing COS cells to assemble thick cables of F-Actin (Welikson and Fischman, 2002), suggesting that it may have a role in sarcomere assembly during cardiomyocyte development and that the disorganized cortical actin in *wwtr1*$^{-/-}$ cardiomyocytes (Fig. 30A-B) may be due to reduced *mybphb* expression.

A previous study by the Stainier lab implicated Asb2b in cardiomyocyte maturation (Fukuda et al., 2017). Similar to what we observed in *wwtr1*$^{-/-}$ ventricles (Fig. 30D-G), *asb2b* mutant atria exhibit overlapping cardiomyocytes and aberrant localization of N-cadherin (Fukuda et al., 2017). Although, I did not observe downregulation of *asb2b* in *wwtr1*$^{-/-}$ hearts, or *vice versa*, both mutants exhibit downregulation of *mybphb* and *myh10* expression of a similar

magnitude (Table 2). These observations support the notion that Wwtr1 through the expression of *mybphb* and *myh10* modulates cardiomyocyte morphogenesis, and suggest a possible cross-talk between Asb2b and Wwtr1 in this process. (Certain lines in this section have been quoted verbatim in a manuscript by Lai et al. submitted to *Development*)

5.3.4. Role for the compact wall in trabecular cardiomyocyte morphogenesis

Trabecular cardiomyocytes have striated parallel myofibrils that span across the long axis of the cell (Reischauer et al., 2014), reminiscent of striated myofibrils of myotubes. Previous studies have shown that manipulation of substrate compliance can influence focal adhesion strength and thus affect myofibril maturation in myotubes (Engler et al., 2004; Sparrow and Schöck, 2009). Notably, when myotubes were cultured on other myotubes, myofibrils could mature. On the other hand, when myotubes were cultured on fibroblasts, myofibrils could not mature, despite the expression of muscle myosins (Engler et al., 2004). Given these observations, it is possible that the morphological defects of *wwtr1$^{-/-}$* compact wall cardiomyocytes could not support cardiomyocytes in the trabecular layer, thus leading to reduced trabeculation.

5.3.5. A dual role for Wwtr1 in cardiac wall morphogenesis

Trabeculae emerge from the compact wall and thus, depend on it for proper morphogenesis. I have shown here that the disrupted compact wall architecture of *wwtr1$^{-/-}$* hearts is not able to support trabeculation. I postulate that Wwtr1 drives expression of *mybphb* and *myh10* to modulate compact wall morphogenesis. Once the compact wall is formed, the activity of Wwtr1 in compact cardiomyocytes is differentially regulated by the Hippo kinases, which then cooperates with Notch signaling to influence a cardiomyocyte's decision to delaminate leading to the formation of trabeculae. As Wwtr1 and Yap1 are well known for their mechanosensitive property, it will also be important to investigate how cardiac contractility/blood flow join forces with the Hippo, Neuregulin and Notch signaling pathways to spatiotemporally coordinate the complex morphogenetic movements of cardiomyocytes as the heart takes shape.

		wwtr1 (bns35) - 57-59 hpf			asb2b (bns33) - 50 hpf*	
EnsembleGeneID	GeneSymbol	log2(mutant/WT)	pvalue	padj	mutant/WT	log2(mutant/WT)
ENSDARG00000067719	wwtr1	-1.715603706	5.47E-22	1.12E-17	0.976317387	-0.034577871
ENSDARG00000102490	asb2b	0.057967247	0.6964	1	1.080569796	0.111792262
ENSDARG00000000103	myh10	-0.435382273	1.34E-06	0.00227	0.752598302	-0.41004806
ENSDARG00000003081	mybphb	-0.527469403	4.88E-06	0.00622	0.572487591	-0.804683673
ENSDARG00000038583	abraa	-1.446679863	1.79E-07	0.00046	2.169353009	1.117264836
ENSDARG00000020610	tnnt2a	-0.133235721	0.14778	1	1.2	0.263034406
ENSDARG00000052708	tnni1b	-0.120950487	0.22503	1	1.22	0.286881148
ENSDARG00000071090	actn2b	-0.127304097	0.18124	1	1.3	0.378511623
ENSDARG00000028213	ttn.2	0.007922422	0.9361	1	1.87	0.90303827
ENSDARG00000000563	ttn.1	-0.040177059	0.67606	1	1.36	0.443606651
ENSDARG00000018693	cdh2	-0.003511144	0.96995	1	1.33	0.411426246
ENSDARG00000041799	cx43	0.11144144	0.69123	1	0.99	-0.01449957
ENSDARG00000090598	pkp1a	0.699689327	0.14995	1	1.06	0.084064265
ENSDARG00000023026	pkp2	0.075913783	0.73694	1	1.06	0.084064265
ENSDARG00000051861	pkp3a	-0.017696385	0.96929	1	0.92	-0.120294234
ENSDARG00000045331	pkp4	0.030541531	0.90236	1	1.02	0.028569152
ENSDARG00000062590	pleca	0.007661889	0.9457	1	1.18	0.23878686
ENSDARG00000021987	plecb	0.028350281	0.76403	1	1.22	0.286881148
ENSDARG00000077506	tjp1a	0.018533334	0.84268	1	1.16	0.214124805
ENSDARG00000103959	pak1	0.077965231	0.66881	1	2.55	1.350497247
ENSDARG00000021309	rhoca	0.21969244	0.04992	1	1.52	0.604071324
ENSDARG00000069928	prkceb	0.293556517	0.12319	1	1.96	0.970853654
ENSDARG00000003008	prkcea	0.178881834	0.25644	1	1.83	0.871843649
ENSDARG00000092696	cyp11a2	0.621832575	0.53595	1	3.46	1.790772038
ENSDARG00000009418	mef2cb	-0.200134869	0.12759	1	2.62	1.389566812
ENSDARG00000025608	casp6l1	0.066421501	0.94244	1	2.6	1.378511623
ENSDARG00000090768	zp3.2	0.219605431	0.79365	1	2.09	1.063502942
ENSDARG00000043317	kita	0.182103726	0.53538	1	2.06	1.042644337
ENSDARG00000051879	abcc8	-0.102743953	0.75146	1	1.93	0.948600847
ENSDARG00000038095	socs1a	0.665677438	0.31657	1	1.84	0.879705766
ENSDARG00000030094	mal	0.086834355	0.83721	1	1.66	0.731183242
ENSDARG00000007560	sema3bl	0.103040456	0.52561	1	1.62	0.695993813
ENSDARG00000026611	socs3b	0.52618898	0.01192	0.87342	1.56	0.641546029
ENSDARG00000055283	id2a	-0.033192404	0.81597	1	1.4	0.485426827

* Fukuda, R., et al (2017). Nat. Commun. 8, 14495.

Table2. Gene expression profiles of *wwtr1* and *asb2b* mutant hearts. This table has been used in a manuscript by Lai et al. submitted to *Development.*

6. CONCLUSION

In conclusion, Yap1 and Wwtr1 are important for zebrafish development, especially in the cardiovascular system.

AIM 1: Generation of zebrafish *yap1* and *wwtr1* mutants

I successfully generated zebrafish *yap1* and *wwtr1* mutants and could study these mutants in different combinations, which exhibited distinctive phenotypes.

AIM 2: Elucidate the functions for Yap1/Wwtr1 in vascular development

Blood flow could regulate Yap1/Wwtr1 activity in endothelial cells and modulate secondary angiogenic sprouting. Additionally, I showed that Yap1/Wwtr1 regulates the expression of *cyr61* in the hypochord, which may induce *vegfc* expression in the DA to modulate the development of the venous and lymphatic vascular network.

AIM 3: Uncovering the roles of Yap1/Wwtr1 in heart development

In this study, I showed that Yap1 could be responsible for myocardial growth of the zebrafish hearts, similar to mouse hearts. Moreover, Yap1 and Wwtr1 may play an overlapping role for the midline migration of CPCs. Finally, my study of *wwtr1* mutants uncover novel functions for the Hippo signaling pathway especially for Wwtr1 in compact wall morphogenesis that is important for trabeculation. Additionally, my work reveals that Wwtr1 can modulate a cardiomyocyte's decision to enter the trabecular layer.

These comprehensive, but not exhaustive, studies of Yap1 and its vertebrate paralog Wwtr1 reveal their specific roles in morphogenesis, in addition to their classical function in promoting growth.

7. ZUSAMMENFASSUNG

Die Hippo-Signalwandler Yap1/Wwtr1 während der Entwicklung des Zebrafisches

Einleitung

Der Hippo-Signalweg ist ein Regulator des Gewebewachstums (Johnson and Halder, 2014). Es handelt sich dabei um eine Kinasen-Kaskade, die in der Phosphorylierung und Inaktivierung von YAP1/WWTR1 gipfelt. YAP1 und WWTR1 sind Co-Transkriptionsfaktoren von TEADs, dieser Komplex transloziert in die Nuclei und führt zu der Expression von Genen, welche die zelluläre Proliferation und das zelluläre Überleben fördern (Johnson and Halder, 2014). Der Hippo-Signalweg kann durch einige Signale stromaufwärts reguliert werden, wie beispielsweise GPCRs, apico-basale Polarität, Tight Junctions, etc. (Yu and Guan, 2013). Obwohl YAP1 und WWTR1 hauptsächlich durch die Hippo-Kinasen-Kassette reguliert werden, können sie trotzdem auch durch mechanische Signale und Tyrosin-Kinasen reguliert werden (Dupont et al., 2011; Taniguchi et al., 2015; Nakajima et al., 2017). Eine Fehlregulation dieses Signalweges kann zu einem unkontrollierten Wachstum und zu der Bildung von Tumoren führen (Zhou et al., 2009; Benhamouche et al., 2010; Cai et al., 2010; Lee et al., 2010; Lu et al., 2010; Zhang et al., 2010; Cox et al., 2016).

Das vaskuläre Netzwerk des Zebrafisches entsteht aus der Vaskulogenese und der Angiogenese. Die Vaskulogenese bildet die dorsale Aorta (DA) und die hintere Kardinalvene (PCV). Von der DA aus bildet eine erste Welle von angiogenen Sprossen, welche durch die Vegfa-Signalwirkung angetrieben wird, die arteriellen intersegmentalen Gefäße (aISVs) (Nasevicius et al., 2000; Rossi et al., 2016). In der Folge fördern Vegfc und Ccbe1 eine zweite Welle an angiogenen Sprossen von der PCV (Hogan et al., 2009; Le Guen et al., 2014), welche entweder in venöse intersegmentale Gefäße (vISVs) übergeht oder in parachordale Lymphangioblasten (PLs), deren Migration durch Cxcl12 und Cxcr4 gesteuert wird, um das lymphatische vaskuläre Netzwerk zu gestalten (Cha et al., 2012).

Das Zebrafischherz besteht aus zwei Hauptkammern, einem Atrium und einem Ventrikel. Während der embryonalen Entwicklung befinden sich kardiale Vorläuferzellen (CPCs) auf der lateralen Seite des Embryos und migrieren zu der Mittellinie, um die kardiale Scheibe zu bilden. Dieser Migrationsprozess ist von den Signalen abhängig, welche aus der synzytialen Dotterschicht (YSL) und dem Entoderm stammen (Alexander et al., 1999; Staudt and Stainier,

2012). Durch eine komplexe Serie an morphogenen Bewegungen formt sich die Herzscheibe zu einer Röhre, gefolgt von einer dextralen Schlingenbildung, welche den Ventrikel nach rechts und das Atrium nach links platzieren wird (Noël et al., 2013). Nach dem Aufblähen der Kammern durchlaufen die Kardiomyozyten in der ventrikulären Wand morphogenetische Bewegungen, initiiert durch den Neuregulin-Signalweg, um die Trabeculae zu formen. Während diesen Entwicklungsprozessen steigt die Anzahl an Kardiomyozyten durch Differenzierung und Proliferation. Das myokardiale Wachstum ist ein streng regulierter Prozess und in erwachsenen Säugerherzen sind Kardiomyozyten meist ruhend. Der Hippo-Signalweg, wie bereits erwähnt, ist ein limitierender Schlüsselfaktor für die Kardiomyozytenproliferation und das myokardiale Wachstum (Heallen et al., 2011; Xin et al., 2011; von Gise et al., 2012).

Die Herztrabekulierung ist ein hochregulierter Prozess und wird durch den Neuregulin-Signalweg initiiert (Gassmann et al., 1995; Meyer and Birchmeier, 1995; Lee et al., 1995; Liu et al., 2010; Rasouli and Stainier, 2017). Obwohl eine Vernetzung des Neuregulin- und des Hippo-Signalweges bekannt sind (Komuro et al., 2003; Haskins et al., 2014), wurde Letzterer nicht mit der Trabekulierung in Verbindung gebracht. Dennoch wurde die Funktion von WWTR1, einem Wirbeltier-Paralog von YAP1 während der Herzentwicklung, noch nicht charakterisiert.

Wegen der präproliferativen Funktion von YAP1 und WWTR1, werden beide oft als Onkogen assoziiert. Ihre Funktion in der embryonalen Entwicklung ist unterschätzt und daher ist es mein Ziel, ihre Funktion während der kardiovaskulären Entwicklung von Wirbeltieren anhand des Zebrafischmodells zu verstehen. In diesem Bericht präsentiere ich die sich überlappenden Rollen von Yap1 und Wwtr1 in der hinteren Körpermorphogenese und vaskulären Entwicklung. Zusätzlich werde ich zeigen, dass, während Yap1 eine Rolle in dem myokardialen Wachstum des Zebrafischherzen spielt, Wwtr1 eine charakteristische und spezifische Rolle in der Reifung der myokardialen Wand spielt.

Ergebnisse und Diskussion

Generierung von *yap1-* und *wwtr1*-Mutanten im Zebrafisch

Ich habe Zebrafischmutanten für die Gene *yap1* und *wwtr1* generiert, welche Frameshift-Indels sind und deren Transkripte nur in geringem Maße vorhanden sind, wahrscheinlich bedingt durch Nonsense-vermitteltem Verfall (Abbildung 4). Die Doppel-*yap1;wwtr1*-

Mutanten entwickeln sich normal bis zur 14-16 ss (somite stage/Somitenstufe), wenn der hintere Schwanz länger wird und sich vom Dottersack ausstülpt. Dieser Prozess fehlt vollständig in den Doppelmutanten, wie zuvor berichtet wurde (Miesfeld et al., 2015; Nakajima et al., 2017) (Abbildung 5). Zusätzlich habe ich viele Zellen in der umhüllenden Schicht (EVL) beobachtet, die absterben (Abbildung 6). Dennoch scheint die Somitenuhr robust zu bleiben, da die Anzahl an Somiten sich in diesen Mutanten nicht ändert (Abbildung 8). Interessanterweise werden nukleares Wwtr1 (und Yap1) in dem Notochord, der Bodenplatte, dem Hypochord, den vorderen Somiten und der Epidermis exprimiert (Abbildung 9). Zusammengefasst berichte ich von einer erfolgreichen Generierung von *yap1*- und *wwtr1*-Mutanten im Zebrafisch und dass Wwtr1 (und Yap1) in spezifischen Gewebebereichen im hinteren Körper exprimiert werden, um die Schwanzentwicklung und -Verlängerung voranzutreiben (Kimelman et al., in Revision).

Rolle für den Blutfluss und Yap1/Wwtr1 in der vaskulären Entwicklung

Die *in vivo* Yap1/Wwtr1-Aktivität im Endothelium wurde durch die Verwendung einer Tead-Reporterlinie studiert (Nakajima et al., 2017). Eine weitere Reporterlinie für die stellvertretende Detektion der Yap1/Wwtr1-Aktivität wurde im Argenton-Labor entwickelt. Diese Reporterlinie benutzt die Promotorregion des menschlichen *CTGF*-Gens, welches eines der kanonischen Ziele von den YAP1/WWTR1-TEADs ist. Das Reportersignal ist umfassend und schließt das Endothelium mit ein (Abbildung 10A). In besonderem Maße ist dieses Signal mäßig in $yap1^{-/-}$ und $wwtr1^{-/-}$ reduziert, obwohl nur Ersterer eine statistische Signifikanz erreicht (Abbildung 10B).

Die einzelnen *yap1*- und *wwtr1*-Mutanten zeigen keine offenkundigen vaskulären Musterungsdefekte im Rumpf und $yap1^{-/-}$ zeigen ein beschränktes kraniales Blutgefäßnetzwerk und weniger Hyaloidgefäße (was durch ein Kolobom verschlimmert wird) (Abbildung 11). Eine Vermischung der *wwtr1*-Mutanten mit einem teilweisen Verlust von *yap1* (z.B. $yap1^{+/-}$) führte nicht zu vaskulären Phänotypen im Rumpf (Abbildung 11B). Auf der anderen Seite zeigen $yap1^{-/-};wwtr1^{+/-}$-Embryos Störungen in einigen vaskulären Entwicklungsprozessen. Diese Mutanten (und die Doppelmutanten) zeigen zunächst ein gewelltes Notochord (Abbildungen 5A, 7). Weiterhin sind die meisten der $yap1^{-/-};wwtr1^{+/-}$-Embryos unfähig, einen Blutfluss aufzubauen, teilweise durch eine Cardia bifida (Abbildung 12A). Dennoch wird die DA gebildet und lumenisiert, jedoch ist die PCV von der Mittellinie abgewichen (Abbildungen 12C-E, 13A-C) und es wird beobachtet, dass sie in einige

querverlaufende Sektionen der Mutantenlarven geteilt ist (Abbildung 12C-G, 13C). Trotzdem scheint die primäre segmentale Gefäßmusterung normal zu sein (Abbildung 15A). Ich habe allerdings eine schwerwiegende Reduktion im sekundären angiogenen Sprießen beobachtet (Abbildung 15B-C, 16B). Da diese Mutanten eine schwächere Blutzirkulation haben, habe ich die Anzahl an vISVs und PLs in den *sih*-Morphanten quantifiziert und herausgefunden, dass die Anzahl von vISVs und PLs reduziert ist, Erstere ist dabei stärker reduziert als Letztere (Abbildung 16A). Daher kann der Blutfluss das sekundäre angiogene Sprießen modulieren und der *yap1$^{-/-}$;wwtr1$^{+/-}$*-Phänotyp kann eine indirekte Folge der Mutation sein. Alternativ reguliert der Blutfluss die Aktivität von Yap1/Wwtr1 im Endothelium (Abbildung 10B), um das sekundäre Sprießen zu modulieren (Abbildung 19). Mosaikanalysen sollten darüber aufklären, ob Yap1/Wwtr1 zellautonom auf das sekundäre Sprießen wirken und es sollte diese beiden konkurrierenden Modelle erläutern.

Ich habe diesen Phänotyp weiter untersucht und herausgefunden, dass *vegfc* und *cxcl12a* in *yap1$^{-/-}$;wwtr1$^{+/-}$*-Rümpfen signifikant herunterreguliert sind (Abbildung 17A, B), aber nicht in *sih*-Morphantenrümpfen (Abbildung 17D). Außerdem weisen *vegfc$^{+/-}$* eine schwerwiegendere Reduktion in der Anzahl an PLs als in der Anzahl an vISVs auf (Abbildung 18), was den deutlichen Verlust an PLs in *yap1$^{-/-}$;wwtr1$^{+/-}$* -Larven erklären könnte. Interessanterweise ist ein kanonisches Ziel von Yap1/Wwtr1, *cyr61*, welches im Hypochord exprimiert wird, signifikant herunterreguliert (Abbildung 17C). Weiterhin ist es möglich, da CYR61 die Expression von *Vegfc* (Mo et al., 2002) induzieren kann, dass Yap1/Wwtr1 im Hypochord die Expression von *cyr61* reguliert, was im Umkehrschluss die Expression von *vegfc* fördert, um das sekundäre angiogene Sprießen zu beeinflussen (Abbildung 19).

Rolle von Yap1/Wwtr1 in der Entwicklung des Herzens

Yap1 und Wwtr1 spielen eine Rolle in der CPC-Migration zur Mittellinie, da die *yap1$^{-/-}$;wwtr1$^{+/-}$*-Embryonen eine Cardia bifida aufweisen (Abbildung 12A) (Nakajima et al., 2017). Jedoch bleibt der Mechanismus unklar und eine vorhergehende Publikation über *yap1*-Morphanten könnte durch Morpholino-Toxizität entstanden sein und benötigt eine Neubewertung (Fukui et al., 2014; Nakajima et al., 2017). Durch kardiale Phänotypen von einzelnen Mutanten habe ich gezeigt, dass Yap1 das myokardiale Wachstum in den Fischen reguliert (Abbildung 20), ebenso wie in Mäuseherzen (Xin et al., 2011; von Gise et al., 2012). Auf der anderen Seite moduliert Wwtr1 die Reifung der Myokardwand.

In meiner Studie habe ich herausgefunden, dass Wwtr1 in den Kardiomyozyten des sich entwickelnden Fischherzen exprimiert wird (Abbildung 21). Bemerkenswerterweise weisen die Nuclei der Kardiomyozyten in den Trabeculae eine verringerte Immunfärbungsintensität als die Kardiomyozyten der kompakten Wand auf (Abbildung 22C). Diese Beobachtung ist entscheidend, da Mutanten-Kardiomyozyten in einem Mosaik-WT-Herzen bevorzugt die Trabekelschicht bevölkern (Abbildung 28A). Zudem sind Kardiomyozyten, die konstitutiv aktives Wwtr1 exprimieren öfter in der kompakten Schicht vertreten als die Kontrolle (Abbildung 28C). Diese Daten suggerieren, dass Wwtr1 Kardiomyozyten davon abhalten kann, in die Trabekelschicht einzuwandern und die Ergebnisse prognostizieren, dass *wwtr1*-Mutantenherzen einen Hypertrabekulierungs-Phänotyp aufweisen könnten. Konträr zu den Vermutungen zeigten die *wwtr1*-Muantenherzen eine ausgesprochen geringere Anzahl an Kardiomyozyten in ihrer Trabekelschicht und es fehlt ihnen deutlich an Trabekelleisten (Abbildung 23). Dieses Paradoxon steigert die Wahrscheinlichkeit, dass Wwtr1 eine Rolle in der Entwicklung der kompakten Wand spielt, welche wichtig ist für die Trabekulierung. Bestätigend für diese Idee wirkt die Beobachtung, dass WT-Kardiomyozyten in Mosaik-Mutanten-Herzen weniger oft in der Trabekelschicht gefunden werden (Abbildung 28B) und Mutanten-Herzen eine mangelhafte Morphologie der Trabekel-Kardiomyozyten aufweisen (Abbildung 24C). Unter Benutzung transgener Linien, die das Aktomyosin-Netzwerk und die N-Cadherin (Cdh2)-Lokalisierung anzeigen, habe ich herausgefunden, dass die kortikalen Aktinbündel der Mutanten-Kardiomyozyten in Unordnung und marginal dünner sind (Abbildung 30A-C). Zudem habe ich beobachtet, dass die Kardiomyozyten-Verbindungen unterbrochen sind, bedingt durch die punktuelle N-Cadherinverteilung entlang der lateralen Membranen der Mutanten-Kardiomyozyten (Abbildung 30D-G). Von meinen Transkriptomanalysen habe ich *myh10* und *mybphb* als mutmaßliche Kandidaten identifiziert, welche die Grundlage für die Funktion von Wwtr1 als Modulator der Architektur der kompakten Wand bilden (Abbildung 32).

Zusammengefasst spielt Wwtr1 eine wichtige Rolle in der Entwicklung der Kardiomyozyten in der kompakten Wand, indem es eine einwandfreie Morphogenese des Kardiomyozyten-Aktomyosin-Netzwerks und deren Verknüpfungen moduliert. Während der Trabekulierung moduliert Wwtr1 negativ die Entscheidung einer Herzmuskelzelle, in die Trabekelschicht einzuwandern. Zudem deckt meine Studie auf, dass die myokardiale Notch-Aktivität Wwtr1 in einer zellautonomen Weise benötigt (Abbildungen 25 und 27). Mit der Tatsache, dass vorhergehende Studien gezeigt haben, dass die Notch-Aktivität die Kardiomyozyten in

ähnlicher Weise davon abhält, die Trabekelschicht zu betreten, (Han et al., 2016; Jiménez-Amilburu et al., 2016) wäre es interessant die Vernetzung des Hippo- und des Notch-Signalweges zu untersuchen, welche die Regulation des Verhaltens der Kardiomyozyten während der Trabekulierung betont. Schließlich, da mechanische Kräfte (Herzkontraktion und Blutfluss) kritische Rollen in der kardialen Trabekulierung spielen, (Samsa et al., 2015; Peshkovsky et al., 2011) wird es wichtig sein, weiter zu untersuchen, wie Wwtr1 diese mechanischen Signale weiterleiten kann und die Kardiomyozyten während der Entwicklung und Reifung der Kardiomyozyten beeinflussen kann.

Fazit

Der Hippo-Signalweg wurde als ein wichtiger Tumorsuppressor-Signalweg identifiziert, da er eine essentielle Rolle in der negativen Regulation der Onkogene und seiner nuklearen Effektoren, YAP1 und WWTR1 spielt. In meiner aktuellen Studie habe ich auffällige Morphogenese-Phänotypen von den unterschiedlichen Kombinationen von *yap1* und *wwtr1*-Zebrafischmutanten während der Entwicklung gefunden. Yap1 und Wwtr1 werden für die hintere Körpermorphogenese, die Entwicklung des Notochord, das sekundäre angiogene Sprießen und die Migration von CPC zur Mittellinie benötigt. Yap1 moduliert das myokardiale Wachstum, wie bereits in Mausherzen dokumentiert wurde, währendWwtr1 eine spezifische Rolle in der Entwicklung und Reifung der myokardialen Wand spielt. Daher hat meine Studie über Yap1 und Wwtr1 in der Wirbeltierentwicklung eine neue Rolle für den Hippo-Signalweg in der Gewebsmorphogenese aufgedeckt und sollte eine neue Perspektive auf diese Signalwege in verschiedenen biologischen Prozessen ermöglichen.

8. ENGLISH SUMMARY

The Hippo signaling transducers Yap1/Wwtr1 in zebrafish development
Introduction

The Hippo signaling pathway is a regulator of tissue growth (Johnson and Halder, 2014). It is a kinase cascade that culminates to the phosphorylation and inactivation of YAP1/WWTR1. YAP1 and WWTR1 are co-transcription factors of TEADs, this complex translocates into the nuclei and drive the expression of genes that promote cellular proliferation and survival (Johnson and Halder, 2014). The Hippo signaling pathway can be regulated by a number of upstream cues such as GPCRs, apico-basal polarity, tight junctions, etc (Yu and Guan, 2013). Although YAP1 and WWTR1 are primarily regulated by the Hippo kinase cassette, they nevertheless can be regulated by mechanical cues and tyrosine kinases (Dupont et al., 2011; Nakajima et al., 2017; Taniguchi et al., 2015). Dysregulation of this signaling pathway can lead to uncontrolled growth and tumorigenesis (Benhamouche et al., 2010; Cai et al., 2010; Cox et al., 2016; Lee et al., 2010; Lu et al., 2010; Zhang et al., 2010; Zhou et al., 2009).

The zebrafish vascular network arise from vasculogenesis and angiogenesis. Vasculogenesis gives rise to the dorsal aorta (DA) and posterior cardinal vein (PCV). From the DA, a first wave of angiogenic sprouts, driven by Vegfa signaling, establishes the arterial intersegmental vessels (aISVs) (Nasevicius et al., 2000; Rossi et al., 2016). Subsequently, Vegfc and Ccbe1 promotes a second wave of angiogenic sprouts from the PCV (Hogan et al., 2009a; Le Guen et al., 2014), which either commit into venous intersegmental vessels (vISVs), or into parachordal lymphangioblasts (PLs) whose migration is guided by Cxcl12 and Cxcr4 to pattern the lymphatic vascular network (Cha et al., 2012).

The zebrafish heart is composed of two principal chambers, one atrium and one ventricle. During embryonic development, cardiac progenitor cells (CPCs) are positioned in the lateral sides of the embryo and will migrate to the midline to fuse and form the cardiac disc. This migration process is dependent on signaling cues originating from the yolk syncytial layer (YSL) and the endoderm (Alexander et al., 1999; Staudt and Stainier, 2012). Through a complex series of morphogenetic movements, the cardiac disc becomes a tube, followed by dextral looping that will place the ventricle to the right and atrium to the left (Noël et al., 2013). After ballooning of the chambers, the cardiomyocytes in the ventricular wall undergo morphogenetic movements, initiated by Neuregulin signaling, to form the trabeculae. During

these developmental processes, the number of cardiomyocytes increases through differentiation and proliferation. Myocardial growth is a tightly regulated process and in mammalian adult hearts, cardiomyocytes are mostly quiescent. The Hippo signaling pathway, as mentioned earlier, is a key limiting factor to cardiomyocyte proliferation and myocardial growth (Heallen et al., 2011; von Gise et al., 2012; Xin et al., 2011).

Cardiac trabeculation is a highly regulated process and is initiated by the Neuregulin signaling pathway (Gassmann et al., 1995; Lee et al., 1995; Liu et al., 2010; Meyer and Birchmeier, 1995; Rasouli and Stainier, 2017). Although a cross-talk between the Neuregulin and Hippo signaling pathway has been reported (Haskins et al., 2014; Komuro et al., 2003), the latter pathway was not implicated in trabeculation. However, the function of WWTR1, a vertebrate paralog of YAP1, during heart development has not been characterized.

Given the pro-proliferative function of YAP1 and WWTR1, they are often associated as an oncogene. Their function in embryonic development is understudied and thus, my aim is to understand their function in vertebrate cardiovascular development using zebrafish as a model. In this report, I present the overlapping roles of Yap1 and Wwtr1 in posterior body morphogenesis and vascular development. In addition, I will also show that while Yap1 plays a role in myocardial growth in zebrafish heart, Wwtr1 plays a distinctive and specific role in myocardial wall maturation.

Results and Discussion

Generation of zebrafish *yap1* and *wwtr1* mutants

I generated zebrafish *yap1* and *wwtr1* mutants, which are frameshift indels and their transcripts are less abundant likely due to nonsense-mediated decay (Figure 4). The double *yap1;wwtr1* mutants develop normally until the 14-16 ss, when the mutant posterior tail fail to evert out from the yolk sac and elongate (Figure 5). Additionally, I observed many cells in the EVL were dying (Figure 6). Nevertheless, the somite clock remains robust as the number of somites is not changed in these mutants (Figure 8). Interestingly, nuclear Wwtr1 (and Yap1) are expressed in the notochord, floor plate, hypochord, anterior somites and epidermis (Figure 9). In summary, I report successful generation of zebrafish *yap1* and *wwtr1* mutants, and that Wwtr1 (and Yap1) are expressed in specific tissue domains in the posterior body to drive tail development and elongation (Kimelman et al., in revision).

Role for blood flow and Yap1/Wwtr1 in vascular development

in vivo Yap1/Wwtr1 activity in the endothelium has been studied through the use of a Tead reporter line (Nakajima et al., 2017). Another reporter line for the proxy detection of Yap1/Wwtr1 activity has been developed in the Argenton lab. This reporter line utilizes the promoter of human *CTGF* gene, which is one of the canonical targets of YAP1/WWTR1-TEADs. The reporter signal is broad and includes the endothelium (Figure 10A). Notably, this signal is modestly reduced in *yap1*$^{-/-}$ and *wwtr1*$^{-/-}$ endothelium, although only the former reached statistical significance (Figure 10B).

The single *yap1* and *wwtr1* mutants do not show overt trunk vascular patterning defects and *yap1*$^{-/-}$ exhibit a truncated cranial vasculature network and fewer hyaloid vessels (which is worsened by coloboma) (Figure 11). Compounding the *wwtr1* mutants with partial loss of *yap1* (i.e. *yap1*$^{+/-}$) did not result in any trunk vascular phenotypes (Figure 11B). On the other hand, *yap1*$^{-/-}$*;wwtr1*$^{+/-}$ embryos exhibit perturbation in a number of vascular developmental processes. These mutants (and double mutants) show an undulating notochord by 20 hpf (Figures 5A, 7). Furthermore, most of the *yap1*$^{-/-}$*;wwtr1*$^{+/-}$ embryos are not able to establish blood flow, in part due to cardia bifida (Figure 12A). Nevertheless, the DA is formed and lumenized, but the PCV has deviated from the midline (Figures 12C-E, 13A-C), and appears to 'split' in some transverse sections of mutant larvae (Figure 12C-g, 13C). Nevertheless, the primary segmental vascular pattern appears normal (Figure 15A). However, I observed a severe reduction in secondary angiogenic sprouting (Figures 15B-C, 16B). As these mutants have a weaker blood circulation, I quantified the number of vISVs and PLs in *sih* morphants and found that the number of vISVs and PLs were reduced, the former was reduced to a larger extent than the latter (Figure 16A). Therefore, blood flow can modulate secondary angiogenic sprouting, and the *yap1*$^{-/-}$*;wwtr1*$^{+/-}$ phenotype can be secondary to weak blood flow. Alternatively, blood flow regulates Yap1/Wwtr1 activity in the endothelium (Figure 10B) to modulate secondary sprouting (Figure 19). Mosaic analyses should inform whether Yap1/Wwtr1 functions cell-autonomously on secondary sprouting and clarify these two competing models.

I further investigated this phenotype and found that *vegfc* and *cxcl12a* are significantly downregulated in *yap1*$^{-/-}$*;wwtr1*$^{+/-}$ trunks (Figure 17A, B), but not *sih* morphant trunks (Figure 17D). Moreover, *vegfc*$^{+/-}$ exhibit a more severe reduction in the number of PLs than vISVs (Figure 18), which may explain the marked loss of PLs in *yap1*$^{-/-}$*;wwtr1*$^{+/-}$ larvae.

Interestingly, a canonical target of Yap1/Wwtr1, *cyr61*, which is expressed in the hypochord is significantly downregulated (Figure 17C). Furthermore, CYR61 was shown to induce *Vegfc* expression (Mo et al., 2002), it is possible that Yap1/Wwtr1 in the hypochord regulates expression of *cyr61*, which in turn promotes the expression of *vegfc* to affect secondary angiogenic sprouting (Figure 19).

Roles for Yap1/Wwtr1 in heart development

Yap1 and Wwtr1 have a role in CPC migration to the midline, as the *yap1*$^{-/-}$*;wwtr1*$^{+/-}$ embryos exhibit cardia bifida (Figure 12A) (Nakajima et al., 2017). However, the mechanism remains unclear, and a previous publication on *yap1* morphant may be due to morpholino toxicity and requires reevaluations (Fukui et al., 2014; Nakajima et al., 2017). From cardiac phenotypes of *yap1* mutants, I showed that Yap1 in fish regulates myocardial growth (Figure 20), just like in mouse hearts (von Gise et al., 2012; Xin et al., 2011). On the other hand, Wwtr1 modulates myocardial wall maturation.

In my study, I found that Wwtr1 is expressed in the cardiomyocytes of the developing fish heart (Figure 21). Notably, nuclei of cardiomyocytes in the trabeculae exhibit a reduced immunostaining intensity than that of compact wall cardiomyocytes (Figure 22C). This observation is key, as mutant cardiomyocytes in mosaic WT hearts preferentially populate the trabecular layer (Figure 28A). Moreover, cardiomyocytes that express constitutively active Wwtr1 are more likely found in the compact layer than the control (Figure 28C). These data suggest that Wwtr1 can inhibit cardiomyocytes from entering the trabecular layer, and predicts that the *wwtr1* mutant heart would exhibit a hypertrabeculation phenotype. Contrary to expectations, the *wwtr1* mutant hearts show markedly fewer cardiomyocytes in the trabecular layer and largely lacking the trabecular ridges (Figure 23). This paradox raises a possibility that Wwtr1 has a role in compact wall development which is important for trabeculation. Corroborating with this idea is the observation that WT cardiomyocytes in mosaic mutant hearts are found less frequently in the trabecular layer (Figure 28B), and mutant hearts exhibit poor morphology of trabecular cardiomyocytes (Figure 24C). Using transgenic lines that report the actomyosin network and N-cadherin (Cdh2) localization, I find that the cortical actin bundles of mutant cardiomyocytes are in disarray and are marginally thinner (Figure 30A-C), and that the cardiomyocyte junctions appear disrupted as evident by the punctate N-cadherin distribution along the lateral membranes of mutant cardiomyocytes (Figure 30D-G). From my transcriptomic analyses, I identified *myh10* and *mybphb* as

putative candidates underlying the function of Wwtr1 in modulating compact wall architecture (Figure 32).

In summary, Wwtr1 plays an important role in the development of the compact wall cardiomyocytes, by modulating proper morphogenesis of the cardiomyocyte actomyosin network and junctions. During trabeculation, Wwtr1 negatively modulates a cardiomyocyte's decision to enter the trabecular layer. Moreover, my study revealed that myocardial Notch activity requires Wwtr1 in a cell-autonomous manner (Figures 25 and 27). Given that previous studies have shown that Notch activity similarly inhibits cardiomyocytes from entering the trabecular layer (Han et al., 2016; Jiménez-Amilburu et al., 2016), it would be interesting to investigate the cross-talk of the Hippo and Notch signaling pathways that underscores the regulation of cardiomyocyte behavior during trabeculation. Finally, as mechanical forces (cardiac contraction and blood flow) have crucial roles for cardiac trabeculation (Peshkovsky et al., 2011; Samsa et al., 2015), it will be important to further investigate how Wwtr1 can relay these mechanical signals and affect cardiomyocytes during heart development and maturation.

Conclusions

The Hippo signaling pathway was identified as an important tumor suppressor pathway as it plays essential function in negatively regulating the oncogenes, and its nuclear effectors, YAP1 and WWTR1. In my current study, I found striking morphogenesis phenotypes from the different combinations of *yap1* and *wwtr1* zebrafish mutants during development. Yap1 and Wwtr1 are required for posterior body morphogenesis, notochord development, secondary angiogenic sprouting, and CPC migration to the midline. Yap1 modulates myocardial growth of zebrafish hearts, as was documented in mouse hearts; while Wwtr1 plays a specific role in myocardial wall development and maturation. Therefore, my study of Yap1 and Wwtr1 in vertebrate development has revealed a novel role for the Hippo signaling pathway in tissue morphogenesis and should illuminate a new perspective of this pathway in various biological processes.

9. REFERENCES

Agarwala, S., Duquesne, S., Liu, K., Boehm, A., Grimm, L., Link, S., König, S., Eimer, S., Ronneberger, O. and Lecaudey, V. (2015). Amotl2a interacts with the Hippo effector Yap1 and the Wnt/β-catenin effector Lef1 to control tissue size in zebrafish. *Elife* **4**, e08201.

Alexander, J., Rothenberg, M., Henry, G. L. and Stainier, D. Y. (1999). casanova plays an early and essential role in endoderm formation in zebrafish. *Dev. Biol.* **215**, 343–357.

Bakkers, J. (2011). Zebrafish as a model to study cardiac development and human cardiac disease. *Cardiovasc. Res.* **91**, 279–288.

Bassat, E., Mutlak, Y. E., Genzelinakh, A., Shadrin, I. Y., Baruch Umansky, K., Yifa, O., Kain, D., Rajchman, D., Leach, J., Riabov Bassat, D., et al. (2017). The extracellular matrix protein agrin promotes heart regeneration in mice. *Nature* **547**, 179–184.

Benhamouche, S., Curto, M., Saotome, I., Gladden, A. B., Liu, C.-H., Giovannini, M. and McClatchey, A. I. (2010). Nf2/Merlin controls progenitor homeostasis and tumorigenesis in the liver. *Genes Dev.* **24**, 1718–1730.

Bergmann, O., Bhardwaj, R. D., Bernard, S., Zdunek, S., Barnabé-Heider, F., Walsh, S., Zupicich, J., Alkass, K., Buchholz, B. A., Druid, H., et al. (2009). Evidence for cardiomyocyte renewal in humans. *Science* **324**, 98–102.

Bersell, K., Arab, S., Haring, B. and Kühn, B. (2009). Neuregulin1/ErbB4 signaling induces cardiomyocyte proliferation and repair of heart injury. *Cell* **138**, 257–270.

Bossuyt, W., Chen, C.-L., Chen, Q., Sudol, M., McNeill, H., Pan, D., Kopp, A. and Halder, G. (2014). An evolutionary shift in the regulation of the Hippo pathway between mice and flies. *Oncogene* **33**, 1218–1228.

Botting, K. J., Wang, K. C. W., Padhee, M., McMillen, I. C., Summers-Pearce, B., Rattanatray, L., Cutri, N., Posterino, G. S., Brooks, D. A. and Morrison, J. L. (2012). Early origins of heart disease: low birth weight and determinants of cardiomyocyte endowment. *Clin. Exp. Pharmacol. Physiol.* **39**, 814–823.

Bussmann, J., Bos, F. L., Urasaki, A., Kawakami, K., Duckers, H. J. and Schulte-Merker, S. (2010). Arteries provide essential guidance cues for lymphatic endothelial cells in the zebrafish trunk. *Development* **137**, 2653–2657.

Cai, J., Zhang, N., Zheng, Y., de Wilde, R. F., Maitra, A. and Pan, D. (2010). The Hippo signaling pathway restricts the oncogenic potential of an intestinal regeneration program. *Genes Dev.* **24**, 2383–2388.

Cao, X., Pfaff, S. L. and Gage, F. H. (2008). YAP regulates neural progenitor cell number via the TEA domain transcription factor. *Genes Dev.* **22**, 3320–3334.

Cha, Y. R., Fujita, M., Butler, M., Isogai, S., Kochhan, E., Siekmann, A. F. and Weinstein, B. M. (2012). Chemokine signaling directs trunk lymphatic network formation along the preexisting blood vasculature. *Dev. Cell* **22**, 824–836.

Chen, J. N., Haffter, P., Odenthal, J., Vogelsang, E., Brand, M., van Eeden, F. J., Furutani-Seiki, M., Granato, M., Hammerschmidt, M., Heisenberg, C. P., et al. (1996).

Mutations affecting the cardiovascular system and other internal organs in zebrafish. *Development* **123**, 293–302.

Chen, H. I., Einbond, A., Kwak, S. J., Linn, H., Koepf, E., Peterson, S., Kelly, J. W. and Sudol, M. (1997). Characterization of the WW domain of human yes-associated protein and its polyproline-containing ligands. *J. Biol. Chem.* **272**, 17070–17077.

Chen, H., Shi, S., Acosta, L., Li, W., Lu, J., Bao, S., Chen, Z., Yang, Z., Schneider, M. D., Chien, K. R., et al. (2004). BMP10 is essential for maintaining cardiac growth during murine cardiogenesis. *Development* **131**, 2219–2231.

Chen, L., Chan, S. W., Zhang, X., Walsh, M., Lim, C. J., Hong, W. and Song, H. (2010). Structural basis of YAP recognition by TEAD4 in the hippo pathway. *Genes Dev.* **24**, 290–300.

Cherian, A. V., Fukuda, R., Augustine, S. M., Maischein, H.-M. and Stainier, D. Y. R. (2016). N-cadherin relocalization during cardiac trabeculation. *Proc. Natl. Acad. Sci. U. S. A.* **113**, 7569–7574.

Choi, W.-Y., Gemberling, M., Wang, J., Holdway, J. E., Shen, M.-C., Karlstrom, R. O. and Poss, K. D. (2013). In vivo monitoring of cardiomyocyte proliferation to identify chemical modifiers of heart regeneration. *Development* **140**, 660–666.

Chong, N. W., Koekemoer, A. L., Ounzain, S., Samani, N. J., Shin, J. T. and Shaw, S. Y. (2012). STARS Is Essential to Maintain Cardiac Development and Function In Vivo via a SRF Pathway. *PLoS One* **7**, e40966.

Clubb, F. J., Jr and Bishop, S. P. (1984). Formation of binucleated myocardial cells in the neonatal rat. An index for growth hypertrophy. *Lab. Invest.* **50**, 571–577.

Cox, A. G., Hwang, K. L., Brown, K. K., Evason, K., Beltz, S., Tsomides, A., O'Connor, K., Galli, G. G., Yimlamai, D., Chhangawala, S., et al. (2016). Yap reprograms glutamine metabolism to increase nucleotide biosynthesis and enable liver growth. *Nat. Cell Biol.* **18**, 886–896.

D'Amato, G., Luxán, G., del Monte-Nieto, G., Martínez-Poveda, B., Torroja, C., Walter, W., Bochter, M. S., Benedito, R., Cole, S., Martinez, F., et al. (2016). Sequential Notch activation regulates ventricular chamber development. *Nat. Cell Biol.* **18**, 7–20.

D'Amico, L., Scott, I. C., Jungblut, B. and Stainier, D. Y. R. (2007). A mutation in zebrafish hmgcr1b reveals a role for isoprenoids in vertebrate heart-tube formation. *Curr. Biol.* **17**, 252–259.

Davis, M. P. A., van Dongen, S., Abreu-Goodger, C., Bartonicek, N. and Enright, A. J. (2013). Kraken: a set of tools for quality control and analysis of high-throughput sequence data. *Methods* **63**, 41–49.

Dobin, A., Davis, C. A., Schlesinger, F., Drenkow, J., Zaleski, C., Jha, S., Batut, P., Chaisson, M. and Gingeras, T. R. (2013). STAR: ultrafast universal RNA-seq aligner. *Bioinformatics* **29**, 15–21.

Dray, N., Lawton, A., Nandi, A., Jülich, D., Emonet, T. and Holley, S. A. (2013). Cell-fibronectin interactions propel vertebrate trunk elongation via tissue mechanics. *Curr. Biol.*

23, 1335–1341.

Du, A., Sanger, J. M., Linask, K. K. and Sanger, J. W. (2003). Myofibrillogenesis in the first cardiomyocytes formed from isolated quail precardiac mesoderm. *Dev. Biol.* **257**, 382–394.

Dupont, S., Morsut, L., Aragona, M., Enzo, E., Giulitti, S., Cordenonsi, M., Zanconato, F., Le Digabel, J., Forcato, M., Bicciato, S., et al. (2011). Role of YAP/TAZ in mechanotransduction. *Nature* **474**, 179–183.

Ellertsdóttir, E., Lenard, A., Blum, Y., Krudewig, A., Herwig, L., Affolter, M. and Belting, H.-G. (2010). Vascular morphogenesis in the zebrafish embryo. *Dev. Biol.* **341**, 56–65.

Engler, A. J., Griffin, M. A., Sen, S., Bönnemann, C. G., Sweeney, H. L. and Discher, D. E. (2004). Myotubes differentiate optimally on substrates with tissue-like stiffness: pathological implications for soft or stiff microenvironments. *J. Cell Biol.* **166**, 877–887.

Ermekova, K. S., Zambrano, N., Linn, H., Minopoli, G., Gertler, F., Russo, T. and Sudol, M. (1997). The WW domain of neural protein FE65 interacts with proline-rich motifs in Mena, the mammalian homolog of Drosophila enabled. *J. Biol. Chem.* **272**, 32869–32877.

Esteves de Lima, J., Bonnin, M.-A., Birchmeier, C. and Duprez, D. (2016). Muscle contraction is required to maintain the pool of muscle progenitors via YAP and NOTCH during fetal myogenesis. *Elife* **5**,.

Fahed, A. C., Gelb, B. D., Seidman, J. G. and Seidman, C. E. (2013). Genetics of congenital heart disease: the glass half empty. *Circ. Res.* **112**, 707–720.

Fouquet, B., Weinstein, B. M., Serluca, F. C. and Fishman, M. C. (1997). Vessel patterning in the embryo of the zebrafish: guidance by notochord. *Dev. Biol.* **183**, 37–48.

Franco, C. A., Jones, M. L., Bernabeu, M. O., Geudens, I., Mathivet, T., Rosa, A., Lopes, F. M., Lima, A. P., Ragab, A., Collins, R. T., et al. (2015). Dynamic endothelial cell rearrangements drive developmental vessel regression. *PLoS Biol.* **13**, e1002125.

Franco, C. A., Jones, M. L., Bernabeu, M. O., Vion, A.-C., Barbacena, P., Fan, J., Mathivet, T., Fonseca, C. G., Ragab, A., Yamaguchi, T. P., et al. (2016). Non-canonical Wnt signalling modulates the endothelial shear stress flow sensor in vascular remodelling. *Elife* **5**, e07727.

Fukuda, R., Gunawan, F., Beisaw, A., Jimenez-Amilburu, V., Maischein, H.-M., Kostin, S., Kawakami, K. and Stainier, D. Y. R. (2017). Proteolysis regulates cardiomyocyte maturation and tissue integration. *Nat. Commun.* **8**, 14495.

Fukui, H., Terai, K., Nakajima, H., Chiba, A., Fukuhara, S. and Mochizuki, N. (2014). S1P-Yap1 signaling regulates endoderm formation required for cardiac precursor cell migration in zebrafish. *Dev. Cell* **31**, 128–136.

Ganem, N. J., Cornils, H., Chiu, S.-Y., O'Rourke, K. P., Arnaud, J., Yimlamai, D., Théry, M., Camargo, F. D. and Pellman, D. (2014). Cytokinesis failure triggers hippo tumor suppressor pathway activation. *Cell* **158**, 833–848.

García-Rivello, H., Taranda, J., Said, M., Cabeza-Meckert, P., Vila-Petroff, M.,

Scaglione, J., Ghio, S., Chen, J., Lai, C., Laguens, R. P., et al. (2005). Dilated cardiomyopathy in Erb-b4-deficient ventricular muscle. *Am. J. Physiol. Heart Circ. Physiol.* **289**, H1153–60.

Gassmann, M., Casagranda, F., Orioli, D., Simon, H., Lai, C., Klein, R. and Lemke, G. (1995). Aberrant neural and cardiac development in mice lacking the ErbB4 neuregulin receptor. *Nature* **378**, 390–394.

Gemberling, M., Karra, R., Dickson, A. L. and Poss, K. D. (2015). Nrg1 is an injury-induced cardiomyocyte mitogen for the endogenous heart regeneration program in zebrafish. *Elife* **4**,.

Genevet, A. and Tapon, N. (2011). The Hippo pathway and apico-basal cell polarity. *Biochem. J* **436**, 213–224.

Gilbert, R., Cohen, J. A., Pardo, S., Basu, A. and Fischman, D. A. (1999). Identification of the A-band localization domain of myosin binding proteins C and H (MyBP-C, MyBP-H) in skeletal muscle. *J. Cell Sci.* **112 (Pt 1)**, 69–79.

Grego-Bessa, J., Luna-Zurita, L., del Monte, G., Bolós, V., Melgar, P., Arandilla, A., Garratt, A. N., Zang, H., Mukouyama, Y.-S., Chen, H., et al. (2007). Notch signaling is essential for ventricular chamber development. *Dev. Cell* **12**, 415–429.

Haggie, P. M., Kim, J. K., Lukacs, G. L. and Verkman, A. S. (2006). Tracking of quantum dot-labeled CFTR shows near immobilization by C-terminal PDZ interactions. *Mol. Biol. Cell* **17**, 4937–4945.

Han, P., Bloomekatz, J., Ren, J., Zhang, R., Grinstein, J. D., Zhao, L., Burns, C. G., Burns, C. E., Anderson, R. M. and Chi, N. C. (2016). Coordinating cardiomyocyte interactions to direct ventricular chamber morphogenesis. *Nature* **534**, 700–704.

Hanahan, D. and Weinberg, R. A. (2011). Hallmarks of Cancer: The Next Generation. *Cell* **144**, 646–674.

Harris, B. Z. and Lim, W. A. (2001). Mechanism and role of PDZ domains in signaling complex assembly. *J. Cell Sci.* **114**, 3219–3231.

Haskins, J. W., Nguyen, D. X. and Stern, D. F. (2014). Neuregulin 1-activated ERBB4 interacts with YAP to induce Hippo pathway target genes and promote cell migration. *Sci. Signal.* **7**, ra116.

Heallen, T., Zhang, M., Wang, J., Bonilla-Claudio, M., Klysik, E., Johnson, R. L. and Martin, J. F. (2011). Hippo pathway inhibits Wnt signaling to restrain cardiomyocyte proliferation and heart size. *Science* **332**, 458–461.

Heallen, T., Morikawa, Y., Leach, J., Tao, G., Willerson, J. T., Johnson, R. L. and Martin, J. F. (2013). Hippo signaling impedes adult heart regeneration. *Development* **140**, 4683–4690.

Helker, C. S. M., Schuermann, A., Pollmann, C., Chng, S. C., Kiefer, F., Reversade, B. and Herzog, W. (2015). The hormonal peptide Elabela guides angioblasts to the midline during vasculogenesis. *Elife* **4**, e06726.

Hilman, D. and Gat, U. (2011). The evolutionary history of YAP and the hippo/YAP

pathway. *Mol. Biol. Evol.* **28**, 2403–2417.

Hogan, B. M., Bos, F. L., Bussmann, J., Witte, M., Chi, N. C., Duckers, H. J. and Schulte-Merker, S. (2009a). Ccbe1 is required for embryonic lymphangiogenesis and venous sprouting. *Nat. Genet.* **41**, 396–398.

Hogan, B. M., Herpers, R., Witte, M., Heloterä, H., Alitalo, K., Duckers, H. J. and Schulte-Merker, S. (2009b). Vegfc/Flt4 signalling is suppressed by Dll4 in developing zebrafish intersegmental arteries. *Development* **136**, 4001–4009.

Hossain, Z., Ali, S. M., Ko, H. L., Xu, J., Ng, C. P., Guo, K., Qi, Z., Ponniah, S., Hong, W. and Hunziker, W. (2007). Glomerulocystic kidney disease in mice with a targeted inactivation of Wwtr1. *Proc. Natl. Acad. Sci. U. S. A.* **104**, 1631–1636.

Huang, J., Wu, S., Barrera, J., Matthews, K. and Pan, D. (2005). The Hippo signaling pathway coordinately regulates cell proliferation and apoptosis by inactivating Yorkie, the Drosophila Homolog of YAP. *Cell* **122**, 421–434.

Huang, Y., Wang, X., Wang, X., Xu, M., Liu, M. and Liu, D. (2013). Nonmuscle myosin II-B (myh10) expression analysis during zebrafish embryonic development. *Gene Expr. Patterns* **13**, 265–270.

Isogai, S., Lawson, N. D., Torrealday, S., Horiguchi, M. and Weinstein, B. M. (2003). Angiogenic network formation in the developing vertebrate trunk. *Development* **130**, 5281–5290.

Jakobsson, L., Franco, C. A., Bentley, K., Collins, R. T., Ponsioen, B., Aspalter, I. M., Rosewell, I., Busse, M., Thurston, G., Medvinsky, A., et al. (2010). Endothelial cells dynamically compete for the tip cell position during angiogenic sprouting. *Nat. Cell Biol.* **12**, 943–953.

Jiménez-Amilburu, V., Rasouli, S. J., Staudt, D. W., Nakajima, H., Chiba, A., Mochizuki, N. and Stainier, D. Y. R. (2016). In Vivo Visualization of Cardiomyocyte Apicobasal Polarity Reveals Epithelial to Mesenchymal-like Transition during Cardiac Trabeculation. *Cell Rep.* **17**, 2687–2699.

Jin, S.-W., Beis, D., Mitchell, T., Chen, J.-N. and Stainier, D. Y. R. (2005). Cellular and molecular analyses of vascular tube and lumen formation in zebrafish. *Development* **132**, 5199–5209.

Johnson, R. and Halder, G. (2014). The two faces of Hippo: targeting the Hippo pathway for regenerative medicine and cancer treatment. *Nat. Rev. Drug Discov.* **13**, 63–79.

Kaan, H. Y. K., Chan, S. W., Tan, S. K. J., Guo, F., Lim, C. J., Hong, W. and Song, H. (2017). Crystal structure of TAZ-TEAD complex reveals a distinct interaction mode from that of YAP-TEAD complex. *Sci. Rep.* **7**, 2035.

Kanai, F., Marignani, P. A., Sarbassova, D., Yagi, R., Hall, R. A., Donowitz, M., Hisaminato, A., Fujiwara, T., Ito, Y., Cantley, L. C., et al. (2000). TAZ: a novel transcriptional co-activator regulated by interactions with 14-3-3 and PDZ domain proteins. *EMBO J.* **19**, 6778–6791.

Keegan, B. R., Meyer, D. and Yelon, D. (2004). Organization of cardiac chamber

progenitors in the zebrafish blastula. *Development* **131**, 3081–3091.

Kim, J. H., Lee, S.-R., Li, L.-H., Park, H.-J., Park, J.-H., Lee, K. Y., Kim, M.-K., Shin, B. A. and Choi, S.-Y. (2011). High cleavage efficiency of a 2A peptide derived from porcine teschovirus-1 in human cell lines, zebrafish and mice. *PLoS One* **6**, e18556.

Kim, J., Kim, Y. H., Kim, J., Park, D. Y., Bae, H., Lee, D.-H., Kim, K. H., Hong, S. P., Jang, S. P., Kubota, Y., et al. (2017). YAP/TAZ regulates sprouting angiogenesis and vascular barrier maturation. *J. Clin. Invest.* **127**, 3441–3461.

Kohli, V., Schumacher, J. A., Desai, S. P., Rehn, K. and Sumanas, S. (2013). Arterial and venous progenitors of the major axial vessels originate at distinct locations. *Dev. Cell* **25**, 196–206.

Komuro, A., Nagai, M., Navin, N. E. and Sudol, M. (2003). WW domain-containing protein YAP associates with ErbB-4 and acts as a co-transcriptional activator for the carboxyl-terminal fragment of ErbB-4 that translocates to the nucleus. *J. Biol. Chem.* **278**, 33334–33341.

Kwon, H.-B., Wang, S., Helker, C. S. M., Rasouli, S. J., Maischein, H.-M., Offermanns, S., Herzog, W. and Stainier, D. Y. R. (2016). In vivo modulation of endothelial polarization by Apelin receptor signalling. *Nat. Commun.* **7**, 11805.

Lauter, G., Söll, I. and Hauptmann, G. (2014). Sensitive whole-mount fluorescent in situ hybridization in zebrafish using enhanced tyramide signal amplification. *Methods Mol. Biol.* **1082**, 175–185.

Lawson, N. D. and Weinstein, B. M. (2002). In vivo imaging of embryonic vascular development using transgenic zebrafish. *Dev. Biol.* **248**, 307–318.

Lawson, N. D., Vogel, A. M. and Weinstein, B. M. (2002). sonic hedgehog and vascular endothelial growth factor act upstream of the Notch pathway during arterial endothelial differentiation. *Dev. Cell* **3**, 127–136.

Lee, K. F., Simon, H., Chen, H., Bates, B., Hung, M. C. and Hauser, C. (1995). Requirement for neuregulin receptor erbB2 in neural and cardiac development. *Nature* **378**, 394–398.

Lee, J. S., Yu, Q., Shin, J. T., Sebzda, E., Bertozzi, C., Chen, M., Mericko, P., Stadtfeld, M., Zhou, D., Cheng, L., et al. (2006). Klf2 is an essential regulator of vascular hemodynamic forces in vivo. *Dev. Cell* **11**, 845–857.

Lee, K.-P., Lee, J.-H., Kim, T.-S., Kim, T.-H., Park, H.-D., Byun, J.-S., Kim, M.-C., Jeong, W.-I., Calvisi, D. F., Kim, J.-M., et al. (2010). The Hippo-Salvador pathway restrains hepatic oval cell proliferation, liver size, and liver tumorigenesis. *Proc. Natl. Acad. Sci. U. S. A.* **107**, 8248–8253.

Le Guen, L., Karpanen, T., Schulte, D., Harris, N. C., Koltowska, K., Roukens, G., Bower, N. I., van Impel, A., Stacker, S. A., Achen, M. G., et al. (2014). Ccbe1 regulates Vegfc-mediated induction of Vegfr3 signaling during embryonic lymphangiogenesis. *Development* **141**, 1239–1249.

Li, Y., Klena, N. T., Gabriel, G. C., Liu, X., Kim, A. J., Lemke, K., Chen, Y., Chatterjee,

B., Devine, W., Damerla, R. R., et al. (2015). Global genetic analysis in mice unveils central role for cilia in congenital heart disease. *Nature* **521**, 520–524.

Liao, Y., Smyth, G. K. and Shi, W. (2014). featureCounts: an efficient general purpose program for assigning sequence reads to genomic features. *Bioinformatics* **30**, 923–930.

Lin, Y.-F., Swinburne, I. and Yelon, D. (2012). Multiple influences of blood flow on cardiomyocyte hypertrophy in the embryonic zebrafish heart. *Dev. Biol.* **362**, 242–253.

Linn, H., Ermekova, K. S., Rentschler, S., Sparks, A. B., Kay, B. K. and Sudol, M. (1997). Using molecular repertoires to identify high-affinity peptide ligands of the WW domain of human and mouse YAP. *Biol. Chem.* **378**, 531–537.

Liu, J., Bressan, M., Hassel, D., Huisken, J., Staudt, D., Kikuchi, K., Poss, K. D., Mikawa, T. and Stainier, D. Y. R. (2010). A dual role for ErbB2 signaling in cardiac trabeculation. *Development* **137**, 3867–3875.

Love, M. I., Huber, W. and Anders, S. (2014). Moderated estimation of fold change and dispersion for RNA-seq data with DESeq2. *Genome Biol.* **15**, 550.

Lu, L., Li, Y., Kim, S. M., Bossuyt, W., Liu, P., Qiu, Q., Wang, Y., Halder, G., Finegold, M. J., Lee, J.-S., et al. (2010). Hippo signaling is a potent in vivo growth and tumor suppressor pathway in the mammalian liver. *Proc. Natl. Acad. Sci. U. S. A.* **107**, 1437–1442.

Lubs, H., Abidi, F. E., Echeverri, R., Holloway, L., Meindl, A., Stevenson, R. E. and Schwartz, C. E. (2006). Golabi-Ito-Hall syndrome results from a missense mutation in the WW domain of the PQBP1 gene. *J. Med. Genet.* **43**, e30.

Ma, X., Takeda, K., Singh, A., Yu, Z.-X., Zerfas, P., Blount, A., Liu, C., Towbin, J. A., Schneider, M. D., Adelstein, R. S., et al. (2009). Conditional ablation of nonmuscle myosin II-B delineates heart defects in adult mice. *Circ. Res.* **105**, 1102–1109.

Manderfield, L. J., Aghajanian, H., Engleka, K. A., Lim, L. Y., Liu, F., Jain, R., Li, L., Olson, E. N. and Epstein, J. A. (2015). Hippo signaling is required for Notch-dependent smooth muscle differentiation of neural crest. *Development* **142**, 2962–2971.

Matz, D. G., Oberpriller, J. O. and Oberpriller, J. C. (1998). Comparison of mitosis in binucleated and mononucleated newt cardiac myocytes. *Anat. Rec.* **251**, 245–255.

McMillen, P. and Holley, S. A. (2015). Integration of cell-cell and cell-ECM adhesion in vertebrate morphogenesis. *Curr. Opin. Cell Biol.* **36**, 48–53.

Meyer, D. and Birchmeier, C. (1995). Multiple essential functions of neuregulin in development. *Nature* **378**, 386–390.

Miesfeld, J. B., Gestri, G., Clark, B. S., Flinn, M. A., Poole, R. J., Bader, J. R., Besharse, J. C., Wilson, S. W. and Link, B. A. (2015). Yap and Taz regulate retinal pigment epithelial cell fate. *Development* **142**, 3021–3032.

Mo, F.-E., Muntean, A. G., Chen, C.-C., Stolz, D. B., Watkins, S. C. and Lau, L. F. (2002). CYR61 (CCN1) is essential for placental development and vascular integrity. *Mol. Cell. Biol.* **22**, 8709–8720.

Morikawa, Y., Zhang, M., Heallen, T., Leach, J., Tao, G., Xiao, Y., Bai, Y., Li, W.,

Willerson, J. T. and Martin, J. F. (2015). Actin cytoskeletal remodeling with protrusion formation is essential for heart regeneration in Hippo-deficient mice. *Sci. Signal.* **8**, ra41.

Morikawa, Y., Heallen, T., Leach, J., Xiao, Y. and Martin, J. F. (2017). Dystrophin-glycoprotein complex sequesters Yap to inhibit cardiomyocyte proliferation. *Nature* **547**, 227–231.

Morin-Kensicki, E. M., Boone, B. N., Howell, M., Stonebraker, J. R., Teed, J., Alb, J. G., Magnuson, T. R., O'Neal, W. and Milgram, S. L. (2006). Defects in yolk sac vasculogenesis, chorioallantoic fusion, and embryonic axis elongation in mice with targeted disruption of Yap65. *Mol. Cell. Biol.* **26**, 77–87.

Nakajima, H., Yamamoto, K., Agarwala, S., Terai, K., Fukui, H., Fukuhara, S., Ando, K., Miyazaki, T., Yokota, Y., Schmelzer, E., et al. (2017). Flow-Dependent Endothelial YAP Regulation Contributes to Vessel Maintenance. *Dev. Cell* **40**, 523–536.e6.

Naqvi, N., Li, M., Calvert, J. W., Tejada, T., Lambert, J. P., Wu, J., Kesteven, S. H., Holman, S. R., Matsuda, T., Lovelock, J. D., et al. (2014). A proliferative burst during preadolescence establishes the final cardiomyocyte number. *Cell* **157**, 795–807.

Nasevicius, A., Larson, J. and Ekker, S. C. (2000). Distinct requirements for zebrafish angiogenesis revealed by a VEGF-A morphant. *Yeast* **17**, 294–301.

Nicenboim, J., Malkinson, G., Lupo, T., Asaf, L., Sela, Y., Mayseless, O., Gibbs-Bar, L., Senderovich, N., Hashimshony, T., Shin, M., et al. (2015). Lymphatic vessels arise from specialized angioblasts within a venous niche. *Nature* **522**, 56–61.

Nicoli, S., Standley, C., Walker, P., Hurlstone, A., Fogarty, K. E. and Lawson, N. D. (2010). MicroRNA-mediated integration of haemodynamics and Vegf signalling during angiogenesis. *Nature* **464**, 1196–1200.

Ninov, N., Borius, M. and Stainier, D. Y. R. (2012). Different levels of Notch signaling regulate quiescence, renewal and differentiation in pancreatic endocrine progenitors. *Development* **139**, 1557–1567.

Nishimura, T., Ito, S., Saito, H., Hiver, S., Shigetomi, K., Ikenouchi, J. and Takeichi, M. (2016). DAAM1 stabilizes epithelial junctions by restraining WAVE complex-dependent lateral membrane motility. *J. Cell Biol.* **215**, 559–573.

Nishioka, N., Inoue, K.-I., Adachi, K., Kiyonari, H., Ota, M., Ralston, A., Yabuta, N., Hirahara, S., Stephenson, R. O., Ogonuki, N., et al. (2009). The Hippo signaling pathway components Lats and Yap pattern Tead4 activity to distinguish mouse trophectoderm from inner cell mass. *Dev. Cell* **16**, 398–410.

Noël, E. S., Verhoeven, M., Lagendijk, A. K., Tessadori, F., Smith, K., Choorapoikayil, S., den Hertog, J. and Bakkers, J. (2013). A Nodal-independent and tissue-intrinsic mechanism controls heart-looping chirality. *Nat. Commun.* **4**, 2754.

Oberpriller, J. O., Oberpriller, J. C., Arefyeva, A. M., Mitashov, V. I. and Carlson, B. M. (1988). Nuclear characteristics of cardiac myocytes following the proliferative response to mincing of the myocardium in the adult newt, Notophthalmus viridescens. *Cell Tissue Res.* **253**, 619–624.

Oka, T. and Sudol, M. (2009). Nuclear localization and pro-apoptotic signaling of YAP2 require intact PDZ-binding motif. *Genes Cells* **14**, 607–615.

Oka, T., Remue, E., Meerschaert, K., Vanloo, B., Boucherie, C., Gfeller, D., Bader, G. D., Sidhu, S. S., Vandekerckhove, J., Gettemans, J., et al. (2010). Functional complexes between YAP2 and ZO-2 are PDZ domain-dependent, and regulate YAP2 nuclear localization and signalling. *Biochem. J* **432**, 461–472.

Okuda, K. S., Astin, J. W., Misa, J. P., Flores, M. V., Crosier, K. E. and Crosier, P. S. (2012). lyve1 expression reveals novel lymphatic vessels and new mechanisms for lymphatic vessel development in zebrafish. *Development* **139**, 2381–2391.

Ozcelik, C., Erdmann, B., Pilz, B., Wettschureck, N., Britsch, S., Hübner, N., Chien, K. R., Birchmeier, C. and Garratt, A. N. (2002). Conditional mutation of the ErbB2 (HER2) receptor in cardiomyocytes leads to dilated cardiomyopathy. *Proc. Natl. Acad. Sci. U. S. A.* **99**, 8880–8885.

Peshkovsky, C., Totong, R. and Yelon, D. (2011). Dependence of cardiac trabeculation on neuregulin signaling and blood flow in zebrafish. *Dev. Dyn.* **240**, 446–456.

Pestel, J., Ramadass, R., Gauvrit, S., Helker, C., Herzog, W. and Stainier, D. Y. R. (2016). Real-time 3D visualization of cellular rearrangements during cardiac valve formation. *Development* **143**, 2217–2227.

Polizzotti, B. D., Ganapathy, B., Walsh, S., Choudhury, S., Ammanamanchi, N., Bennett, D. G., dos Remedios, C. G., Haubner, B. J., Penninger, J. M. and Kühn, B. (2015). Neuregulin stimulation of cardiomyocyte regeneration in mice and human myocardium reveals a therapeutic window. *Sci. Transl. Med.* **7**, 281ra45.

Porazinski, S., Wang, H., Asaoka, Y., Behrndt, M., Miyamoto, T., Morita, H., Hata, S., Sasaki, T., Gabriel Krens, S. F., Osada, Y., et al. (2015). YAP is essential for tissue tension to ensure vertebrate 3D body shape. *Nature* **521**, 217–221.

Porrello, E. R. and Olson, E. N. (2014). A neonatal blueprint for cardiac regeneration. *Stem Cell Res.* **13**, 556–570.

Poss, K. D., Wilson, L. G. and Keating, M. T. (2002). Heart regeneration in zebrafish. *Science* **298**, 2188–2190.

Proulx, K., Lu, A. and Sumanas, S. (2010). Cranial vasculature in zebrafish forms by angioblast cluster-derived angiogenesis. *Dev. Biol.* **348**, 34–46.

Rasouli, S. J. and Stainier, D. Y. R. (2017). Regulation of cardiomyocyte behavior in zebrafish trabeculation by Neuregulin 2a signaling. *Nat. Commun.* **8**, 15281.

Reginensi, A., Hoshi, M., Boualia, S. K., Bouchard, M., Jain, S. and McNeill, H. (2015). Yap and Taz are required for Ret-dependent urinary tract morphogenesis. *Development* **142**, 2696–2703.

Reginensi, A., Enderle, L., Gregorieff, A., Johnson, R. L., Wrana, J. L. and McNeill, H. (2016). A critical role for NF2 and the Hippo pathway in branching morphogenesis. *Nat. Commun.* **7**, 12309.

Reischauer, S., Arnaout, R., Ramadass, R. and Stainier, D. Y. R. (2014). Actin binding

GFP allows 4D in vivo imaging of myofilament dynamics in the zebrafish heart and the identification of Erbb2 signaling as a remodeling factor of myofibril architecture. *Circ. Res.* **115**, 845–856.

Revenu, C., Streichan, S., Donà, E., Lecaudey, V., Hufnagel, L. and Gilmour, D. (2014). Quantitative cell polarity imaging defines leader-to-follower transitions during collective migration and the key role of microtubule-dependent adherens junction formation. *Development* **141**, 1282–1291.

Rosenthal, N. and Harvey, R. P. (2010). *Heart Development and Regeneration*. Academic Press.

Rossi, A., Gauvrit, S., Marass, M., Pan, L., Moens, C. B. and Stainier, D. Y. R. (2016). Regulation of Vegf signaling by natural and synthetic ligands. *Blood* **128**, 2359–2366.

Rottbauer, W., Saurin, A. J., Lickert, H., Shen, X., Burns, C. G., Wo, Z. G., Kemler, R., Kingston, R., Wu, C. and Fishman, M. (2002). Reptin and pontin antagonistically regulate heart growth in zebrafish embryos. *Cell* **111**, 661–672.

Ryan, J. M. (1979). Effect of different fetal bovine serum concentrations on the replicative life span of cultured chick cells. *In Vitro* **15**, 895–899.

Sabine, A., Bovay, E., Demir, C. S., Kimura, W., Jaquet, M., Agalarov, Y., Zangger, N., Scallan, J. P., Graber, W., Gulpinar, E., et al. (2015). FOXC2 and fluid shear stress stabilize postnatal lymphatic vasculature. *J. Clin. Invest.* **125**, 3861–3877.

Samsa, L. A., Givens, C., Tzima, E., Stainier, D. Y. R., Qian, L. and Liu, J. (2015). Cardiac contraction activates endocardial Notch signaling to modulate chamber maturation in zebrafish. *Development* **142**, 4080–4091.

Schindelin, J., Arganda-Carreras, I., Frise, E., Kaynig, V., Longair, M., Pietzsch, T., Preibisch, S., Rueden, C., Saalfeld, S., Schmid, B., et al. (2012). Fiji: an open-source platform for biological-image analysis. *Nat. Methods* **9**, 676–682.

Schlegelmilch, K., Mohseni, M., Kirak, O., Pruszak, J., Rodriguez, J. R., Zhou, D., Kreger, B. T., Vasioukhin, V., Avruch, J., Brummelkamp, T. R., et al. (2011). Yap1 acts downstream of α-catenin to control epidermal proliferation. *Cell* **144**, 782–795.

Sedmera, D., Pexieder, T., Vuillemin, M., Thompson, R. P. and Anderson, R. H. (2000). Developmental patterning of the myocardium. *Anat. Rec.* **258**, 319–337.

Siekmann, A. F. and Lawson, N. D. (2007). Notch signalling limits angiogenic cell behaviour in developing zebrafish arteries. *Nature* **445**, 781–784.

Soonpaa, M. H., Kim, K. K., Pajak, L., Franklin, M. and Field, L. J. (1996). Cardiomyocyte DNA synthesis and binucleation during murine development. *Am. J. Physiol.* **271**, H2183–9.

Sparrow, J. C. and Schöck, F. (2009). The initial steps of myofibril assembly: integrins pave the way. *Nat. Rev. Mol. Cell Biol.* **10**, 293–298.

Stainier, D. Y. (2001). Zebrafish genetics and vertebrate heart formation. *Nat. Rev. Genet.* **2**, 39–48.

Stainier, D. Y., Fouquet, B., Chen, J. N., Warren, K. S., Weinstein, B. M., Meiler, S. E., Mohideen, M. A., Neuhauss, S. C., Solnica-Krezel, L., Schier, A. F., et al. (1996). Mutations affecting the formation and function of the cardiovascular system in the zebrafish embryo. *Development* **123**, 285–292.

Staudt, D. and Stainier, D. (2012). Uncovering the molecular and cellular mechanisms of heart development using the zebrafish. *Annu. Rev. Genet.* **46**, 397–418.

Staudt, D. W., Liu, J., Thorn, K. S., Stuurman, N., Liebling, M. and Stainier, D. Y. R. (2014). High-resolution imaging of cardiomyocyte behavior reveals two distinct steps in ventricular trabeculation. *Development* **141**, 585–593.

Sudol, M. and Harvey, K. F. (2010). Modularity in the Hippo signaling pathway. *Trends Biochem. Sci.* **35**, 627–633.

Sumoy, L., Keasey, J. B., Dittman, T. D. and Kimelman, D. (1997). A role for notochord in axial vascular development revealed by analysis of phenotype and the expression of VEGR-2 in zebrafish flh and ntl mutant embryos. *Mech. Dev.* **63**, 15–27.

Taniguchi, K., Wu, L.-W., Grivennikov, S. I., de Jong, P. R., Lian, I., Yu, F.-X., Wang, K., Ho, S. B., Boland, B. S., Chang, J. T., et al. (2015). A gp130–Src–YAP module links inflammation to epithelial regeneration. *Nature* **519**, 57–62.

Thisse, C. and Thisse, B. (2008). High-resolution in situ hybridization to whole-mount zebrafish embryos. *Nat. Protoc.* **3**, 59–69.

Tullio, A. N., Accili, D., Ferrans, V. J., Yu, Z. X., Takeda, K., Grinberg, A., Westphal, H., Preston, Y. A. and Adelstein, R. S. (1997). Nonmuscle myosin II-B is required for normal development of the mouse heart. *Proc. Natl. Acad. Sci. U. S. A.* **94**, 12407–12412.

Varelas, X., Samavarchi-Tehrani, P., Narimatsu, M., Weiss, A., Cockburn, K., Larsen, B. G., Rossant, J. and Wrana, J. L. (2010). The Crumbs complex couples cell density sensing to Hippo-dependent control of the TGF-β-SMAD pathway. *Dev. Cell* **19**, 831–844.

Vassilev, A., Kaneko, K. J., Shu, H., Zhao, Y. and DePamphilis, M. L. (2001). TEAD/TEF transcription factors utilize the activation domain of YAP65, a Src/Yes-associated protein localized in the cytoplasm. *Genes Dev.* **15**, 1229–1241.

Verma, S., Han, S. P., Michael, M., Gomez, G. A., Yang, Z., Teasdale, R. D., Ratheesh, A., Kovacs, E. M., Ali, R. G. and Yap, A. S. (2012). A WAVE2-Arp2/3 actin nucleator apparatus supports junctional tension at the epithelial zonula adherens. *Mol. Biol. Cell* **23**, 4601–4610.

Vincent, M. D. (2010). The animal within: carcinogenesis and the clonal evolution of cancer cells are speciation events sensu stricto. *Evolution* **64**, 1173–1183.

Vivien, C. J., Hudson, J. E. and Porrello, E. R. (2016). Evolution, comparative biology and ontogeny of vertebrate heart regeneration. *npj Regenerative Medicine* **1**,.

von Gise, A., Lin, Z., Schlegelmilch, K., Honor, L. B., Pan, G. M., Buck, J. N., Ma, Q., Ishiwata, T., Zhou, B., Camargo, F. D., et al. (2012). YAP1, the nuclear target of Hippo signaling, stimulates heart growth through cardiomyocyte proliferation but not hypertrophy. *Proc. Natl. Acad. Sci. U. S. A.* **109**, 2394–2399.

Wang, K.-C., Yeh, Y.-T., Nguyen, P., Limqueco, E., Lopez, J., Thorossian, S., Guan, K.-L., Li, Y.-S. J. and Chien, S. (2016). Flow-dependent YAP/TAZ activities regulate endothelial phenotypes and atherosclerosis. *Proc. Natl. Acad. Sci. U. S. A.* **113**, 11525–11530.

Wang, X., Freire Valls, A., Schermann, G., Shen, Y., Moya, I. M., Castro, L., Urban, S., Solecki, G. M., Winkler, F., Riedemann, L., et al. (2017). YAP/TAZ Orchestrate VEGF Signaling during Developmental Angiogenesis. *Dev. Cell* **42**, 462–478.e7.

Welikson, R. E. and Fischman, D. A. (2002). The C-terminal IgI domains of myosin-binding proteins C and H (MyBP-C and MyBP-H) are both necessary and sufficient for the intracellular crosslinking of sarcomeric myosin in transfected non-muscle cells. *J. Cell Sci.* **115**, 3517–3526.

Wenink, A. C., Knaapen, M. W., Vrolijk, B. C. and VanGroningen, J. P. (1996). Development of myocardial fiber organization in the rat heart. *Anat. Embryol.* **193**, 559–567.

Wickham, H. (2010). *ggplot2: Elegant Graphics for Data Analysis*. Springer New York.

Williamson, K. A., Rainger, J., Floyd, J. A. B., Ansari, M., Meynert, A., Aldridge, K. V., Rainger, J. K., Anderson, C. A., Moore, A. T., Hurles, M. E., et al. (2014). Heterozygous loss-of-function mutations in YAP1 cause both isolated and syndromic optic fissure closure defects. *Am. J. Hum. Genet.* **94**, 295–302.

Wills, A. A., Holdway, J. E., Major, R. J. and Poss, K. D. (2008). Regulated addition of new myocardial and epicardial cells fosters homeostatic cardiac growth and maintenance in adult zebrafish. *Development* **135**, 183–192.

Wu, S., Huang, J., Dong, J. and Pan, D. (2003). hippo encodes a Ste-20 family protein kinase that restricts cell proliferation and promotes apoptosis in conjunction with salvador and warts. *Cell* **114**, 445–456.

Xin, M., Kim, Y., Sutherland, L. B., Qi, X., McAnally, J., Schwartz, R. J., Richardson, J. A., Bassel-Duby, R. and Olson, E. N. (2011). Regulation of insulin-like growth factor signaling by Yap governs cardiomyocyte proliferation and embryonic heart size. *Sci. Signal.* **4**, ra70.

Xin, M., Kim, Y., Sutherland, L. B., Murakami, M., Qi, X., McAnally, J., Porrello, E. R., Mahmoud, A. I., Tan, W., Shelton, J. M., et al. (2013). Hippo pathway effector Yap promotes cardiac regeneration. *Proc. Natl. Acad. Sci. U. S. A.* **110**, 13839–13844.

Yaniv, K., Isogai, S., Castranova, D., Dye, L., Hitomi, J. and Weinstein, B. M. (2006). Live imaging of lymphatic development in the zebrafish. *Nat. Med.* **12**, 711–716.

Yu, F.-X. and Guan, K.-L. (2013). The Hippo pathway: regulators and regulations. *Genes Dev.* **27**, 355–371.

Yu, F.-X., Zhao, B., Panupinthu, N., Jewell, J. L., Lian, I., Wang, L. H., Zhao, J., Yuan, H., Tumaneng, K., Li, H., et al. (2012). Regulation of the Hippo-YAP pathway by G-protein-coupled receptor signaling. *Cell* **150**, 780–791.

Zanconato, F., Forcato, M., Battilana, G., Azzolin, L., Quaranta, E., Bodega, B., Rosato, A., Bicciato, S., Cordenonsi, M. and Piccolo, S. (2015). Genome-wide association between YAP/TAZ/TEAD and AP-1 at enhancers drives oncogenic growth. *Nat. Cell Biol.* **17**, 1218–

1227.

Zemrak, F., Ahlman, M. A., Captur, G., Mohiddin, S. A., Kawel-Boehm, N., Prince, M. R., Moon, J. C., Hundley, W. G., Lima, J. A. C., Bluemke, D. A., et al. (2014). The relationship of left ventricular trabeculation to ventricular function and structure over a 9.5-year follow-up: the MESA study. *J. Am. Coll. Cardiol.* **64**, 1971–1980.

Zhang, N., Bai, H., David, K. K., Dong, J., Zheng, Y., Cai, J., Giovannini, M., Liu, P., Anders, R. A. and Pan, D. (2010). The Merlin/NF2 tumor suppressor functions through the YAP oncoprotein to regulate tissue homeostasis in mammals. *Dev. Cell* **19**, 27–38.

Zhao, B., Wei, X., Li, W., Udan, R. S., Yang, Q., Kim, J., Xie, J., Ikenoue, T., Yu, J., Li, L., et al. (2007). Inactivation of YAP oncoprotein by the Hippo pathway is involved in cell contact inhibition and tissue growth control. *Genes Dev.* **21**, 2747–2761.

Zhao, B., Ye, X., Yu, J., Li, L., Li, W., Li, S., Yu, J., Lin, J. D., Wang, C.-Y., Chinnaiyan, A. M., et al. (2008). TEAD mediates YAP-dependent gene induction and growth control. *Genes Dev.* **22**, 1962–1971.

Zhao, B., Li, L., Tumaneng, K., Wang, C.-Y. and Guan, K.-L. (2010). A coordinated phosphorylation by Lats and CK1 regulates YAP stability through SCF(beta-TRCP). *Genes Dev.* **24**, 72–85.

Zhou, D., Conrad, C., Xia, F., Park, J.-S., Payer, B., Yin, Y., Lauwers, G. Y., Thasler, W., Lee, J. T., Avruch, J., et al. (2009). Mst1 and Mst2 maintain hepatocyte quiescence and suppress hepatocellular carcinoma development through inactivation of the Yap1 oncogene. *Cancer Cell* **16**, 425–438.

10.   ACKNOWLEDGEMENTS

I would like to first and foremost thank my family: Lai Tek Chai, Ong Ching Goh, Lai Pik Yien, and Samuel Lai, for their support and sacrifices that have made this pursuit in science possible. I am indebted to my parents' sacrifices which provided my siblings and me a good education and a good life. To my dad, who is always fascinated by scientific discoveries (he is more advanced than I am, technologically speaking), for encouraging me to be a student of the sciences.

I am thankful to Didier Stainier, who has graciously accepted to train me as a doctoral candidate. Although a challenging project, his careful guidance and supervision have allowed me to push the boundaries. I have also benefitted immensely from his vast connections to various trendsetters in the field, which has produced many fruitful collaborations and discoveries about the Hippo pathway and cardiovascular development.

To the many fish that were sacrificed for this project and for the advancement of knowledge, I owe them for their unspoken courage and unwillful choice to be born in a lab. I can only hope that their sacrifices will be paid off by the impact of this work, small or big.

My warmest thanks go to Virginie Lecaudey, for graciously accepting to review this thesis. And to Stefan Liebner, who has taken the effort every year to attend and be a source of guidance and encouragement during my Thesis Advisory Committee (TAC) meetings. I am also thankful to Bilge Reischauer for taking care of the PhD students in MPI Bad Nauheim; also to Sharon Meaney-Gardian and Sabine Fischer for the assistance over the countless administrative matters in the institute.

I would like to acknowledge colleagues who have been instrumental in the synergistic creativity in the work mentioned here or otherwise. To Hans-Martin Maischein, the transplantation master, through whom I came to know that medaka-zebrafish hybrids were possible, leading to the oddest experiments I have thought of and performed. To Ben Lai, who was curious and willing to help me pursue my Zedaka (zebrafish-medaka) vision, by first showing that in principle, isolated cardiomyocytes can be grafted into adult zebrafish hearts. To Sven Reischauer, Oliver Stone, Mike Housley and Markus Bussen who are immensely interested in the abstract questions of Biology, who have given me invaluable ideas and

11. CURRICULUM VITAE

Full Name: Jason LAI Kuan Han

Address: Benekestrasse 13, 61231 Bad Nauheim, Germany.

Contact number: +49-(0)6032 705-1333

E-mail: jason.lai@mpi-bn.mpg.de

EDUCATION

Feb 2014 – present	**Max Planck Institute for Heart and Lung Research, Bad Nauheim, Germany; Goethe University, Frankfurt, Germany**
	Ph.D. Biological Sciences
Aug 2008 – Jun 2012	**National University of Singapore (NUS), Singapore**
	B. Sc. (Hons.) Life Sciences and Statistics (minor) (CAP 4.13/5.00)
Jan 2011 – Jun 2011	**University of California, Berkeley, California, USA**
	Education Abroad Program (Semester GPA 3.42/4.00)

RESEARCH

Feb 2014 - Current	**Stainier Lab**, Max Planck Institute for Heart and Lung Research, Bad Nauheim, Germany
	Functional Investigation of the Hippo Transducers Yap/Taz in Cardiovascular Development.
	Ph.D. Thesis
	Supervisor: Dr. Didier Stainier
Jun 2011 – Jun 2012	**Wang Lab**, Department of Biochemistry, NUS, Singapore
	Reprogramming of Lung Cancer Cells Abrogates Aberrant Cancer Methylome and Transcriptome.
	Honors Thesis
	Supervisors: Dr. Henry Yang and Dr. Wang Xueying
Jan 2010 – Dec 2010	**Chu Lab**, Department of Microbiology, NUS, Singapore
	Identifying Putative Receptor-Binding Domain(s) on Chikungunya Virus (CHIKV) E2 Protein.
	Undergraduate Research Opportunities Programme in Science
	Supervisor: Dr. Justin Chu

EMPLOYMENT

Jul 2012 – Jan 2014	**Saw Swee Hock School of Public Health, NUS, Singapore**
	Research Assistant
	Supervisor: A/P Yik Ying Teo

PUBLICATIONS

Lai, S.-L., Marín-Juez, R., Moura, P., Kuenne, C., **Lai, J. K. H.**, Tsedeke, A. T., Guenther, S., Looso, M. & Stainier, D. Y. R. (2017). Reciprocal analyses in zebrafish and medaka reveal that harnessing the immune response promotes cardiac regeneration. *eLife*.

Lai, J. K. H. & Stainier, D. Y. R. (2017). Pushing Yap into the nucleus with shear force. *Dev. Cell*, 40(6), 517-518.

Wong, L.-P., **Lai, J. K.-H.**, Saw, W.-Y., Ong, R. T.-H., Cheng, A. Y., Pillai, N. E., … Teo, Y.-Y. (2014). Insights into the Genetic Structure and Diversity of 38 South Asian Indians from Deep Whole-Genome Sequencing. *PLoS Genetics*, 10(5), e1004377.

Lai, J., Kong, C. M., Mahalingam, D., Xie, X. & Wang, X. (2013). Elite Model for the Generation of Induced Pluripotent Cancer Cells (iPC). *PLoS ONE* 8(2): e56702.

Mahalingam, D, Kong, C. M., **Lai, J.**, Tay, L. L., Yang, H. & Wang, X. (2012). Reversal of Aberrant Cancer Methylome and Transcriptome upon Direct Reprogramming of Lung Cancer Cells. *Sci Rep.***2**, 592.

ARTICLES IN PREPARATION

Kimelman, D., Smith, N. L., **Lai, J. K. H.** & Stainier, D. Y. R. (under review). Regulation of posterior body and ectodermal morphogenesis in zebrafish by localized Yap1 and Wwtr1 (Taz). *eLife.*

Stone, O., El-Brolosy, M., Wilhelm, K., Liu X., Romão, A., Grillo, E., **Lai, J. K. H.**, Günther, S., Jeratsch, S., Lee, I-C., Braun, T., Santoro, M., Locasale, J., Potente, M., Stainier, D. Y. R. (submitted). Loss of pyruvate kinase M2 limits growth and triggers viral mimicry in endothelial cells. *Nat. Comm.*

Lai, J. K. H., Collins, M. M., Jiménez-Amilburu, V., Günther, S., Maischein, H.-M. & Stainier, D. Y. R. (submitted). Multiple roles for the Hippo pathway effector Wwtr1 in cardiac wall maturation in zebrafish. *Development.*

Astone, M., **Lai, J. K. H.**, Dupont, S., Stainier, D. Y. R., Argenton, F. & Vettori, A. (resubmission in preparation). Hippo pathway transducers Yap1/Wwtr1 control secondary sprouting during vascular development. *Development.*

SKILLS

Bioinformatics/Computing – R and Python. **Zebrafish** – Generating mutants and transgenic lines; transplantation; *in situ* and immuno staining; live confocal imaging; microdissection. **Cell culture** – General eukaryotic, bacterial and viral culture techniques. **Molecular biology** – PCR, cloning, qPCR, Western blot. **NGS** – Raw data processing and analysis. Operate MinION device by Oxford Nanopore Technologies.

Languages – English, Malay, Mandarin and German (A2).

AWARDS AND FELLOWSHIPS

Poster Award, Weinstein Cardiovascular Meeting, Columbus, OH, USA, 2017.

International Max Planck Research School Travel Grant, Keystone Symposia, the Hippo Pathway: Signaling, Development and Disease, Taos, NM, USA, 2015.

International Max Planck Research School, Bad Nauheim, Germany, 2014 – present.

Outstanding Undergraduate Researcher Prize (OURP), Certificate of Merit and Book Prize, Singapore, 2012.

PRESENTATIONS
ORAL PRESENTATIONS

Lai, J. K. H., & Stainier D. Y. R. (2016). The Hippo Signaling Effector Wwtr1 (Taz) Interacts with Notch Signaling To Organize Cardiomyocytes into Trabeculae. *International Max Planck Research School (MPI-BN) retreat, Hohenroda, Germany.*

Lai, J. K. H., & Stainier D. Y. R. (2015). Hippo Signaling Pathway in Heart Development. *International Max Planck Research School (MPI-BN) retreat, Schloss Ringberg, Germany.*
POSTER PRESENTATIONS

Lai, J. K. H., Maischein, H.-M., Guenther, S. & Stainier, D. Y. R. (2017). Taz (Wwtr1) Links the Mechanical Processes and Signaling Networks of Cardiomyocytes to Modulate Trabeculation. *Weinstein Cardiovascular Meeting, Columbus, OH, USA.*

Astone, M., **Lai, J. K. H.,** Dupont, S., Stainier, D. Y. R., Argenton, F. & Vettori, A. (2017). Hippo Signaling Pathway Transducers Yap1/Wwtr1 are Required for Secondary Sprouting During Vascular Development. *SFB/Transregio 23 – Vascular Differentiation and Remodeling, Heidelberg, Germany.*

Lai, J. K. H. & Stainier, D. Y. R. (2016). Taz (Wwtr1), a Downstream Effector of the Hippo Signaling Pathway, is Required for Cardiac Trabeculation. *Excellence Cluster Cardio-Pulmonary System meeting, Bad Nauheim, Germany.*

Lai, J. K. H. & Stainier, D. Y. R. (2015). Hippo Signaling Pathway in Embryonic Heart Development. *Keystone Symposia – The Hippo Pathway: Signaling, Development and Disease, Taos, NM, USA.*

Lai, J, Reischauer, S. & Stainier, D.Y.R. (2014). Determining the Role of Genes Involved in Heart Chamber Specification and Development. *International Max Planck Research School (MPI-BN) retreat, Burg Guttenberg, Germany.*

Lai J & Chu JH. Identification of Putative Receptor-Binding Domain(s) on CHIKV E2 Protein. *National UROPS Congress, Singapore.*

SCIENTIFIC PROCEEDINGS

Weinstein Cardiovascular Meeting, Columbus, OH, USA, 2017.

SFB/Transregio 23 – Vascular Differentiation and Remodeling, Heidelberg, Germany, 2017.

Keystone Symposia - The Hippo Pathway: Signaling, Development and Disease, Taos, NM, USA, 2015.

Excellence Cluster Cardio-Pulmonary System – annual meeting, Bad Nauheim, Germany, 2014 – 2017.

International Max Planck Research School, MPI-HLR - annual retreat, Germany, 2014 – 2017.

SUPERVISED STUDENTS

Kristina Gagalova, Master's Thesis, Vrije University, Amsterdam, Netherlands. Jan – July 2015.

Project Title: Understanding the Biology of Morpholino in Zebrafish through Integrated Gene Expression Analysis.

Joseph Hamley, Max Planck Junior Scholars Program, Frankfurt International School, Frankfurt, Germany. July 2015.